A High-Flux Solar Concentrating System

by

Michael Mouzouris

Submitted in fulfillment of the academic requirements for the degree of

Master of Science in Mechanical Engineering

Supervisor:

Mr. Michael J. Brooks

Co-supervisor:

Prof. Lance W. Roberts

July 2011

DECLARATION

I hereby declare that this dissertation presents my own unaided work except where due acknowledgement has been given to others. This dissertation is being submitted to the University of KwaZulu-Natal for the Degree of Master of Science in Mechanical Engineering, and has not been submitted previously for any other degree or examination.

Signed:_____

As the candidate's supervisor I have approved this dissertation for submission.

Signed:_____
Name: Mr. Michael J. Brooks
Date: July 2011

As the candidate's co-supervisor I have approved this dissertation for submission.

Signed:_____
Name: Prof. Lance W. Roberts
Date: July 2011

ACKNOWLEDGEMENTS

Firstly I would like to thank my supervisor, Mr. Michael J. Brooks for always pointing me in the right direction and guiding me towards my academic development. He has provided me with an invaluable source of knowledge and constantly drove me to perform better.

Many thanks are extended to Prof. Lance W. Roberts, my co-supervisor, for his time spent discussing, both related and unrelated topics to my research. I thank him for his guidance and support.

In addition I would like to extend my thanks for the guidance of Prof. J. Bindon, Prof. W.H. Moolman, Clinton Bemont, Khulisile Kunene and Michael Constantino.

OPTIS, CeramOptec, Durban University of Technology and the University of Stellenbosch's Centre for Renewable and Sustainable energy studies (CRSES) are thanked for their support and assistance.

This research was supported by the National Research Foundation of South Africa and Eskom TESP.

Finally, I would like to thank my family for their constant support and inspiration needed to complete my studies.

ABSTRACT

This research investigates the collection of concentrating solar energy and its transmission through optical fibres for use in high temperature applications such as lunar in-situ resource utilisation (ISRU) programmes, solar power generation and solar surgery. A prototype collector, known as the Fibre Optic Concentrating Utilisation System (FOCUS), has been developed and is capable of delivering high energy fluxes to a remote target. Salient performance results include flux concentrations approaching 1000 suns with an overall optical efficiency of 13%, measured from the inlet of the collector to the fibre outlet.

The system comprises a novel solar concentrator designed to inject solar energy into a four metre long fibre optic cable for the transmission of light to the target. A nonimaging reflective lens in the form of a 600 mm diameter ring array concentrator was chosen for the collection of solar energy. Advantageous characteristics over the more common parabolic dish are its rearward focusing capacity and single stage reflection. The ring array comprises a nested set of paraboloidal elements constructed using composite material techniques to demonstrate a low-cost, effective fabrication process. At concentrator focus, a fibre optic cable of numerical aperture 0.37 is positioned to transport the highly concentrated energy away from the collector. The cable is treated to withstand UV exposure and high solar energy flux, and allows flexibility for target positioning.

A computational analysis of the optical system was performed using ray tracing software, from which a predictive model of concentrator performance was developed to compare with experimental results. Performance testing of FOCUS was conducted using energy balance principles in conjunction with a flat plate calorimeter. Temperatures approaching 1500°C and flux levels in the region of 1800 suns were achieved before injection to the cable, demonstrating the optical system's suitability for use in high flux applications. During testing, peak temperatures exceeding 900°C were achieved at the remote target with a measured flux of 104 W/cm^2 at the cable outlet. The predicted optical efficiency was 22%, indicating that further refinements to the ray trace model are necessary, specifically with regard to losses at the inlet to the cable. FOCUS was able to demonstrate its usefulness as a test bed for lunar in-situ resource utilisation technologies by successfully melting a lunar soil simulant. The system permits further terrestrial-based ISRU research, such as oxygen production from regolith and the fabrication of structural elements from lunar soil.

Στους γονείς μου, με αγάπη!

TABLE OF CONTENTS

DECLARATION ii

ACKNOWLEDGEMENTS iii

ABSTRACT iv

LIST OF TABLES ix

LIST OF FIGURES xii

LIST OF SYMBOLS xxi

CHAPTER 1: INTRODUCTION 1

1.1 Research question 1

1.2 Aims 2

1.3 Methodology 2

1.4 Publications 2

CHAPTER 2: LITERATURE REVIEW 4

2.1 Introduction 4

2.2 Solar collector technology 5

2.2.1 Solar power generation 6

2.2.2 Solar surgery 7

2.2.3 Lunar in-situ resource utilisation 8

2.2.4 HCPV module using ring array technology 10

CHAPTER 3: DESCRIPTION OF SOLAR THERMAL SYSTEM 12

3.1 Introduction 12

3.2 Ring array concentrator 13

3.3 Fibre optic cable 14

3.4 Tracking system 14

3.5 Radiometric instrumentation for DNI measurements 15

CHAPTER 4: DESIGN METHODOLOGY 16

4.1 Introduction 16

4.2 Optical system design 16

4.3 Design tools 21

4.4 Design selection 24

CHAPTER 5: CONSTRUCTION PROCESS 26

5.1 Introduction 26

5.2 Construction of reflective elements 27

CHAPTER 6: ERROR ANALYSIS 32

6.1 Introduction 32

6.2 Optical error analysis 33

6.2.1 Slope error 33

6.2.2 Surface topography measurements 33

6.2.3 Statistical analysis 34

6.3 Pointing error analysis 37

6.3.1 Misalignment error 37

6.3.2 Ray tracing model 39

6.3.3 Ray tracing results 40

6.4 Summary 44

CHAPTER 7: NUMERICAL RESULTS 45

7.1 Introduction 45

7.2 Ray tracing model 46

7.3 Ray tracing results 47

7.4 Optical efficiency 51

CHAPTER 8: ENERGY BALANCE VALIDATION METHOD 54

7.1 Introduction 54

7.2 Calorimeter construction 55

7.3 Energy balance 56

CHAPTER 9: EXPERIMENTAL RESULTS 59

9.1 Introduction 59

9.2 Experimental setup 59

9.3 Experimental procedure 60

9.4 FOCUS performance results 61

9.4.1 Concentrator focus 61

9.4.2 Optical waveguide exit 65

9.4.3 Optical efficiency 67

9.4.4 Regolith melting capabilities 68

CHAPTER 10: CONCLUSION 72

REFERENCES 75

APPENDICIES 81

A MATLAB SOFTWARE: OPTICAL SYSTEM DESIGN 81

B STATISTICAL ANALYSIS 92

C MATLAB SOFTWARE: CALORIMETRIC ENERGY BALANCE 98

D EXPERIMENTAL RESULTS 100

LIST OF TABLES

CHAPTER 2: LITERATURE REVIEW 4

Table 2.1 High temperature processes for lunar in-situ resource utilisation (Nakamura and Senior, 2004) 9

CHAPTER 3: DESCRIPTION OF SOLAR THERMAL SYSTEM 12

Table 3.1 Physical and geometric properties of FOCUS 13

CHAPTER 4: DESIGN METHODOLOGY 16

Table 4.1 Design parameters for proposed ring array concentrator and fibre optic transmission system. The primary design variable is chosen to have seven reflective elements 24

Table 4.2 Critical dimensions for a proposed array with constant ring number of seven and varying radius 25

CHAPTER 5: CONSTRUCTION PROCESS 26

Table 5.1 Physical, mechanical and heat resistance properties of low shrinking LR20/SLC60 laminating epoxy resin system 30

Table 5.2 Area of laminate and mass of resin used for hand impregnating the fibre profiles. Total mass of the completed concentrator is 5.1kg 30

CHAPTER 6: ERROR ANALYSIS 32

Table 6.1 ANOVA test results conducted at the 1% level of significance for the seven reflective elements. An $F_{critical}$ value of 3.832 is greater than the seven $F_{statistic}$ values for the elements, suggesting no statistical significant profile differences 35

Table 6.2 Slope error results for optically characterising the seven reflective elements. Results for each element include a sample of 392 observations. Calculations were conducted excluding outliers (E/O) to provide improved slope error trends between elements. Results show smaller ring elements have improved surface geometry than larger elements 36

Table 6.3 Average power values at optical waveguide inlet, P_{OWin} for the range of misalignment errors obtained by ray tracing methods for two ring array concentrator systems. 44

CHAPTER 7: NUMERICAL ANALYSIS 45

Table 7.1 Ray tracing input parameters. Eight numerical simulations of FOCUS were conducted incorporating ideal and realistic parameters for comparison 46

Table 7.2 Predicted component efficiencies and performance results for characterising the ring array concentrator with a 60 mm diameter receiver using ray tracing methods. Simulations were conducted at a typical irradiance of 850 W/m^2. 52

Table 7.3 Predicted component efficiencies and average performance results for FOCUS using ray tracing methods. Simulations were conducted at a typical irradiance of 850 W/m^2. 53

CHAPTER 9: EXPERIMENTAL RESULTS 59

Table 9.1 Performance results at concentrator focus using the ten stages. Power and flux distribution results are normalised to 850 W/m^2 and represent an average of five experimental tests conducted for each reflective shield. Theoretical results represent ray tracing simulations at an irradiance of 850 W/m^2 with Case 8 scenario parameters modelled 63

Table 9.2 Performance results of FOCUS. Experimental results were normalised to an irradiance value of 850 W/m^2 and represent an average of five tests conducted 68

Table 9.3 Lunar regolith simulant peak melt temperature and cable exit flux concentration results. 70

APPENDIX B 92

Table B.1 Slope error values after processing CMM results in a 3D modeling package. The four profile scans (+X, -X, +Y, -Y) comprise 98 points each. Data results are in milliradians 93

Table B.2 ANOVA results for element #7. The test was conducted at the 1% level of significance. 95

APPENDIX D 100

Table D.1 Five experimental measurements and results for the 6 mm diameter reflective shield, s_7 using HTAC software 102

LIST OF FIGURES

CHAPTER 2: LITERATURE REVIEW 4

Figure 2.1 Typical paraboloidal elements of a ring array concentrator with plane A illustrating the cross-sectional profile of three elements and single stage reflection to a common focal point 5

Figure 2.2 Aerial view of the Solucar Platform in Seville, Spain, showing the Solnova solar power plant using parabolic trough technology and the two central receiver plants, PS10 and PS20 for electricity generation (Abengoa solar website). 6

Figure 2.3 Maricopa solar thermal plant in Arizona, USA. The CSP plant houses sixty SunCatcher™ dishes, each with a power rating of 25 kW (Power technology website) 7

Figure 2.4 (left) Prototype of the solar fibre-optic mini dish concentrator for solar surgery. (right) Fibre optic cable delivering concentrated sunlight on to a chicken breast for experimental testing (New scientist website). 8

Figure 2.5 (left) Single concentrator array comprising seven parabolic dishes for oxygen production. (right) Seven optical bundles assembled together and integrated with a single quartz rod to inject concentrated energy into the oxygen reactor (Nakamura and Smith, 2011) 10

Figure 2.6 Prototype of the HCPV module using six ring array concentrators cut into square apertures to provide uniform flux concentrations to high performance PV receivers (Vasylyev et al., 2010).. 11

Figure 2.7 (left) Ray tracing environment illustrating the ability of light concentration with a single RAC-PV unit. (right) Ray tracing results for a single unit with a reflective improver homogenising flux concentrations onto a 3 mm PV cell (Vasylyev et al., 2010) 11

CHAPTER 3: DESCRIPTION OF SOLAR THERMAL SYSTEM 12

Figure 3.1 FOCUS consisting of a ring array concentrator integrated with an optical waveguide bundle to provide high-flux levels remote from the collector. 12

Figure 3.2 FOCUS in operation, concentrating incoming solar rays into a fibre optic cable..... 13

Figure 3.3 Aluminium fine-tuning mechanism to allow horizontal adjustment for each element.. 13

Figure 3.4 (left) Housing of the inlet to the fibre optic cable. The aluminium structure allows vertical adjustment of the focal point. (right) Representation of the inlet and outlet 6 mm diameter fused ends of the fibre optic waveguide.. 14

Figure 3.5 Dual-axis, altitude-azimuth solar tracker comprising of a linear actuator, an azimuth drive motor and a controller. (right) Controller consisting of four sensors; two for altitude movement and two for azimuth movement, used to perpendicularly align the collector to DNI.. 15

Figure 3.6 Radiometric ground station on the Howard College campus at UKZN. The instrument used for DNI measurements, NIP, is located nearby the experimental test site of FOCUS. 15

CHAPTER 4: DESIGN METHODOLOGY 16

Figure 4.1 Secondary design variables for a ring array concentrator integrated with an optical waveguide 16

Figure 4.2 (left) Top view of a ring array configuration illustrating the aperture area, Aa, in yellow and (right) the seven black projections of each element's thickness, At, which do not contribute to the collection of energy.. 17

Figure 4.3 The maximum half angle α solution line (left) and design angles, θ and α_{trial} for reflection of light into the optical waveguide (right). 18

Figure 4.4 Angles of incidence, β_i, and reflected, β_r, rays. From these angles the surface angle, γ, of R_1 is obtained..... 19

Figure 4.5 Support rib structure (left) and design of the remaining rings (right). 20

Figure 4.6 A two-dimensional solution space for five radii ring array configurations with constant geometric concentration ratio of 5000. The output of number rings shows construction feasibility. All related secondary variables are constant. 22

Figure 4.7 Two-dimensional solution of CODeC supplying a constant RAC aperture power of 250 W for five ring array systems. The number of elements required for each radius is shown. All related secondary variables are constant. 22

Figure 4.8 Three-dimensional solution surfaces of varying radius (r_o = 200 mm, 400 mm or 600 mm). Variables to select an optical system include numerical aperture, number of ring elements and power. All related secondary variables are constant. 23

Figure 4.9 Three-dimensional surface solutions for an optical system with varying number of rings (k = 5, 7 or 9). Selection variables include numerical aperture, RAC outer radius and geometric concentration ratio. All related secondary variables are constant. 23

Figure 4.10 Solution space for the proposed optical system of seven reflective rings concentrating sunlight into an optical waveguide of numerical aperture 0.37. 25

CHAPTER 5: CONSTRUCTION PROCESS 26

Figure 5.1 (left) Tooling board mould constructed to machine paraboloidal profiles for the reflective elements and (right) machined geometry for element #1 (largest element) with conic aluminium profiles 28

Figure 5.2 (left) Developed conic profiles of Miro 4 polished aluminium for the elements. (right) Profile for element #7 strapped to the tooling board mould before first lay-up. A vacuum is applied during bonding of the aluminium over the mould to enforce the paraboloidal shape. 28

Figure 5.3 (left) Aluminium profile after bonding with a bead of silicone to prevent resin offset between the metal surface and mould. Glass and carbon fibre profiles were hand impregnated with resin for the wet lay-up and second vacuum bagging process. (right) Second vacuum bag process with peel ply, perforated film and bleeder surrounding the lay-up to improve the composite finish. 29

Figure 5.4 (left) After curing vacuum is removed and the element is demoulded using tabs. (right) The completed seven FRP elements #1 to #7, anticlockwise from back right 29

Figure 5.5 A completed reflective element focusing incident rays to a point. 29

Figure 5.6 Machined aluminium framework to house reflective elements and fibre optic cable (left). Fibre reinforced plastic reflective elements nested in support framework (right). 31

CHAPTER 6: ERROR ANALYSIS 32

Figure 6.1 Cross-sectional view of the reflection of direct normal irradiation from a paraboloidal element of a ring array concentrator 32

Figure 6.2 (left) Schematic of ideal angles of incidence (α_i) and reflected rays (α_r). (right) Angles of incidence (β_i) and reflected rays (β_r) arising from the inaccuracies in the construction process yielding a slope error (φ). 33

Figure 6.3 Four profile scans (+X, -X, +Y, -Y) using a contact profilometer were measured and compared to the ideal CAD model to optically characterise each paraboloidal surface. Each scan measured 98 points on the reflective surface. 34

Figure 6.4 Comparative box-and-whisker plots for the seven reflective elements. Each plot represents the distribution of the observations showing outlier positions. The middle 50% of the observations represented by the blue box shows element #7 having the least distributed data indicating an improved construction process 36

Figure 6.5 Ray tracing environment in OptisWorks Studio. A simulation of FOCUS includes modelling the concentrator, framework and creating a sun source to generate rays. The sun source is modelled as a blackbody at a temperature of 5800 K to approximate the spectral irradiance of solar radiation 38

Figure 6.6 Two point focus concentrator systems used to compare misalignment sensitivity. Each concentrator consists of a nested set of reflective rings of 600 mm (left) and 1000 mm (right) diameter. There are seven reflective rings in both cases, but focal length differs. 39

Figure 6.7 Exaggerated misalignment angles (ε) of 0.05°, 0.10° and 0.15° at the sun source for the ring array concentrator configuration. Pointing error in an optical system is defined as the angular difference between the aperture center and the flux distribution center. 40

Figure 6.8 Ideal three-dimensional flux maps showing the irradiance levels and positioning of the reflected parallel rays of light at the inlet to the optical waveguide. Average power values are given beneath respective flux maps. The 0.6 m and 1.0 m

diameter optical systems with corresponding misalignment angles are on the left and right respectively. 42

Figure 6.9 Three-dimensional irradiance maps showing a realistic simulation of rays striking the 6 mm diameter optical waveguide inlet. Average power values are given beneath respective flux maps. The 0.6 m and 1.0 m diameter optical systems with corresponding misalignment angles are on the left and right respectively. 43

Figure 6.10 Ideal and realistic power plots at optical waveguide inlet showing misalignment sensitivity for the two systems (0.6 m and 1 m diameter systems). 44

CHAPTER 7: NUMERICAL ANALYSIS 45

Figure 7.1 Predicted optical efficiency stages for FOCUS. The four efficiency stages include the concentrator, focusing process, injection into the optical waveguide and the transmission of the concentrated sunlight to the target 45

Figure 7.2 Three-dimensional flux maps illustrating power density levels striking the 60 mm diameter copper plate for simulation cases 1 – 8. Flux levels decrease progressively due to realistic parameters implemented for each ray tracing simulation. 48

Figure 7.3 Three-dimensional flux maps representing power density levels at waveguide inlet for simulation Cases 1 – 8. Average power levels at waveguide inlet, P_{OWin} decrease progressively due to realistic parameters implemented for each case simulation. 49

Figure 7.4 Two-dimensional flux maps showing representative cross-sectional profiles of the 60 mm diameter receiver for Cases 2 - 8. Progressive losses in performance occur due to realistic ray trace modelling 50

Figure 7.5 Two-dimensional flux maps showing magnified cross-sectional flux profiles of the 6 mm diameter optical waveguide inlet for Cases 2 - 8. Progressive losses in performance occur due to realistic ray trace modelling. 50

Figure 7.6 Representative cross-sectional flux maps showing the worst case ray trace scenario of Case 8 for the 60 mm diameter copper receiver (left) and the fibre optic cable inlet (right). The two theoretical ray trace profiles will be compared to the experimental results. 51

Figure 7.7 Photomicrographs of the optical waveguide fused inlet end (left) and a 100 times magnified view showing the hexagonal geometry of the silica fibres (right). 52

CHAPTER 8: ENERGY BALANCE VALIDATION METHOD 54

Figure 8.1 Exploded view of the flat plate calorimeter constructed for performance measurements of FOCUS. The device consists of a cylindrical stainless steel outer casing that houses a nylon insulator, a radial flow distributor and the copper receiving plate (left). Pre-assembly of the flat plate calorimeter is shown on the right 55

Figure 8.2 (left) Calorimeter cross-section illustrating the conservation of energy for a steady-flow, open system. (right) Top view of the six thermocouple positions inside the copper plate, starting with T_0 at r = 0 mm, increasing anti-clockwise in increments of 5 mm, ending with T_{25} at r = 25 mm. 57

Figure 8.3 (left) Calorimeter side view showing water inlet and outlet passages. (right) Top view of the six thermocouple positions inside the painted copper plate to estimate convective and radiative heat losses 58

CHAPTER 9: EXPERIMENTAL RESULTS 59

Figure 9.1 Experimental layout for the second test phase to characterise the flux at fibre optic cable exit. Fundamental components include FOCUS, the flat plate calorimeter, water pumping system and thermocouples 59

Figure 9.2 (left) Calorimeter positioned at concentrator focal point to characterise the performance of the composite material RAC and (right) fibre optic cable directed onto the calorimeter to determine exit flux concentration. 60

Figure 9.3 Water circulation system showing throttle valve to achieve the desired mass flow rate. 61

Figure 9.4 (left) The nine reflective shields with nylon backing used to characterise the average power striking the exposed copper surface. From the top right in an anti-clockwise direction, the shields (s_2-s_{10}) allow copper exposure of diameter 3 mm, 4 mm,5 mm, 6mm, 8 mm, 10 mm, 20 mm, 30 mm and 40 mm. (right) The 6 mm diameter reflective shield positioned at concentrator focus with a nylon backing to minimise conduction between the shield and copper surface 62

Figure 9.5 Two reflective shields illustrating the methodology used to obtain a band flux, $F_{band,s_q-s_{q+1}}$ on the copper surface. Shields on the left and right represent smaller, s_{q+1} and larger, s_q exposed surfaces respectively. Average powers striking the

exposed surface are illustrated with $P_{s_{q+1}}$ and P_{s_q} on the areas $A_{s_{q+1}}$ and A_{s_q} respectively. 63

Figure 9.6 Experimental results showing the flux distribution at concentrator focus at a typical irradiance level of 850 W/m^2. Peak flux levels recorded are illustrated with the 3 mm diameter reflective shield. 64

Figure 9.7 Performance results at concentrator focus showing flux levels striking the 60 mm diameter copper plate (left) and a magnified view of the 6 mm diameter inlet to the optical waveguide (right). Theoretical and experimental results illustrate performance levels at 850 W/m^2 64

Figure 9.8 Average power striking receiver as a function of exposed copper surface diameter. Theoretical and experimental results illustrate performance levels at 850 W/m^2 64

Figure 9.9 (left) Reflective shield at fibre optic cable inlet allowing concentrated solar energy into the 6 mm diameter quartz glass inlet. (right) Vertical displacement of the cable outlet prevents back reflection onto the 900 fibres resulting in cable damage 65

Figure 9.10 Diagram illustrating exit cable concentrations as a function of vertical displacement (*VD*) from the receiver. Numerical aperture, diameter of the exit quartz glass and distance from the receiver characterise the flux striking the target. Experiments were conducted using a 5 mm *VD* from calorimeter centre to prevent cable damage. 66

Figure 9.11 Relationship between vertical displacement of the optical waveguide to the flux concentration striking the copper surface. The trend represents an average power of 20.5 W striking the calorimeter at an irradiance of 850 W/m^2 67

Figure 9.12 Realised optical efficiency stages for FOCUS. The power values given are based on a nominal input flux of 850 W/m2 acting on an aperture of 0.192 m2. Calorimetric experiments showed representative optical waveguide inlet and outlet powers of 39.4 W and 20.5 W respectively. 68

Figure 9.13 Regolith melting experiment, including a downward facing reflective shield and a thermocouple for the central melt temperature measurement. The lunar regolith simulant, JSC-1 was placed in a ceramic dish at a 5 mm vertical displacement from the cable. 69

Figure 9.14 (left) Post experimental observations of JSC-1 in the ceramic dish showing a circular melt zone with (right) a magnified view of the vitrified melt having an estimated diameter of 6 mm and depth 2.5 mm. 70

Figure 9.15 (left) Time evolution of the melt temperature for each of the five experiments. Temperature stabilisation in the melt zone is evident over the six minute test period. (right) Peak melt temperatures vs. flux levels at cable exit. Flux results represent a maximum value exiting the 900 silica fibres at varied irradiance levels.. 70

Figure 9.16 A vitrified sample of JSC-1 illustrating an 'S' shaped geometry obtained by shifting the regolith beneath the cable in intervals of 60 seconds. The sample approximates a square geometry with 12 mm sides and shows the ability of lunar surface stabilisation using concentrated solar energy.. 71

APPENDIX B 92

Figure B.1 Histogram plot for the 392 slope error observations for element #7. The highest frequency occurs near the ideal 0 mrad slope error with frequencies on either side decreasing. The histogram approximates a normally distributed curve with its symmetric bell-shaped appearance 96

Figure B.2 Box-and-whisker plot for element #7 showing the statistical spread in the data. The blue box indicates the middle 50% of the 392 observations and is calculated from Q1, Q2 and Q3. Outliers are evident outside the upper and lower inner fence boundaries. 97

APPENDIX D 100

Figure D.1 LabVIEW block diagram illustrating the methodology for obtaining temperature measurements from the eight thermocouples in the calorimeter 101

Figure D.2 LabVIEW environment showing the time evolution of temperature for all thermocouples. 102

Figure D.3 Results from experiment #3, showing a water temperature difference of 6.4°C (left) and temperature measurements midway in the copper plate (right). The experimental procedure was conducted for three minutes allowing the temperatures to reach steady state conditions 103

Figure D.4 Temperature distribution midway in copper plate (z = 3 mm) after three minutes of testing. Assuming a concentric focal spot on the calorimeter surface allows obtaining a mirrored representation of temperatures on the full diameter copper plate. 104

LIST OF SYMBOLS

Nomenclature

A	Area	[mm^2]
AA	Active area	[mm^2]
C	Geometric concentration ratio	
C_{flux}	Flux concentration ratio	
C_{max}	Theoretical maximum geometric concentration ratio	
$C_{p,w}$	Specific heat of water	[J/kg.K]
$\dot{E}$	Energy rate	[J]
f	Focal point	[mm]
F	Average flux	[W/m^2]
$F_{critical}$	Calculated statistic value	
$F_{statistic}$	Standard statistic value	
GF	Gradient factor	
G_{sc}	Solar constant	[W/m^2]
h	Convective heat transfer co-efficient	[$W/K.m^2$]
h_r	Height of ring 1	[mm]
H_o	Null hypothesis	
H_1	Alternative hypothesis	
k	Number of ring elements	
k_t	Thermal conductivity	[W/m.K]
$\dot{m}$	Mass flow rate	[kg/s]
m_B	Gradient at point B	
MS_B	Mean squares between samples	
MS_W	Mean squares within samples	
n	Refractive index	
N	Number of observations	
NA	Numerical aperture	
N_f	Number of fibres	
P	Power	[W]
q	Solar power	[W]

$\dot{q}''$	Heat flux	[W/m^2]
r	Radius	[mm]
r_{OWout}	Optical waveguide outlet radius	[mm]
R	Ring element	
t	Thickness of ring 1	[mm]
T	Temperature	[K]
TA	Total area	[mm^2]

Greek symbols

α	Maximum entrance half-angle of the optical waveguide	[deg]
α_s	Surface absorptivity	
$\alpha_{l.o.s}$	Level of significance	
α_{trial}	Design half-angle of ring 1	[deg]
β_i	Angle of incidence	[deg]
β_r	Angle of reflection	[deg]
γ	Surface angle	[deg]
ε	Misalignment angle	[deg]
ε_s	Surface emissivity	
η	Efficiency	
θ_s	Solar half-angle	[deg]
θ	Design half-angle of ring k	[deg]
σ	Stefan-Boltzmann constant	[W/m^2.K^4]
μ	Profile mean	
φ	Slope error angle	[deg]

Subscripts

1	First element
2	Second element
a	Aperture
abs	Absorbed
act	Actual

amb	Ambient
band, s_q -s_{q+1}	Band
conv	Convection
Cu	Copper plate
foc	Focussing process
g	Generated
ik	Inner k^{th} element
in	Inlet
inj	Injection into optical waveguide
k	k^{th} element
l,out	Outlet losses
o	Outer element
ow	Optical waveguide
OW_{in}	Optical waveguide inlet
OW_{out}	Optical waveguide outlet
out	Outlet
r	Receiver
rad	Radiation
RMS	Root mean square
RAC	Ring array concentrator
s	Surface
s_q	Reflective shield q
s_{q+1}	Reflective shield q+1
st	Stored
t	Transmission through optical waveguide
theo,in	Theoretical value at inlet

Abbreviations

ANOVA	Analysis of variance test
CAD	Computer aided drawing
CMM	Co-ordinate measuring machine
CNC	Computer numerical control
CODeC	Concentrating optics design code

CPV	Concentrating photovoltaic
CSP	Concentrating solar power
DCC	Direct computer control
FOCUS	Fibre optic concentrating utilisation system
FRP	Fibre reinforced plastic
HCPV	High-concentrating photovoltaic
ISRU	In-situ resource utilisation
OW	Optical waveguide
RAC	Ring array concentrator
SHOT	Scanning Hartman optical test

1. INTRODUCTION

Renewable energy can potentially play a vital role for global sustainable development and diversifying energy supply. Fossil fuels and nuclear power have dominated power generation, with outcomes that threaten the health of the population and lead to environmental degradation. Mainstream renewable energy technologies such as, solar energy, wind turbines, geothermal, biomass and hydro-power have the potential to replace and prolong conventional power plants while alleviating their negative effects.

The Sustainable Energy Research Group (SERG) was established at the University of KwaZulu-Natal (UKZN) to focus on such technologies. SERG was formed within the School of Mechanical Engineering, at the Howard College Campus with an aim to meet the challenge of a safe, sustainable energy supply. Current research areas include solar energy and wind power. A broad-ranging interest exists within the solar energy field, including research in concentrator design, resource assessment, heating and cooling. Wind energy research areas include resource assessment, wind turbine blade design and low wind speed performance optimisation. Future prospects within SERG include the design and optimisation of a small-scale solar thermal power plant, ocean current energy generation, energy storage systems and sustainable transport systems. Existing facilities at the Howard College campus include a radiometric ground station, a parabolic trough solar thermal collector and a 2 kW wind turbine. Further solar collector design and construction involves a novel type solar concentrator that is the topic of this research.

1.1 Research question

This study contributes to the development of renewable energy systems, specifically solar thermal collectors which provide concentrated thermal energy for high temperature applications. Whereas parabolic dish collectors are normally used for concentrating solar energy, this research addresses the use of a novel, nonimaging reflective lens in the form of a ring array concentrator. The lens produces a hot spot of concentrated solar energy to the rear of the structure where energy is injected into optical fibres for transmission of the high heat-flux to a remote target. Design and construction of the prototype will contribute to the development of sustainable energy technologies with salient performance metrics determined through laboratory testing.

1.2 Aims

The research aim is to design, construct and test a point-focus solar concentrator for high-flux applications. A prototype solar thermal optical system is proposed for design and construction with the following research objectives:

1. Describe the design of a collector integrated with a fibre optic cable to concentrate direct normal solar irradiance.
2. Describe a low-cost, construction method for the collector.
3. Characterise the construction process using an optical and pointing error analysis.
4. Obtain a theoretical performance model of the system using ray tracing software.
5. Validate theoretical results using a measurement device for high-flux solar concentrations.
6. Assess the optical efficiency and thermal performance of the individual components as well as the overall optical efficiency of the solar thermal system.

1.3 Methodology

The research methodology comprises of four phases, including:

1. Review of the relevant literature for optical systems.
2. Design and construction of a prototype optical system.
3. Development of a theoretical model to predict system performance.
4. Validation of the theory with experimental laboratory testing.

1.4 Publications

In the course of performing this research the following publications have been documented:

1. Mouzouris, M. and Brooks M.J. "Nonimaging solar thermal collector for high temperature terrestrial and space applications" Proceedings of SPIE Optics and Photonics Vol. 7423, San Diego, CA, August 1-6, 2009.
2. Mouzouris, M. and Brooks M.J. "Misalignment effects in a point focus solar concentrator" Proceedings of ISES Solar World Congress, Johannesburg, RSA, October 11-14, 2009.

3. Mouzouris, M. and Brooks M.J. “Construction of a composite material solar concentrator for high heat flux applications” Proceedings of 8th Annual International Energy Conversion Engineering Conference Vol. 7097, Nashville, TN, July 25-28, 2010.
4. Mouzouris, M., Roberts, L.W. and Brooks M.J. “Heat transfer analysis for high-flux solar measurements using a flat plate calorimeter” Proceedings of First Postgraduate Renewable Energy Symposium, CRSES, Stellenbosch, RSA, November 11-12, 2010.
5. Mouzouris, M., Roberts, L.W. and Brooks M.J. “Thermal performance of a high-flux solar concentrating system” In preparation for R&D Journal, 2011.

2. LITERATURE REVIEW

2.1 Introduction

With a global move towards responsible energy use and reduction in fossil fuel dependence, there is a need for technologies that can supply heat without consuming electricity. This can be achieved by using solar energy as a fuel coupled with a form of solar collector to transform the energy into heat. The heat is then transferred to a fluid, which acts as the driving force for the required application.

Transforming radiation into heat is a function of the amount of energy the Earth intercepts from the Sun. The Sun emits energy in the form of electromagnetic radiation with a spectral distribution between the wavelengths 250 nm - 3000 nm (Duffie and Beckman, 2006). It has an effective blackbody temperature in the region of 5800 K and subtends a half-angle, θ_s, of 0.265° at the Earth. The radiation emitted by the Sun and its geometric positioning to the Earth govern the nearly constant extraterrestrial energy intensity. The solar constant, G_{sc} defines the flux density on a surface perpendicular to the solar rays outside the Earth's atmosphere and is generally accepted to be 1367 W/m^2. Due to atmospheric interactions typical direct normal irradiance levels between 800 W/m^2 – 1000 W/m^2 arrive at the Earth's surface under clear sky conditions. Atmospheric attenuation of solar radiation occurs due to scattering and absorption. Scattering is caused by the interaction of solar rays with air molecules, water and dust particles, while absorption occurs due to ozone, water vapour and carbon dioxide. The remaining radiation striking the Earth can be effectively concentrated using a solar collector for high heat-flux applications.

Collector performance is commonly characterised by geometric concentration ratio, *C*, defined as the collector aperture area to that of the receiver (Equation 2.1). Geometric properties of the Sun allow establishing a maximum concentration ratio for cylindrical concentrators, C_{max}, derived from the second law of thermodynamics, as described in Equation 2.2 (Welford and Winston, 1978). Using θ_s as 0.265°, the theoretical maximum flux concentration for solar concentrators in air-filled media exceeds 46 000 suns, where one sun refers to 1000 W/m^2. Several concentrating collector technologies have been developed to achieve high concentrations for the efficient transformation of sunlight into heat.

$$C = \frac{A_a}{A_r} \tag{2.1}$$

$$C_{max} = \left(\frac{A_a}{A_r}\right)_{max} = \frac{1}{\sin^2(\theta_s)} \tag{2.2}$$

2.2 Solar collector technology

The most important component of any solar thermal system is the collector. Solar collectors are used to capture solar radiation and transform it into thermal energy for applications such as electricity production and generation of hydrogen (Pregger et al., 2009). They are categorised either as non-concentrating, for example the flat plate variety used in solar water heating applications, or concentrating, such as those collectors employed for high heat-flux applications (Kalogirou, 2004). Non-concentrating type collectors are used for stationary systems and provide temperatures between 30˚C and 200˚C. Concentrating collectors are classified into line focus or point focus systems (Sen, 2004). Parabolic troughs and linear Fresnel mirrors are examples of line focus concentrators and have operating temperature ranges between 60˚C and 400˚C. Point focus technologies include parabolic dishes and central receivers that can achieve temperatures in excess of 1500°C (Kalogirou, 2004). A novel point focus collector introduced by Vasylyev and Vasylyev (2003) is the ring array concentrator (RAC), which provides high concentration with single stage reflection. Advantages over the commonly used parabolic dish include rearward focusing and the potential to outperform the dish geometry at shorter focal lengths (Vasylyev and Vasylyev, 2002). The rearward focusing characteristic eliminates the need to employ a Cassegrain-type design to achieve an upward facing receiver, which further decreases flux concentrations due to expansion of the solar image (Feuermann and Gordon, 1998). The ring array configuration is formed by a set of concentrically nested paraboloidal elements that operate similarly to a Fresnel lens to converge incident solar rays to a common point, as shown in Figure 2.1. Unlike a Fresnel lens, the sunlight is reflected, not refracted, therefore optical losses are reduced (Vasylyev and Vasylyev, 2005). The successful deployment of various solar concentrating technologies has been shown for high temperature applications, such as solar power generation, solar surgery and material sintering.

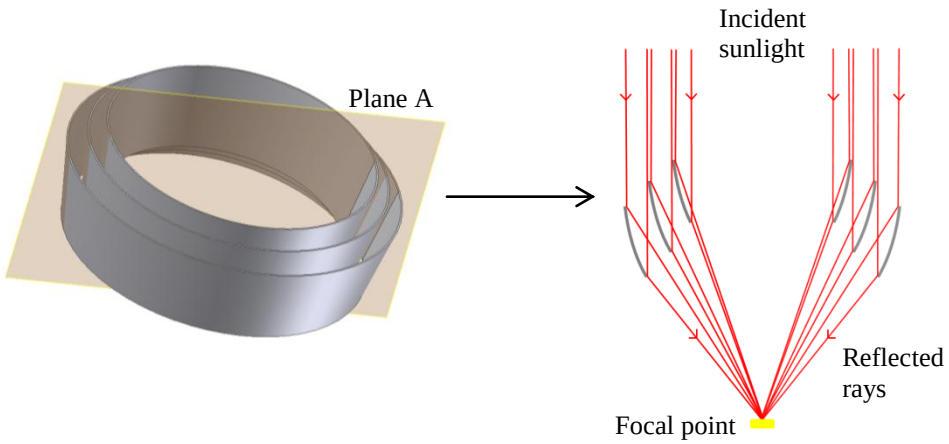

Figure 2.1 Typical paraboloidal elements of a ring array concentrator with plane A illustrating the cross-sectional profile of three elements and single stage reflection to a common focal point.

2.2.1 Solar power generation

Converting solar energy into electrical power has been one of the primary motivations for solar energy research. Direct and indirect conversion methods include using non concentrating photovoltaic cell, (PV) concentrating photovoltaic cell (CPV) or concentrating solar power (CSP) technology respectively. The development of photovoltaic cells to withstand high-flux concentrations allows for efficient power generation when coupled to a solar concentrator (Feuermann and Gordon, 2001). Proven forms of CSP technology include the use of parabolic troughs (Odeh et al., 1998), Fresnel mirrors (Mills and Morrison, 2000), central receivers and dish/Stirling engine systems. Operating principles of the four CSP technologies are fundamentally similar. Sunlight is concentrated onto a receiver to create thermal energy which in turn generates steam to drive turbines and generators, much like conventional coal-fired power plants. As an example of currently deployed CSP technologies, Abengoa Solar are in the process of erecting five parabolic trough units with a combined power capacity of 250 MW at the Solnova Solar Power Station in Spain. Of the five power stations, three have been commissioned for commercial operation during 2010, with the remaining two under development at the Solucar Platform in Seville (Figure 2.2). In addition to the parabolic trough CSP plants at the Solucar Platform, two existing central receiver plants, PS10 and PS20 provide a combined power of 31 MW.

Figure 2.2 Aerial view of the Solucar Platform in Seville, Spain, showing the Solnova solar power plant using parabolic trough technology and the two central receiver plants, PS10 and PS20 for electricity generation (Abengoa solar, 2011).

Technologies favourable for smaller power generation plants include dish/Stirling systems such as the 1.5 MW Maricopa solar plant in Arizona, USA. The CSP plant, operated by Tessera Solar, uses SunCatcher^{TM} technology developed by Stirling Energy Systems with the advantages of being standalone

and mobile units (Figure 2.3). The disadvantage of these systems is the requirement of a fixed receiver at concentrator focal point that results in robust framework designs for Stirling engines. The usefulness of a solar thermal system is enhanced if energy can be transferred to a location remote from the collector's focal point. In this regard the integration of collectors with fibre optic energy transmission has been proposed for solar power generation (Seboldt, 2004). Kribus et al. (2000) proposed a dish-fibre-engine system comprising a primary parabolic dish with secondary concentration to re-focus solar rays downward. At secondary focus concentrated rays are injected into optical fibres where transmission to the stationary engine occurs. Possible advantages of the system include reduced weight and wind loads on the concentrator, and easier access to the engine. In addition to using concentrator-fibre optic technology for CSP generation, other applications such as solar surgery and material sintering have been demonstrated using point focus technologies.

Figure 2.3 Maricopa solar thermal plant in Arizona, USA. The CSP plant houses sixty SunCatcher™ dishes, each with a power rating of 25 kW (Power technology, 2011).

2.2.2 Solar surgery

Solar surgery is the proposed use of concentrated sunlight as an inexpensive alternative to lasers for various surgical operations such as tissue transformations (Feuermann and Gordon, 1998). The primary characteristic of laser light therapy which makes it attractive for medical surgeries is its high power density from a few to tens of W/mm^2 (Gordon et al., 2003). A major surgical application using such high-flux levels is the termination of cancerous growths and tumors by highly localised thermal energy. Gordon et al. (2002) have demonstrated a prototype solar fibre-optic mini dish system, constructed using readily available components, capable of delivering the power densities required for typical laser surgery applications (Figure 2.4, left). The optical system comprises a 200 mm diameter parabolic dish coupled to an optical fibre 1 mm in diameter that achieved consistent peak power densities of 10 W/mm^2 with flux

concentrations exceeding 11 000 suns (Feuermann et al., 2002). Experimental testing involved chicken breast and liver samples as test material, (Figure 2.4, right). Concluding results of the solar surgery experiments showed test samples having the same tissue transformation properties to corresponding laser therapy procedures. In addition to being an inexpensive competitor to traditional laser therapy, a solar surgery optical system can be a mobile unit for prompt emergency surgeries in remote locations. The feasibility of using solar surgery however is limited to sun abundant areas. A space-based area of research where sunlight is plentiful is lunar in-situ resource utilisation, where optical systems are being developed for applications such as material sintering and oxygen production.

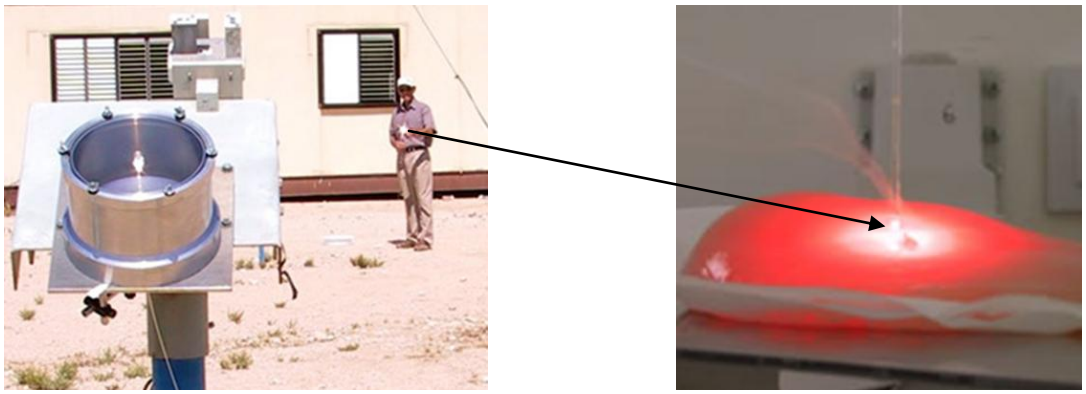

Figure 2.4 (left) Prototype of the solar fibre-optic mini dish concentrator for solar surgery. (right) Fibre optic cable delivering concentrated sunlight on to a chicken breast for experimental testing (New scientist, 2011).

2.2.3 Lunar in-situ resource utilisation (ISRU)

The use of lunar in-situ resources for producing sintered structural blocks, rocket propellant and life support materials has been proposed as a means to reduce the cost of future Moon exploration missions (Nakamura and Senior, 2008). For example NASA's ISRU program focuses on technologies required to extract oxygen, water and nitrogen needed for various life support and manufacturing processes. Solar energy is the most readily available source of energy on the Moon and can be used effectively for lunar materials processing. Nakamura and Senior (2004) classified these high temperature processes into nine categories with thermal requirements varying between 900 K and 2500 K (Table 2.1). They demonstrated the use of parabolic mirrors coupled to fibre optic cables to achieve these temperature ranges for ISRU. Their prototype solar thermal power system comprises four paraboloidal dishes of 500 mm diameter each, having secondary concentrators to boost concentrations into an optical waveguide (OW) transmission

line. Each OW was positioned into a single thermal reactor for the hydrogen reduction of lunar soil (regolith) to produce oxygen, process 2 in Table 2.1. The constituent of lunar soil that makes it attractive for oxygen production is the mineral ilmenite, $(Fe,Mg)TiO_3$ which requires the endothermic chemical reaction of Equation 2.3. For experimental testing Nakamura et al. (2008) used a lunar regolith simulant, JSC-1 which approximates lunar soil properties. They successfully demonstrated the capability of the OW solar thermal system to melt JSC-1 at a minimum flux of 85 W/cm^2 corresponding to a temperature of 1556°C. The experimental procedure to extract the oxygen includes depositing hydrogen gas into the solar heated thermal reactor at the required temperature. The heated gas diffuses through JSC-1 resulting in the thermochemical reaction, which produces water as a by-product. Water electrolysis is then performed to release the oxygen while the hydrogen is recycled back into the system for further reduction of ilmenite.

Table 2.1 High temperature processes for lunar in-situ resource utilisation (Nakamura and Senior, 2004).

Class		Description	Examples	Temperature (K)
Chemical process recovery	**1**	Pyrolysis	Oxygen production at low to medium pressure	2000-2500
	2	Gas-solid reactions	Reduction of regolith to produce oxygen	1000-1200
	3	Gas-liquid or three-phase reactions	Reduction of magma to produce oxygen, silicates	1600-1800
	4	Desorption of solids	Solar wind volatiles, drying	1000-1200
Manufacturing	**5**	Hot liquid processing	Metal/basalt casting, glass processing	1200-1800
	6	Sinter forming	Powder metallurgy, refractory sintering	900-1800
	7	Composite forming	Fibres, whiskers, flakes in matrix	900-1800
	8	Welding/Glass blowing		1600-1800
Power operations	**9**	Thermal energy storage	In fused basalt	<1400

$$FeTiO_3 + H_2 \rightarrow Fe + TiO_2 + H_2O \quad (2.3)$$

More recent research includes the development of a single concentrator array consisting of seven parabolic dishes delivering concentrated solar power to a carbothermal reactor for oxygen production (Nakamura and Smith, 2009). The optical system consists of seven paraboloidal concentrators with secondary reflectors concentrating sunlight downward into optical fibres (Figure 2.5, left). The seven cable outlets are integrated with a single quartz rod which injects the highly concentrated sunlight into the carbothermal oxygen reactor to create high temperature molten regolith (Figure 2.5, right). Experimental

testing of the concentrator array showed a measured power output of 795 W delivered to the reactor with overall system efficiency being 38% (Nakamura and Smith, 2011).

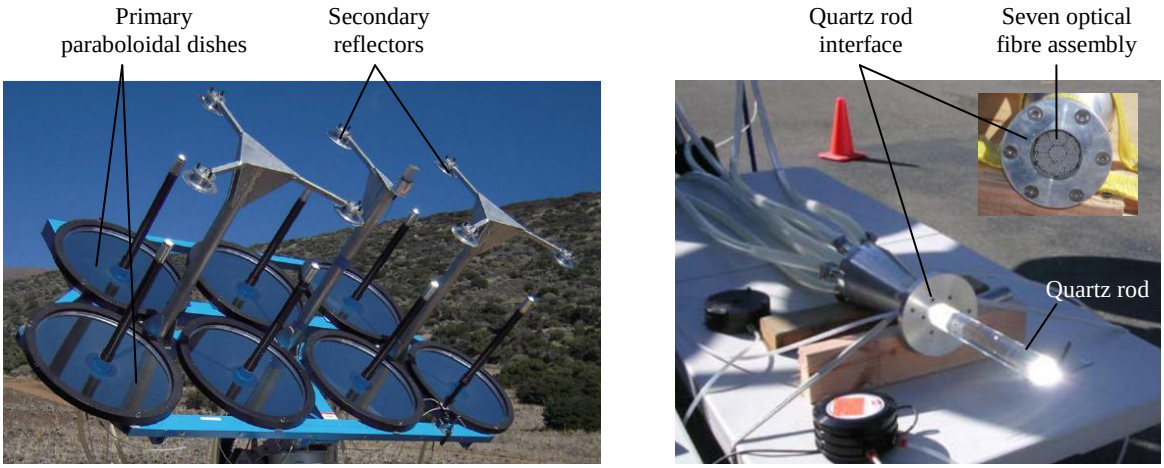

Figure 2.5 (left) Single concentrator array comprising seven parabolic dishes for oxygen production. (right) Seven optical bundles assembled together and integrated with a single quartz rod to inject concentrated energy into the oxygen reactor (Nakamura and Smith, 2011).

In addition to lunar regolith melting, the concentrator array was used to sinter a native soil in Hawaii called Tephra, for applications including surface stabilisation (Nakamura and Smith, 2011). A stable lunar surface facilitates robotic or human exploration and can be achieved by sintering regolith at lower temperatures and flux levels than required with regolith melting. Experiments resulted in the successful sintering of Tephra between temperatures of 1000°C – 1100°C, at flux levels of 70 W/cm^2. At higher temperatures and concentrations molten slag forms which is not desirable for surface stabilisation. Knowledge of the Tephra sintering experiments aids the development of solar concentrating systems for lunar regolith surface stabilisation.

2.2.4 HCPV module using ring array technology

To date, reflective parabolic dishes have largely been used for point focus applications, however non-traditional optics such as the ring array concentrator potentially has properties better suited for applications such as HCPV. Vasylyev et al. (2010) constructed a prototype optical system using six RAC configurations of 100 mm diameter each to provide uniform flux concentrations for HCPV (Figure 2.6). The concentric RAC geometry was converted into square apertures to achieve a flat-plate HCPV panel,

with a Fresnel lens filling the central cavity to boost concentration. A ray tracing analysis illustrates expected performance levels of a single RAC-PV unit approximating uniform flux distribution on to a 3 mm PV cell (Figure 2.7, left). Uniform concentration was optimised using a reflective focus improver to achieve average concentrations in the region of 1000 suns (Figure 2.7, right). Preliminary on-sun testing has produced 3 mm square focal concentrations, thereby approximating the geometric concentration ratio of 1100. Further performance characterisation of the system is in progress with future objectives including the development of a full-sized HCPV panel. Advantages of the RAC-PV optical system over existing Fresnel technology are improved concentrations and optical efficiencies, (Vasylyev, 2005) which attracts research and development using RAC configurations.

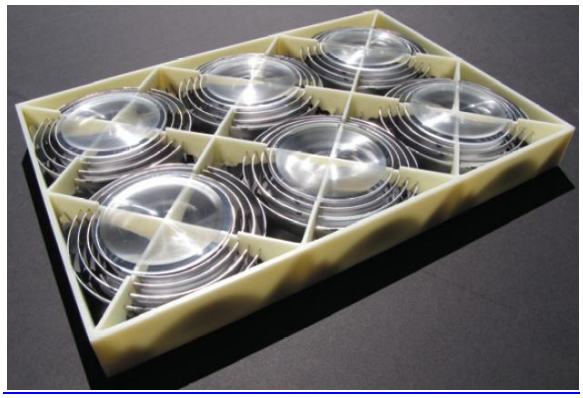

Figure 2.6 Prototype of the HCPV module using six ring array concentrators cut into square apertures to provide uniform flux concentrations to high performance PV receivers (Vasylyev et al., 2010).

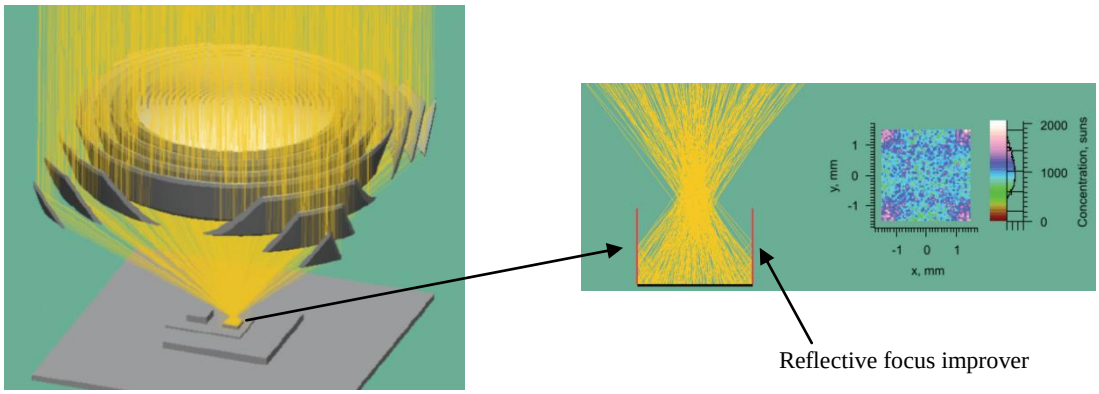

Figure 2.7 (left) Ray tracing environment illustrating the ability of light concentration with a single RAC-PV unit. (right) Ray tracing results for a single unit with a reflective improver homogenising flux concentrations onto a 3 mm PV cell (Vasylyev et al., 2010).

3. DESCRIPTION OF SOLAR THERMAL SYSTEM

3.1 Introduction

Solar concentrating technologies have been extensively reported for the efficient collection of solar radiation for high temperature processes. Previous optical systems include the development of parabolic dish collectors for applications such as CSP, solar surgery and lunar ISRU. Novel point focus systems have been demonstrated using ring array technology for HCPV applications, which can provide improved performance over existing systems.

This study aims to design and construct a concentrator to provide thermal energy for high-flux applications, using a ring array concentrator integrated with a fibre optic bundle. The solar thermal concentrating system is known as the Fibre Optic Concentrating Utilisation System, (FOCUS) and has been developed at the University of KwaZulu-Natal (UKZN) to provide thermal input to high temperature processes. The system is intended for use in a university ISRU program, primarily to demonstrate the melting of a lunar regolith simulant at 85 W/cm^2 for oxygen production. The optical system consists of three key components; the ring array concentrator, fibre optic cable and a solar tracking system (Figure 3.1). Figure 3.2 shows the system in operation with incoming direct normal irradiation being concentrated and transmitted through the fibre optic cable to a location remote from the collector. Physical and geometric properties of FOCUS are given in Table 3.1.

Figure 3.1 FOCUS consisting of a ring array concentrator integrated with an optical waveguide bundle to provide high-flux levels remote from the collector.

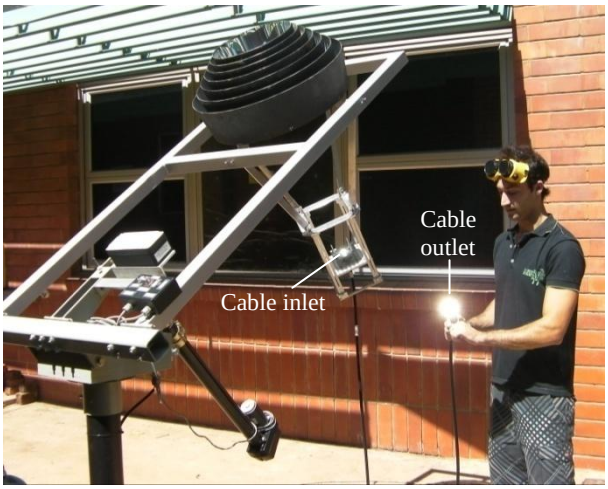

Figure 3.2 FOCUS in operation, concentrating incoming solar rays into a fibre optic cable.

Table 3.1 Physical and geometric properties of FOCUS.

Total height of concentrator (mm)	293
Reflective aperture area (mm^2)	1.92×10^5
Geometric concentration ratio at fibre optic cable outlet	6777
Concentration ratio at cable inlet (suns)	1639
Concentration ratio at cable outlet (suns)	999
Numerical aperture of fibre optic cable	0.37
Focus from outer ring (mm)	677
Thickness of each ring element (mm)	3

3.2 Ring array concentrator

The concentrator is 600 mm in diameter and consists of seven reflective elements, each having a different paraboloidal geometry to reflect incoming direct normal irradiance into a fibre optic cable. A rigid, aluminium support structure allows vertical alignment of the seven elements and ensures they act as one concentrator, reflecting incident rays to a common focus. To allow fine-tuning of the collective system, each reflective element can be adjusted horizontally in two dimensions using aluminium tabs (Figure 3.3).

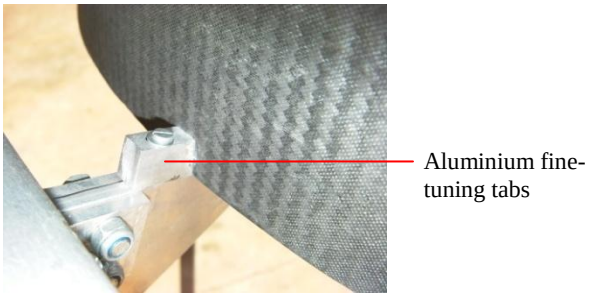

Figure 3.3 Aluminium fine-tuning mechanism to allow horizontal adjustment for each element.

3.3 Fibre optic cable

The fibre optic cable is manufactured by CeramOptec with a 0.37 numerical aperture consisting of 900 silica fibres treated to resist UV degradation. The numerical aperture represents the range of angles over which the cable can accept and emit light. The cable is housed in an aluminium framework that allows vertical displacement for focal point adjustment (Figure 3.4, left). The bundle is 4 meters in length with 95% internal transmission efficiency (CeramOptec website) and has a 6 mm diameter fused end at inlet and outlet (Figure 3.4, right). The fused inlet lowers injection losses by minimising the inter-fibre spaces.

Figure 3.4 (left) Housing of the inlet to the fibre optic cable. The aluminium structure allows vertical adjustment of the focal point. (right) Representation of the inlet and outlet 6 mm diameter fused ends of the fibre optic waveguide.

3.4 Tracking system

The concentrator array is equipped with a dual-axis, altitude-azimuth solar tracker provided by Small Power Systems (Small Power Systems, 2011). Key components include; a linear actuator for altitude movement, a drive motor for azimuth movement and a controller. The controller senses direct normal irradiation (DNI) and sends signals to the drive motors for correct sun-concentrator alignment (Figure 3.5, left). The controller or sun sensor keeps the sun in an average band of 0.05° relative to each concentrator axis to minimise the optical losses that occur when incident light deviates from the aperture normal. It has two degrees of freedom to perpendicularly align the collector to DNI and two sensors per axis to adjust the collector in the altitude and azimuth direction every 1-2 seconds in increments of 0.025° (Figure 3.5, right). One set of sensors is used for wide angle movement while the other is for precision adjustments. In addition, the controller has a daylight sensor which, after sunset, sends a signal to the drive motors to position the collector east. The tracker is built with a set of manual controls for the approximate positioning of the collector to DNI, after which autonomous control, using the sensors, can be selected.

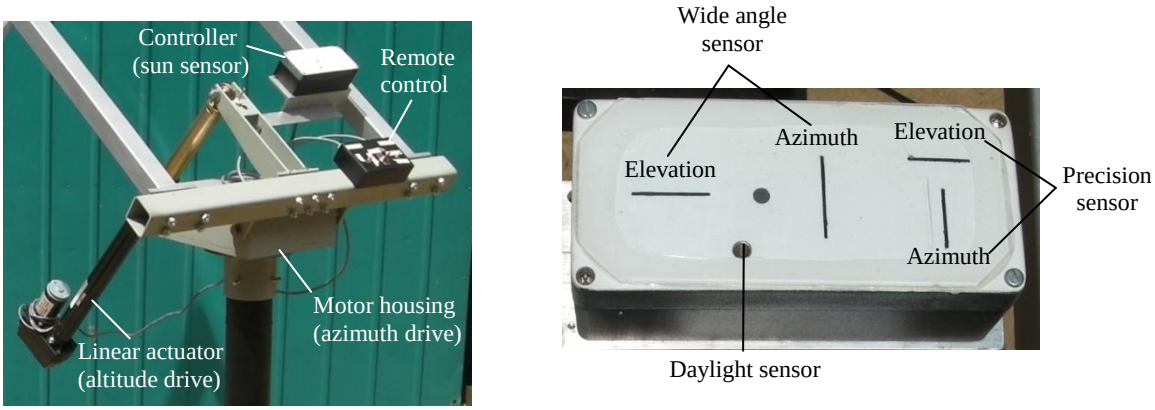

Figure 3.5 (left) Dual-axis, altitude-azimuth solar tracker comprising of a linear actuator, an azimuth drive motor and a controller. (right) Controller consisting of four sensors; two for altitude movement and two for azimuth movement, used to perpendicularly align the collector to DNI.

3.5 Radiometric instrumentation for DNI measurements

To conduct the controlled experimental procedure, accurate DNI measurements were obtained from a radiometric ground station on the Howard College campus at UKZN (Brooks and Roberts, 2009). The ground station is located at 29.9° South and 30.98° East in a nearby position to the experimental test site for FOCUS (Kunene et al., 2010). The nearby position allows the assumption of similar DNI readings at the experimental test site. The instrumentation bench is 151.1 meters above sea level and consists of four radiometers, including an Eppley normal incidence pyrheliometer (NIP) which was used to obtain average DNI levels for the experimental procedure (Figure 3.6).

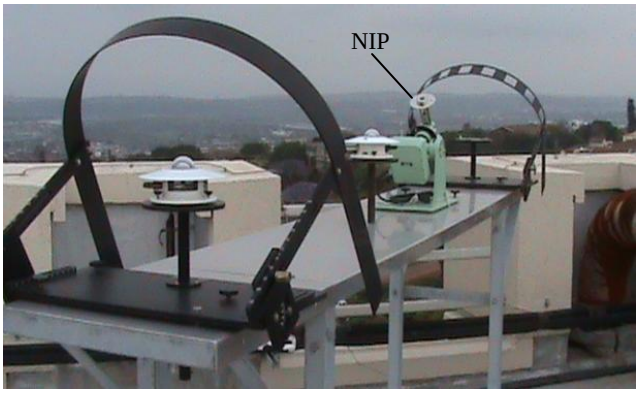

Figure 3.6 Radiometric ground station on the Howard College campus at UKZN. The instrument used for DNI measurements, NIP, is located nearby the experimental test site of FOCUS.

4. DESIGN METHODOLOGY

4.1 Introduction

The design methodology applied to the RAC is based on nonimaging optical theory and geometric principles to develop an optical system that comprises a ring array concentrator reflecting direct normal irradiance into a fibre optic cable. The desired target flux in this study is 85 W/cm^2 at cable outlet. The flux criterion is reported by Nakamura (2009) and drives the overall design process.

4.2 Optical system design

In the general case, the ring array is composed of *k* rings, each numbered R_1...R_k with R_1 representing the outermost element. In this methodology a ring array design may be driven by any one of four primary variables, namely aperture area (A_a), power incident on the concentrator (P), geometric concentration ratio (C), or number of rings (k). In addition there are secondary variables that must be defined, (Figure 4.1) including outer radius of R_1 (r_o); numerical aperture of optical waveguide (NA); height of R_1 (h_r); thickness of rings (t); gradient factor (GF) and the optical waveguide outlet radius, (r_{OWout}).

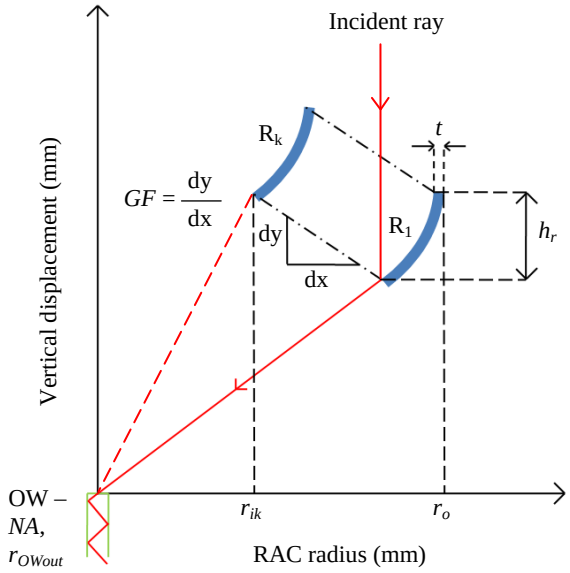

Figure 4.1 Secondary design variables for a ring array concentrator integrated with an optical waveguide.

The outer radius of R_1 (r_o) is used together with other variables to obtain the inner radius of R_k (r_{ik}). The dimensions of the concentrator are determined differently, depending on which of the four primary driving variables is used.

1. Design based on aperture area: Aperture area is defined as the projection of the reflective area on a plane perpendicular to the sun's rays (Figure 4.2). Together r_o, r_{ik} and the sum of the areas for each element's thickness, $\sum_{R_k}^{R_1} A_t$ characterise the aperture area of the RAC (Equation 4.1).
2. Design based on solar power: Equation 4.2 is used where power is the product of the aperture area and irradiance. The irradiance is assumed to be 850 W/m^2, as is generally accepted (Jaramillo et al., 2008).
3. Design based on geometric concentration ratio: Equation 4.3 is used which is the ratio of the aperture area, A_a, to the optical waveguide outlet area, A_{ow}.
4. Design based on number of rings: k is defined and ring geometry is calculated using the secondary variables previously specified.

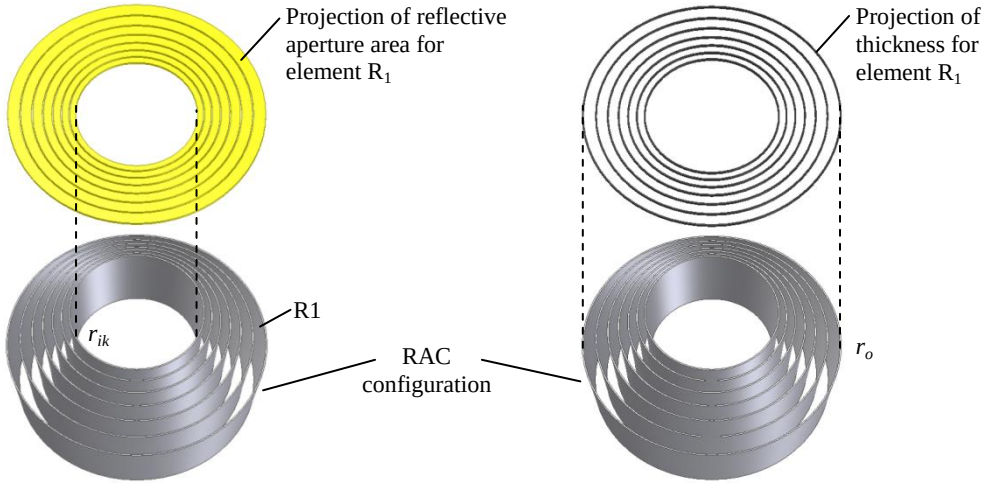

Figure 4.2 (left) Top view of a ring array configuration illustrating the aperture area, A_a, in yellow and (right) the seven black projections of each element's thickness, A_t, which do not contribute to the collection of energy.

$$A_a = \pi(r_o)^2 - \pi(r_{ik})^2 - \sum_{R_k}^{R_1} A_t \quad (\text{mm}^2) \quad (4.1)$$

$$P = \left(\pi(r_o)^2 - \pi(r_{ik})^2 - \sum_{R_k}^{R_1} A_t\right) * 0.00085 \quad (\text{W}) \quad (4.2)$$

$$C = \frac{A_a}{A_{ow}} = \frac{\pi(r_o)^2 - \pi(r_{ik})^2 - \sum_{R_k}^{R_1} A_t}{\pi(r_{OWout})^2} \quad (4.3)$$

A necessary condition for the integrated concentrator and optical transmission system is that all incident light on the aperture area of the RAC must be reflected into the waveguide located at the focal point. To achieve this, the maximum permissible half-angle, α, of a reflected ray is calculated using Equation 4.4, where n is the index of refraction of the medium in which the lens operates. Angle α defines a solution line for the inner radius (r_i) of R_1, from the inlet of the waveguide (Figure 4.3 left).

$$NA = nsin\alpha \tag{4.4}$$

Point A in the diagram is a logical start point in the design of a ring as it uses the maximum half-angle of the waveguide. However, anchoring the array at this point may conflict with the required outer radius, thus point B (Figure 4.3 right) is used as a starting point, which fixes the working variable α_{trial}. From Figure 4.3 right, θ must be determined iteratively so that α_{trial} tends to α and all dimensional constraints, being the primary and secondary variables, are met. This approach ensures optimal use of the waveguide half-angle.

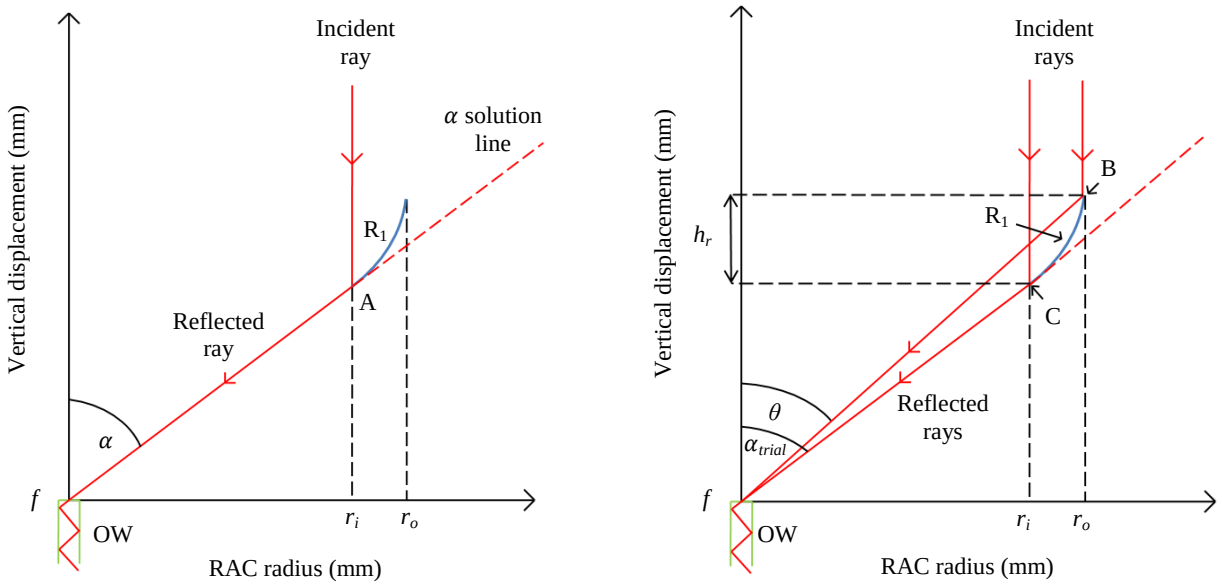

Figure 4.3 The maximum half-angle α solution line (left) and design angles, θ and α_{trial} for reflection of light into the optical waveguide (right).

For each ring the angle of incidence, β_i, must equal the angle of reflection, β_r (Figure 4.4). For this to occur a tangent line is drawn at the anchor point B. The normal to the tangent line then bisects the angle

between the incident ray and the reflected ray. Of most interest in determining the shape of R_1 is the surface angle, γ, between the tangent line and the incident ray. This is used to obtain the gradient at point B, m_B (Equation 4.5).

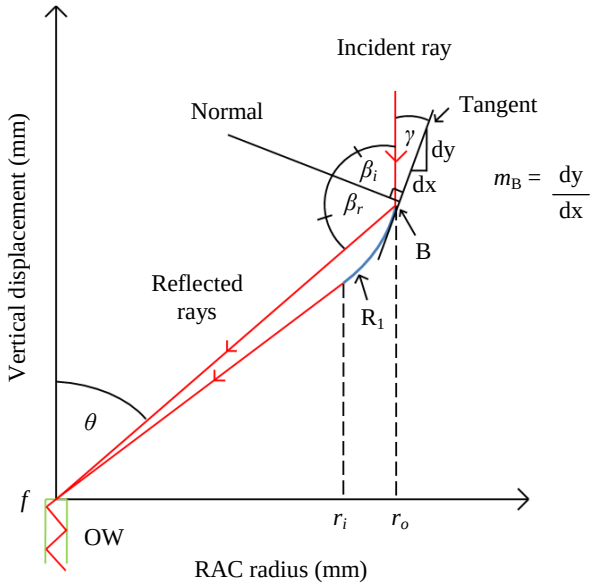

Figure 4.4 Angles of incidence, β_i, and reflected, β_r, rays. From these angles the surface angle, γ, of R_1 is obtained.

$$m_B = \frac{dy}{dx} = \tan(90 - \gamma) \tag{4.5}$$

The rings of the RAC are parabolic in cross-sectional profile to achieve point convergence of light. With γ known, the geometry of R_1 can be calculated from Equations 4.6, 4.7 and 4.8. Parameter a_1 is obtained by substituting m_B for y_1' and r_o for x_1. The focus of R_1 is calculated using Equation 4.8. The surface parabola is plotted using as a constraint the secondary variable for the ring height, h_r (Figure 4.3 right). Once the geometry of R_1 has been calculated, α_{trial} is checked against α and if necessary a further iteration is completed. In this way R_1 is correctly positioned to meet the requirements of the waveguide and the driving dimensional constraints.

$$y_1 = a_1 {x_1}^2 \tag{4.6}$$

$$y_1' = 2a_1 x_1 \tag{4.7}$$

$$f = \frac{1}{4a_1} \tag{4.8}$$

In order to constrain the paraboloidal elements a support rib structure is included. The structure is a diagonal strip defined by a lower support line starting from the bottom co-ordinate of R_1, (point C, Figure 4.5 left). The slope depends on a specified gradient factor or *GF*. Each ring terminates at the intersection of the support line. An upper support line starts at the top co-ordinate of R_1 (point B). In design terms a high *GF* means a tall RAC and a low *GF* a squat one. The methodology used here incorporates a check for interference between ring elements.

The criteria that must be met for placement of the remaining rings are: 1) that the rings are parabolic, 2) that the rings are bounded by the upper and lower support lines and 3) that the rings are closely packed to prevent light rays from penetrating between them. These criteria ensure an efficient design. Rings R_2 to R_k are positioned sequentially from outside in by simultaneously solving Equations 4.9 and 4.10 until a ring inner radius (r) equal to or less than r_{ik} is reached, thereby ensuring that A_a, P and C exceed the driving minima (Figure 4.5 right). Each element is bounded by the upper and lower support rib lines and focuses to the same point at f.

$$y_k = a_k {x_k}^2 - c_k \tag{4.9}$$

$$f - c_k = \frac{1}{4a_{1k}} \tag{4.10}$$

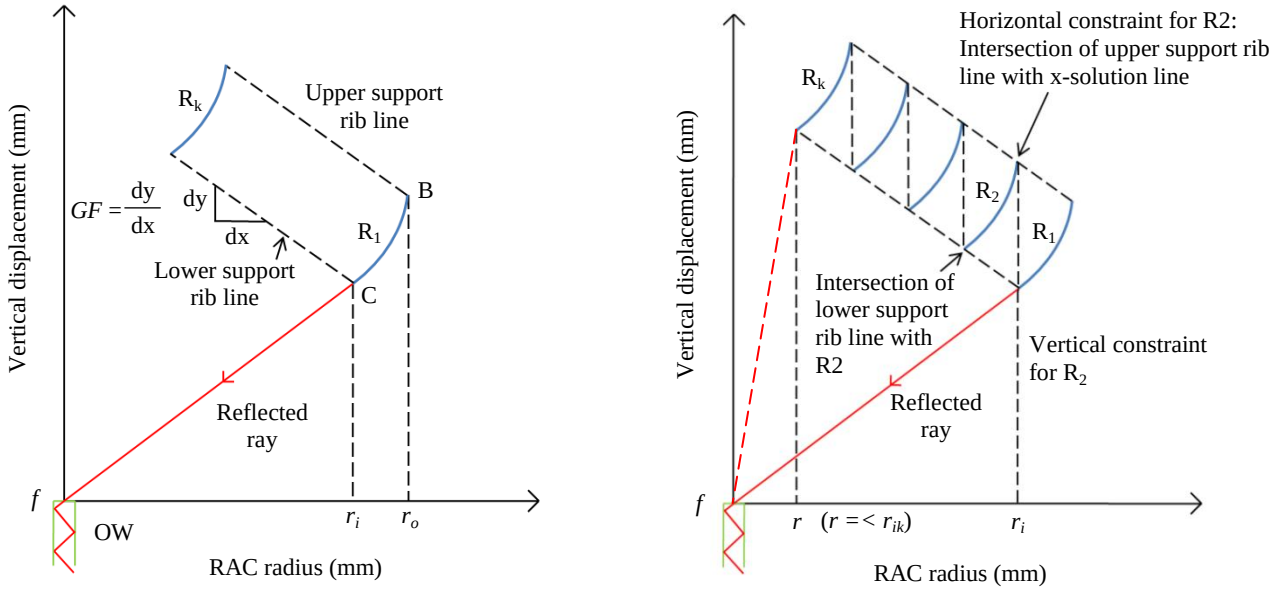

Figure 4.5 Support rib structure (left) and design of the remaining rings (right).

4.3 Design tools

The design methodology for the optical system is implemented in MATLAB for the integrated ring array concentrator and optical waveguide transmission system. The software programme is named the Concentrating Optics Design Code (CODeC) and can be used to obtain a variety of two and three-dimensional design tools to assist in selecting a solar thermal optical system for a particular application (Appendix A). The tools are developed by varying certain input parameters (independent variables) while keeping all other design variables constant to obtain a solution space for a concentrating system.

Examples of two-dimensional design tool results are illustrated in Figures 4.6 and 4.7. The figures show the output of the number of ring elements required for a varying concentrator radius, constant primary design variable and constant remaining secondary variables. As an example in using a two-dimensional design tool, Figure 4.6 shows that for a constant geometric concentration ratio of 5000 at a concentrator radius of 400 mm, with all other variables kept constant, the optical system requires five paraboloidal elements. Other dimensional outputs are distance to focal point and concentrator inner radius, r_{ik}. Knowledge of these dimensions can determine if the design is feasible for production when conducting manufacturing, cost and space constraint studies.

In addition three-dimensional design tool results illustrated in Figures 4.8 and 4.9 can be developed using similar methods. Each figure shows three surface solutions of an optical system solved using CODeC. An optical system can be selected by choosing a surface solution and any two variables on either axis. The corresponding result on the third unselected axis is the outcome of the previously selected variables. All other secondary variables are constant. For example, using Figure 4.8, for a RAC outer radius of 600 mm, a numerical aperture of 0.44 and five ring elements the optical system would have 520 W of power incident on the concentrator. In a similar manner an optical system with three surface solutions of k = 5, 7 or 9 can be selected with variables of geometric concentration ratio (C), numerical aperture (NA) and RAC outer radius (r_o) (Figure 4.9).

For this research a two-dimensional design tool was developed to select a solar thermal optical system. The RAC solution space included varying the outer concentrator radius with a constant ring number of seven. Geometric dimensions and performance outputs were analysed in selecting the final design for construction.

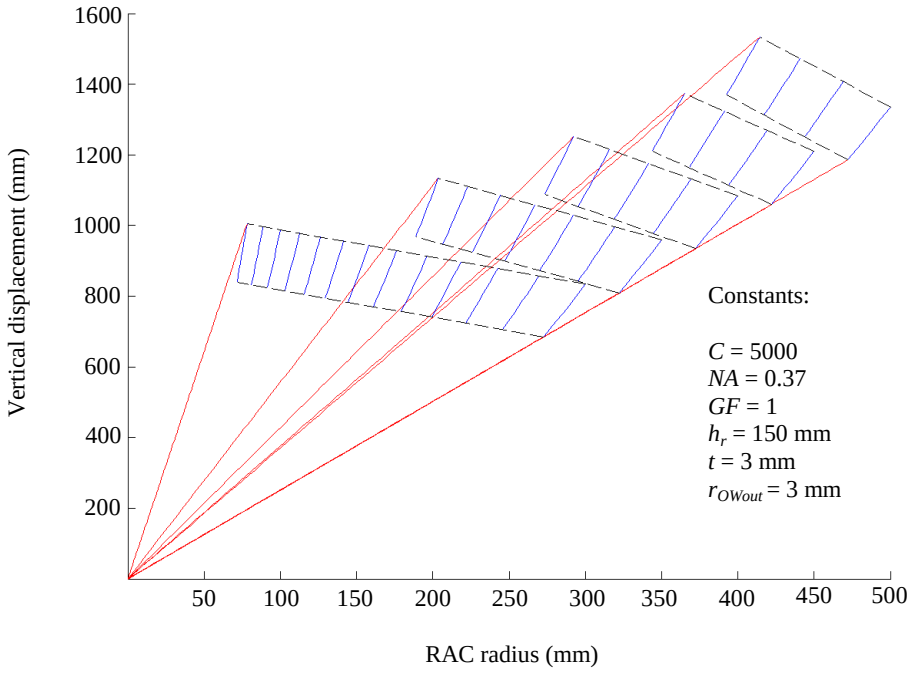

Figure 4.6 A two-dimensional solution space for five radii ring array configurations with constant geometric concentration ratio of 5000. The output of number rings shows manufacturing feasibility. All related secondary variables are constant.

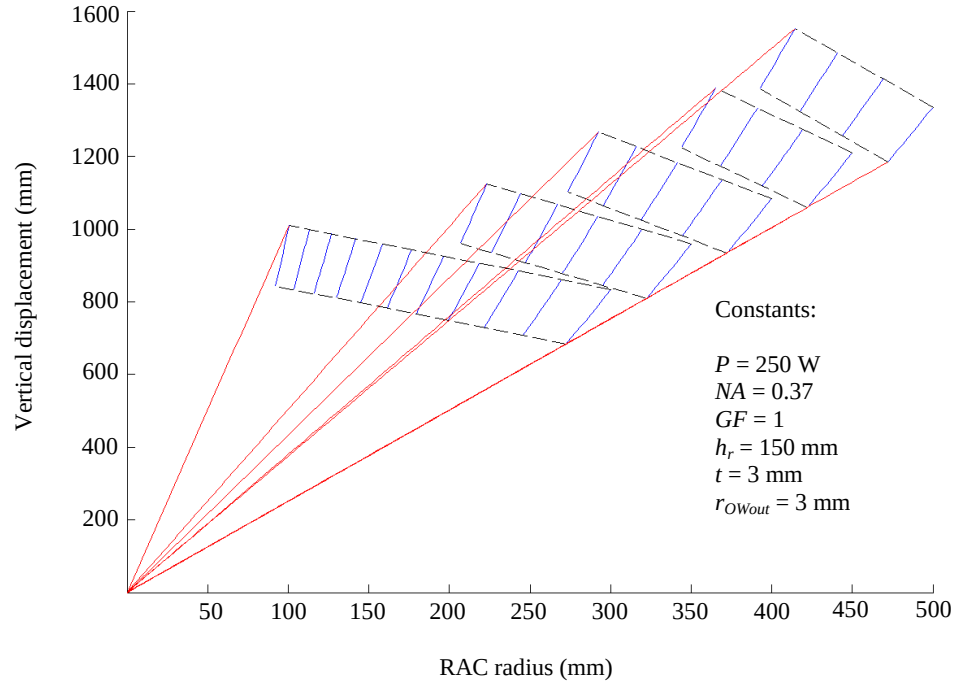

Figure 4.7 Two-dimensional solution of CODeC supplying a constant RAC aperture power of 250 W for five ring array systems. The number of elements required for each radius is shown. All related secondary variables are constant.

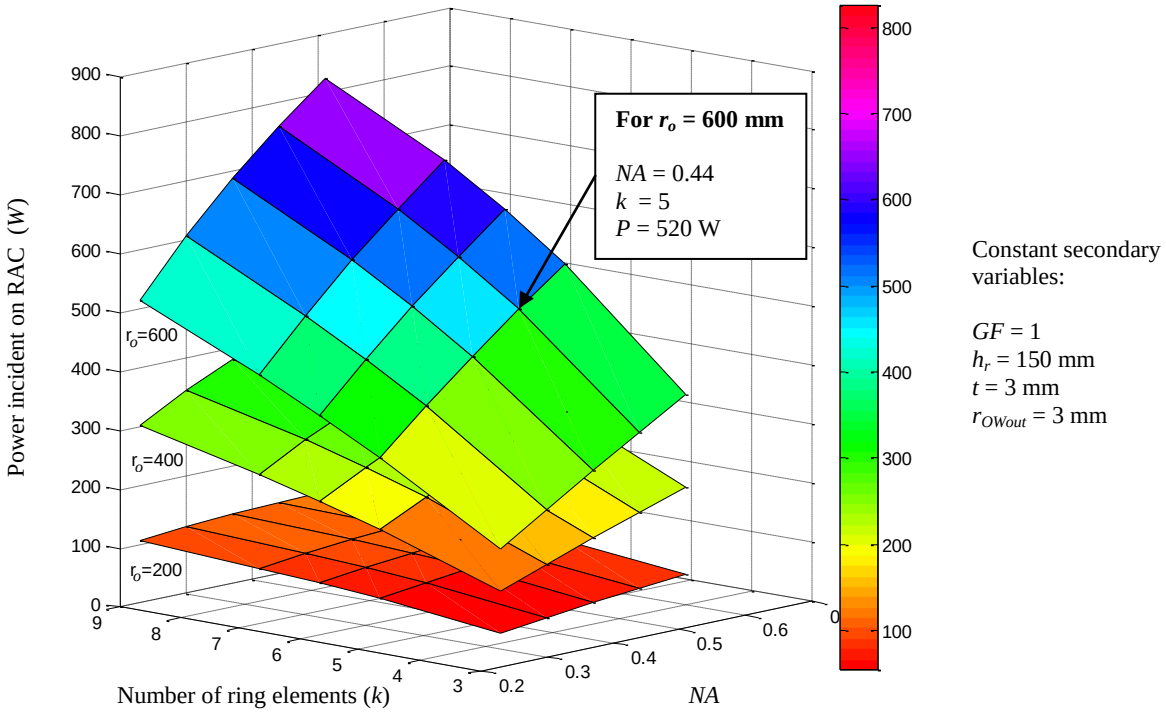

Figure 4.8 Three-dimensional solution surfaces of varying radii (r_o = 200 mm, 400 mm or 600 mm). Variables to select an optical system include numerical aperture, number of ring elements and power. All related secondary variables are constant.

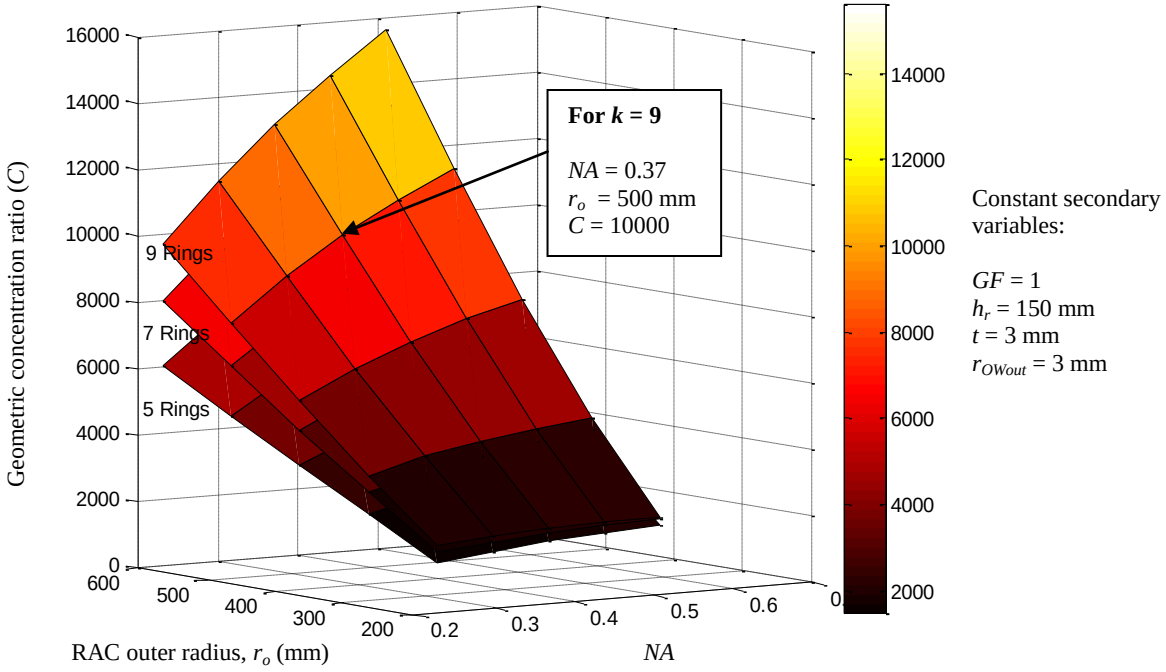

Figure 4.9 Three-dimensional surface solutions for an optical system with varying number of rings (k = 5, 7 or 9). Selection variables include numerical aperture, RAC outer radius and geometric concentration ratio. All related secondary variables are constant.

4.4 Design selection

A design is proposed for a combined ring array concentrator and fibre optic energy transmission system based on CODeC. The optical system is required to achieve a flux of 85 W/cm^2 stipulated by Nakamura and Smith (2009) for melting lunar regolith. The desired flux is intended for use in high temperature terrestrial and space applications, such as lunar ISRU research.

The methodology in selecting a design includes considerations for manufacturing, cost and spatial constraints. The ring array configuration comprises a set of paraboloidal elements. Manufacturing numerous elements increases costs and causes difficulties in the support structure design. The prototype optical system is chosen to have seven paraboloidal elements for further investigation. CODeC is used to obtain a two-dimensional design tool with a constant ring number (k) of seven and secondary design variables given in Table 4.1.

Table 4.1 Design parameters for proposed ring array concentrator and fibre optic transmission system. The primary design variable is chosen to have seven reflective elements.

	r_o (mm)	*NA*	h_r (mm)	t (mm)	*GF*	r_{OWout} (mm)
Values	From 200 – 600	0.37	150	3	1	3
Notes	Defines a solution space for a system with seven elements	Available waveguide	Practical height for a ring element	Practical thickness for a ring element	Practical slope for ring elements	Available waveguide

The solution space for a seven-ring array optical system with the above secondary variables is shown in Figure 4.10. Resulting CODeC outputs of aperture area, power, geometric concentration ratio and related dimensions are given in Table 4.2. In selecting an array configuration, any one of the sample designs would meet the seven ring requirement, but not necessarily the nominal flux. Manufacturability is also a concern and the trade-off between construction efforts and collection of energy must be beneficial. The width of the inner ring should not become too small as this would collect a small amount of energy for construction efforts. Larger diameter arrays have wider elements however the overall size of the device becomes problematic. For example, the 600 mm radius RAC has a focal length of almost 1.5 m making the support structure unwieldy. In addition, optical errors are likely to increase for the larger arrays because light must travel further from the reflective surface to the focal point. To support the selection of

a feasible design, a ray tracing exercise was conducted to obtain representative performance results of concentrators having different focal lengths, as shown in Chapter 6. Concentrator radius configurations of 300 mm and 500 mm were chosen for comparison. Results show the smaller array concentrator as having superior performance, suggesting optical errors in the 500 mm radius configuration are due to a longer focal length. Given the optical error problems associated with the larger designs a concentrator array of 300 mm radius was selected for construction and geometrically analysed to obtain predicted performance results.

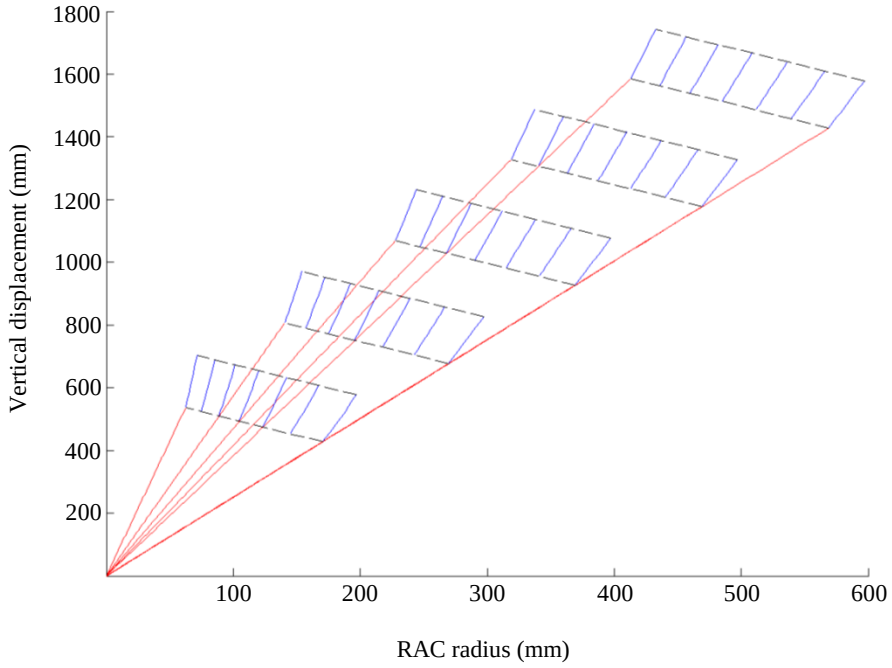

Figure 4.10 Solution space for the proposed optical system of seven reflective rings concentrating sunlight into an optical waveguide of numerical aperture 0.37.

Table 4.2 Critical dimensions for a proposed array with constant ring number of seven and varying radius.

		Concentrator height, h_r (mm)	**Aperture Area, A_a (mm^2)**	**Outer diameter, r_o (mm)**	**Inner diameter r_{ik} (mm)**	**Geometric concentration ratio, C**	**Power incident on RAC, P (W)**	**Focus from ring 1 (mm)**	**Width of last ring (mm)**
Radius (mm)	600	314.4	5.28E+05	1200	825.6	18672	448.7	1428.6	19.8
	500	309.8	4.11E+05	1000	637.8	14545	349.6	1177.8	18.4
	400	303.2	2.98+E05	800	454.9	10550	253.6	927.2	16.4
	300	293.0	1.92E+05	600	280.9	6777.0	163.2	677.0	13.5
	200	275.5	0.97E+05	400	124.8	3414.7	82.0	427.7	9.0

5. CONSTRUCTION PROCESS

5.1 Introduction

An important factor affecting the performance of a point focus solar collector is the accuracy of the reflective paraboloidal surface. While a range of construction methods may be followed in producing reflective surfaces, the lower cost approaches inevitably lead to a reduction in performance due to the use of non-specialised equipment. A limited performance reduction may be acceptable if the trade-off against mass or cost is justifiable. This research aims to construct a low-cost solar collector to achieve high-flux concentrations required in high temperature processes.

Three methods for constructing a point focus concentrator of the ring array type were considered. In the first method, described by the developers of the ring array configuration, a centrifugal forming process is used for the ring elements in a vessel with circular partition walls (Vasylyev, 1981). This is a preferred method owing to the axisymmetrical geometric properties of the resulting elements, however it is expensive and requires complex manufacturing techniques. Another method is to machine each element from a billet of aluminium, using a computer numerical control (CNC) lathe to ensure accuracy of the inner reflective surface. Even if material is conserved in this approach by using off-cuts from the larger elements to produce the smaller rings, the costs are high. An example of a CNC lathe process is diamond turning of aluminium. Feuermann et al. (2002) and Nakamura and Senior (2008) used this process to machine paraboloidal dishes to a root mean square (rms) mirror slope error of 0.1 mrad. This process is expensive because of the materials and equipment involved, and suggests a need for novel, lower-cost construction methods using composite materials. Such an approach has been followed here in the development of the ring array concentrator.

Elements are constructed using composite materials and a mould. This approach is attractive because of the potential reductions in cost and weight. Cost of construction of the composite material ring array was estimated to be one eighth the price of machining each ring from aluminium, and 3 kg lighter overall. Composite materials are used extensively for their specific properties of strength, stiffness and compressibility which permit novel methods for product design (Teti, 2002). Their mouldable characteristics potentially allow for shaping of solar reflective surfaces with acceptable magnitudes of surface slope error, while keeping manufacturing costs low compared to existing methods. Previous collectors constructed with composites include a parabolic trough designed and tested by Arasu and

Sornakumar (2007) using the hand lay-up method. Surface slope errors of the trough estimated to be 6.6 mrad. In addition Johnston (1998) designed and constructed a parabolic dish using composites to achieve a surface slope error of 2.0 mrad. Using adhesive, he fixed 2300 flat mirrors on to a fibreglass shell that was cast on a paraboloidal mould.

The construction aim in this research is to construct a prototype low-cost solar concentrator of the ring array design, using composite materials for injection of solar energy into a fibre optic waveguide. Polymer matrix composites in the form of fibre reinforced plastics (FRP) are used as the materials for construction of the reflective elements. Video footage demonstrating the construction process is supplied in a compact disc at the back of this dissertation.

5.2 Construction of reflective elements

The composite material hand lay-up method was employed for the construction of each element, which is formed from a matrix material and two reinforcement materials to produce a FRP composite. The matrix material is a thermosetting polymer and distributes the stress to the reinforcement materials, providing the final shape of the element (Teti, 2002). The reinforcement materials consist of glass and carbon fibres which provide the composite with high mechanical properties and reinforce the matrix in preferential directions. The mould bearing the paraboloidal geometry of each element is made from easily machineable Necuron 651 tooling board (Figure 5.1, left). Starting with the largest diameter ring, the mould is machined using a CNC lathe and the lay-up is completed for that element (Figure 5.1, right). The subsequent rings are constructed one at a time by machining down the tooling board. The reflective surfaces of the ring array are laser cut into seven conic profiles from Miro 4 aluminium (Alanod, 2011) of high specular reflectance and 0.4 mm thickness (Figure 5.2, left). The aluminium is strapped on to the mould and bonded together at the join using Spabond 370 as the adhesive and a rectangular sheet of aluminium as the connector (Figure 5.2, right). The mould is vacuum bagged to allow the aluminium to form the shape of the paraboloid. Aluminium tabs are used on the top surface of the mould to constrain the profile when applying the vacuum. After curing, silicone is beaded around the inner and outer diameters of the element to prevent resin seeping between the mould and profile surface. Glass and carbon fibre profiles are hand impregnated with resin and applied over the aluminium profile (Figure 5.3, left). Glass fibre is laid on first to eliminate corrosive interaction between the carbon fibre and aluminium. A thin layer of adhesive is applied to the aluminium to allow the glass to bond with the metal surface before four layers of carbon fibre are applied. The use of peel ply ensures a smooth finish of the element, after which perforated film and bleeder are applied to drain excess resin. Two hours after the epoxy resin

is mixed, a vacuum bag is applied to improve consolidation and allow for additional pressure forming of the aluminium on to the paraboloidal mould (Figure 5.3, right). The lay-up is left to cure for 24 hours before demoulding using the carbon fibre tabs to produce the seven FRP elements (Figure 5.4). The concentration of sunlight with a completed reflective FRP element is illustrated in (Figure 5.5).

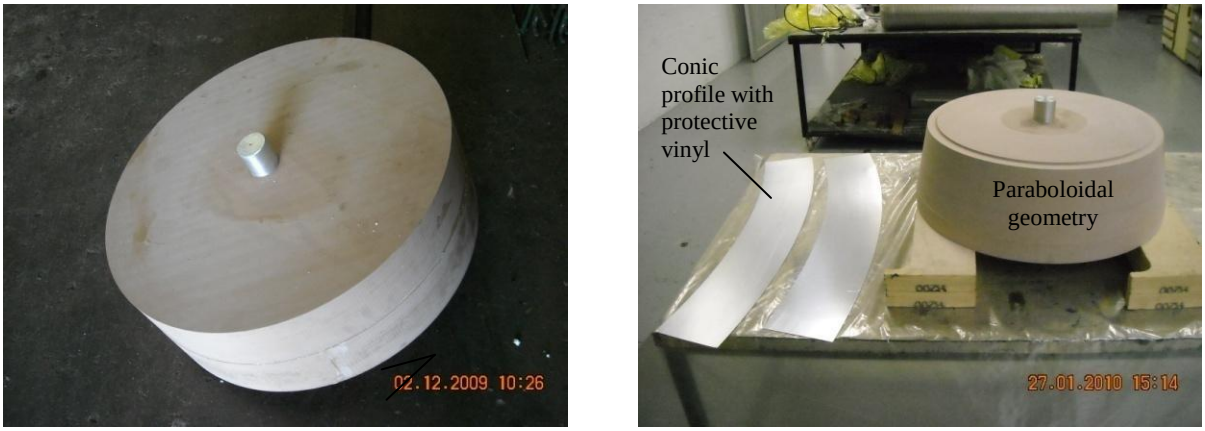

Figure 5.1 (left) Tooling board mould constructed to machine paraboloidal profiles for the reflective elements and (right) machined geometry for element #1 (largest element) with conic aluminium profiles.

Figure 5.2 (left) Developed conic profiles of Miro 4 polished aluminium for the elements. (right) Profile for element #7 strapped to the tooling board mould before first lay-up. A vacuum is applied during bonding of the aluminium over the mould to enforce the paraboloidal shape.

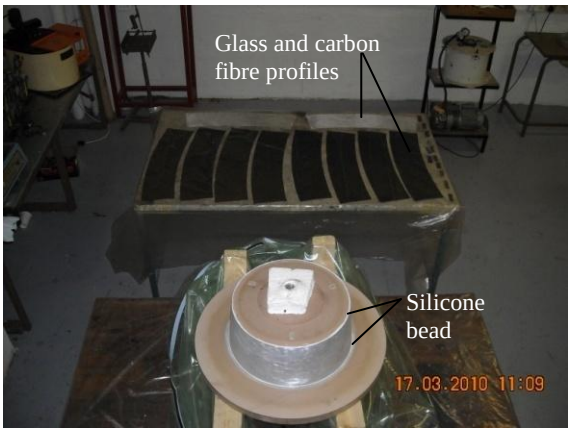

Figure 5.3 (left) Aluminium profile after bonding with a bead of silicone to prevent resin offset between the metal surface and mould. Glass and carbon fibre profiles were hand impregnated with resin for the wet lay-up and second vacuum bagging process. (right) Second vacuum bag process with peel ply, perforated film and bleeder surrounding the lay-up to improve the composite finish.

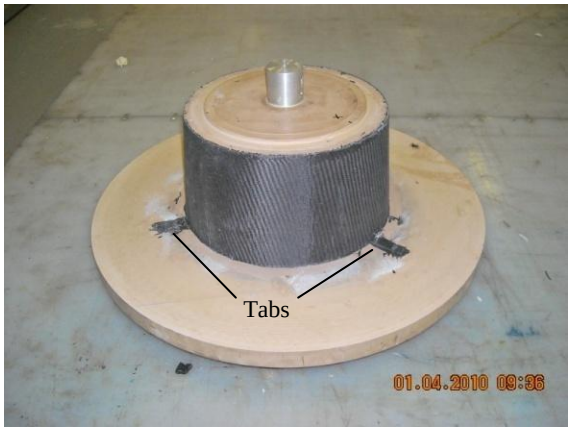

Figure 5.4 (left) After curing vacuum is removed and the element is demoulded using tabs. (right) The completed seven FRP elements #1 to #7, anticlockwise from back right.

Figure 5.5 A completed reflective element focusing incident rays to a point.

To ensure a rigid and thin element, the composite lay-up consists of five layers: one layer of 163 g/m^2 glass fibre, two layers of 2 x 2 twill 200 g/m^2 carbon fibre and two layers of unidirectional (UD) 300 g/m^2 carbon fibre. A low shrinking epoxy resin system, LR20/SLC 60, is employed to minimise shrinkage post curing. The properties of the epoxy resin system used for the wet lay-up are given in Table 5.1. The area of the fibre profiles with the values for the amount of resin used for each element is given in Table 5.2. These values are calculated considering the area of laminate, fibre volume fraction of a wet lay-up, density of fibres, mass of fibres, layers of fibres, and density of resin.

Table 5.1 Physical, mechanical and heat resistance properties of low shrinking LR20/SLC60 laminating epoxy resin system.

	Resin (LR20)	**Hardener (SLC60)**	**System**
Mix ratio (Parts by weight)	100	25	
Density at 25°C (g/cm^3)	1.13	0.94	1.09
Demould time at room temperature (hrs)	-	-	24-38
Compressive strength (MPa)	-	-	120 ± 5
Tensile strength (MPa)	-	-	65 ± 5
Flexural strength (MPa)	-	-	130 ± 5
Flexural modulus of elasticity (MPa)	-	-	3500 ± 200
Elongation at break (%)	-	-	5.0
Heat distortion, Tg (°C)	-	-	98
Fibre volume fraction for wet lay-up (%)	-	-	33

Table 5.2 Area of laminate and mass of resin used for hand impregnating the fibre profiles. Total mass of the completed concentrator is 5.1kg.

		Fibre profile area for one lay-up (mm^2)	**Resin mass – two layers UD carbon fibre (g)**	**Resin mass – two layers 2 x 2 twill carbon (g)**	**Resin mass – one layer glass fibre (g)**	**Extra mass of resin (peel ply) (g)**	**Total mass of resin (g)**	**Hardener mass (25% of resin) (g)**	**Total mass (g)**
Ring element	#1	280739.6	214.7	143.1	21.7	21.7	401.3	100.3	950.4
	#2	257184.9	196.6	131.1	19.9	19.9	367.6	91.9	860.0
	#3	235118.6	179.8	119.8	18.2	18.2	336.1	84.0	754.0
	#4	214752.4	164.2	109.4	16.6	16.6	307.0	76.7	700.7
	#5	195859.1	149.7	99.8	15.1	15.1	279.9	70.0	661.8
	#6	178407.7	136.4	90.9	13.8	13.8	255.0	63.7	615.1
	#7	162356.3	124.1	82.7	12.5	12.5	232.0	58.0	561.1

A rigid support structure is machined from aluminium to house the fibre reinforced plastic elements (Figure 5.6). The support permits adjustment in concentric alignment and vertical off-set of the seven reflective elements, to converge sunlight to a common focal point.

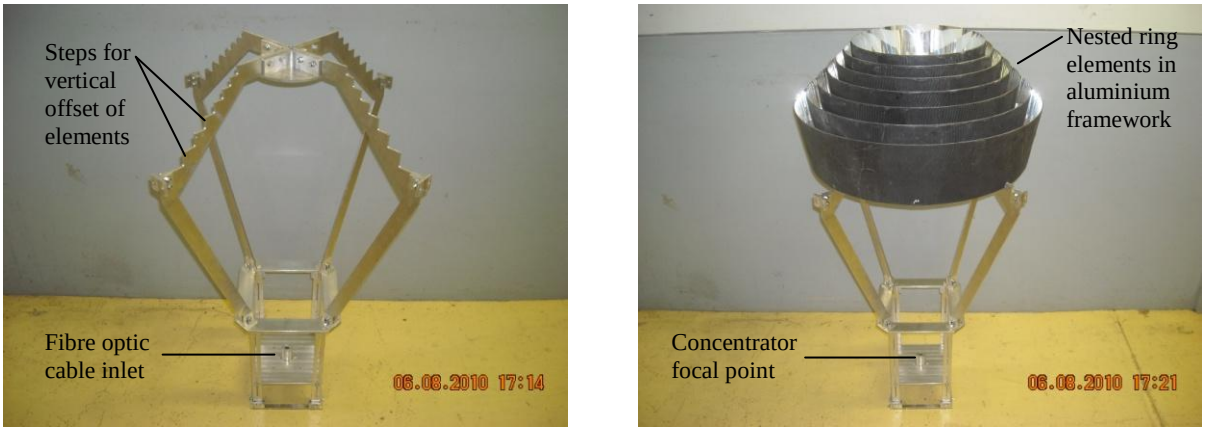

Figure 5.6 Machined aluminium framework to house reflective elements and fibre optic cable (left). Fibre reinforced plastic reflective elements nested in support framework (right).

6. ERROR ANALYSIS

6.1 Introduction

Optical characterisation of the elements is necessary to quantify the low-cost, composite material construction method. Errors in point focus concentrators result in the spread of the focal point and decrease the power density of the system. A high power density is required at fibre optic cable exit and an error analysis is conducted to predict performance losses of FOCUS. Factors contributing to the spread at the focal point include the sun's finite angular size, optical errors and pointing errors. Optical errors include imperfect specular reflection from the reflective surface and slope error inaccuracies in the paraboloidal geometry, while pointing errors result from tracking and receiver misalignment (Stine and Harrigan, 1985). Ray tracing simulations were conducted to directly model the solar half-angle, imperfect specular reflection and misalignment errors while slope errors were obtained by measurement, after which they were incorporated in the ray tracing simulations.

The design methodology for the RAC configuration was implemented assuming incident light rays being parallel. However an incident ray of direct normal irradiance has a cone of angular width 0.53° (Duffie and Beckman, 2006). Figure 6.1 illustrates the effect of this angle on an optically perfect reflective ring array element. Independent errors due to imprecise geometry of the reflective elements result in slope errors and cause the majority of optical errors in point focus systems.

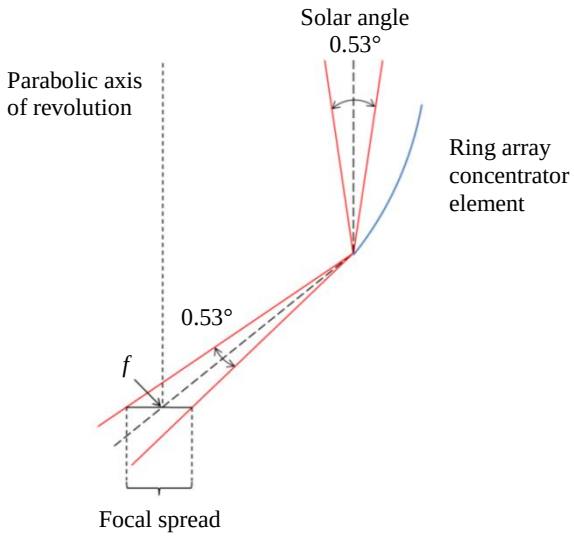

Figure 6.1 Cross-sectional view of the reflection of direct normal irradiation from an optically perfect paraboloidal element of a ring array concentrator.

6.2 Optical error analysis

6.2.1 Slope error

A slope error analysis of a solar concentrator aims to verify the match between the ideal geometry required and the realised geometry obtained through the construction process. Slope error evaluation in solar concentrating systems is a critical exercise due to the doubling error effect of Snell's law. Characterising optical errors using slope measurements includes obtaining angular deviations between ideal and realistic perpendicular lines along points on a curved surface (Stine and Harrigan, 1985) (Figure 6.2). Several methods have been developed for accurate slope error (φ) measurements of point focus solar collectors, mostly requiring complex metrology equipment. Some methods include photogrammetry (Pottler et al., 2005; Shortis and Johnston, 1996), laser ray tracing such as the Scanning Hartmann Optical Test (SHOT) (Wendelin et al., 1991) and its successor the Video-SHOT (Jones, 1998), surface topography characterisation, and distant observer techniques using digital cameras and colour-coded targets (Ulmer et al., 2008). In this study a three-dimensional (3D) co-ordinate measuring machine (CMM) was used to measure surface topography (Kumler and Caldwell, 2007; Menq and Chen, 1996).

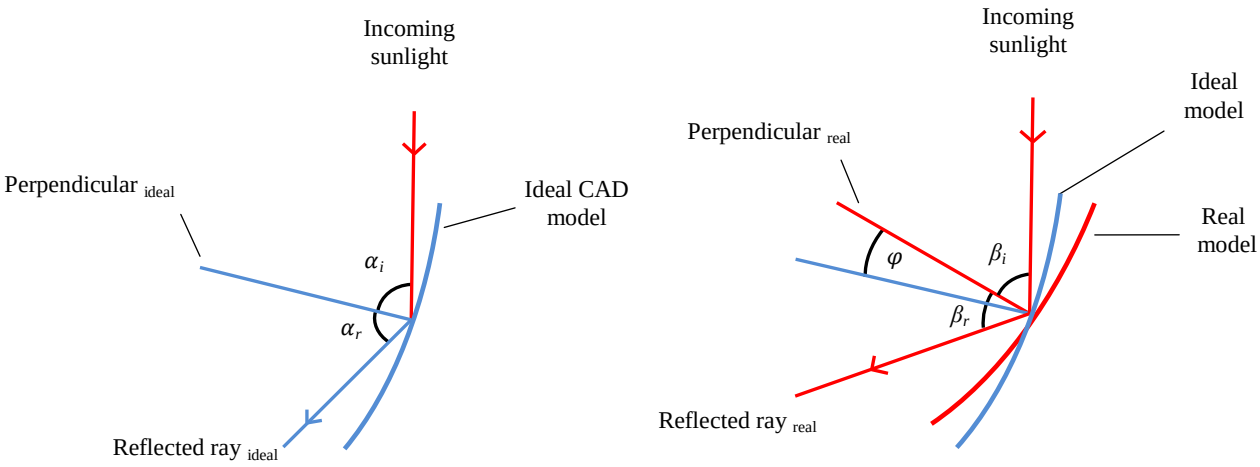

Figure 6.2 (left) Schematic of ideal angles of incidence (α_i) and reflected rays (α_r). (right) Angles of incidence (β_i) and reflected rays (β_r) arising from the inaccuracies in the construction process yielding a slope error (φ).

6.2.2 Surface topography measurements

The CMM provides scanned profiles of the reflective surface for each ring element before processing the results to obtain slope error. It has three main components: the three axes of motion structure; a contact

profilometer (Renishaw PH10M) using direct computer control (DCC) with 1.9 µm accuracy; and measuring and analysis software (PC-DMIS). The measurement method includes obtaining a concentric reference on an element, after which four profile scans (+X, -X, +Y, -Y) 90° apart are measured and compared to the ideal CAD model for a real time horizontal deviation analysis (Figure 6.3). Each profile comprises 98 data points. Further analysis is done in a 3D modelling package to obtain surface slope errors for each profile scan by matching the realistic curve to the ideal. A statistical analysis was conducted to determine if the four profiles had similar trends in order to obtain a representative slope error value per element.

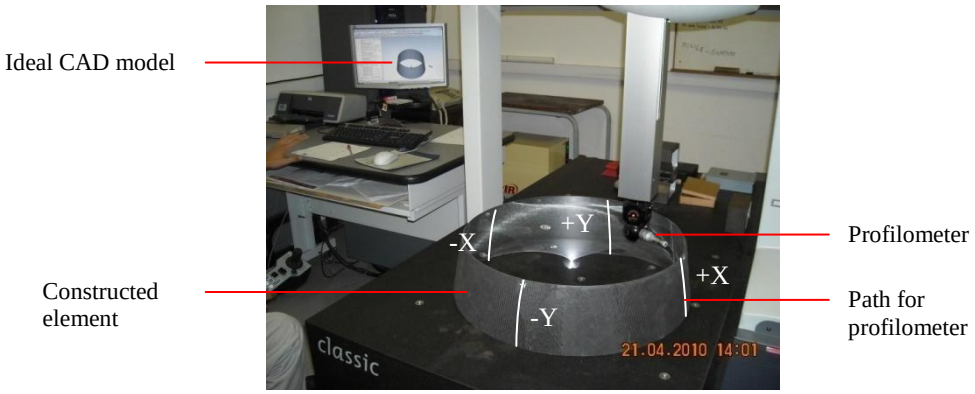

Figure 6.3 Four profile scans (+X, -X, +Y, -Y) using a contact profilometer were measured and compared to the ideal CAD model to optically characterise each paraboloidal surface. Each scan measured 98 points on the reflective surface.

6.2.3 Statistical analysis

The resulting four profile slope errors were examined using statistical methods to obtain a representative slope error value for each element. The methodology uses the NIST/SEMATECH e-Handbook of Statistical Methods (2010) with assistance from UKZN's School of Statistics and Actuarial Science.

A one-way analysis of variance (ANOVA) test consisting of hypothesis testing was conducted using Equations 6.1 and 6.2 to determine if the profiles had similar trends. The null hypothesis assumes all four profile means (μ_{+X}, μ_{-X}, μ_{+Y}, μ_{-Y}) are equal while the alternative aims to prove at least two of the means differ. The criterion used for rejecting the null hypothesis is the level of significance, $\alpha_{l.o.s}$ which is used to obtain an $F_{critical}$ value for comparison with the $F_{statistic}$ calculated from the ANOVA test. The $F_{statistic}$ for

each ring is defined as the ratio of the mean squares between (MS_B) and within (MS_W) profile scans (Equation 6.3). The ANOVA test was conducted to expect negligible variation in results at the 1% level of significance which corresponds to an $F_{critical}$ value of 3.832. The criterion in Equation 6.4 determines if profile trends have no statistical differences. A sample set of the data and results for the ANOVA test for element #7 is shown in Appendix B.1. Results for the seven ANOVA tests show that H_o failed to be rejected at the 1% level of significance suggesting profile trends have no statistical significant differences (Table 6.1). The profiles were pooled to obtain a sample of 392 observations, N for each element to obtain a single representative rms slope error value.

Null hypothesis $$H_o: \mu_{+X} = \mu_{-X} = \mu_{+Y} = \mu_{-Y} \quad (6.1)$$

Alternative hypothesis $$H_1: \text{At least two of the means are not equal} \quad (6.2)$$

$$F_{statistic} = \frac{MS_B}{MS_W} \quad (6.3)$$

$$\text{if } F_{statistic} > F_{critical} : \text{reject } H_o \text{ at } \alpha_{l.o.s} = 0.01 \quad (6.4)$$

Table 6.1 ANOVA test results conducted at the 1% level of significance for the seven reflective elements. An $F_{critical}$ value of 3.832 is greater than the seven $F_{statistic}$ values for the elements, suggesting no statistically significant profile differences.

Ring element	**#1**	**#2**	**#3**	**#4**	**#5**	**#6**	**#7**
$\mathbf{F_{statistic}}$	1.040	0.306	0.485	1.462	2.430	0.409	2.649

Using the 392 observations, rms slope errors, φ_{RMS}, were calculated for each element with Equation 6.5, where φ_{ideal} is the idealistic zero slope error (0 mrad) at each data point, φ_{real} is the realised angular deviation obtained through the construction process and N is the number of observations. Table 6.2 shows the slope error results of the 392 observations per ring element. The general trend in the errors shows an increase in accuracy with decreasing diameter. Slope errors between 5.67 mrad and 2.90 mrad rms were observed, which are comparable to those reported by Arasu and Sornakumar (2007) and Johnston (1998) who used similar fabrication methods for a parabolic trough and dish respectively. A statistical analysis of the data was completed to identify error outliers, which tended to cluster near the upper and lower edges of the elements. When the analysis was repeated with the statistically determined outliers excluded, an improved representation of slope error trends was obtained for the reflective elements, as a function of diameter. Slope error results between 2.21 mrad and 0.79 mrad rms were obtained (Table 6.2) with a direct correlation between the size of the reflective ring and the scale of surface slope error. This highlights the difficulty of constructing large-geometry, precision optics using composite materials. A

sample set of the outlier results for element #7 is shown in Appendix B.2. A box-and-whisker plot of the seven elements (Figure 6.4) shows the distribution of the observations and indicates where the middle 50% of the error data lie. The box-plot for element #7 (smallest reflective ring) deviates least from ideal, whereas element #1 has the most widely distributed middle data.

$$\varphi_{\mathrm{RMS}} = \sqrt{\frac{\Sigma(\varphi_{ideal} - \varphi_{real})^2}{\mathrm{N}}} \qquad \text{(mrad)} \qquad (6.5)$$

Table 6.2 Slope error results for optically characterising the seven reflective elements. Results for each element include a sample of 392 observations. Calculations were conducted excluding outliers (E/O) to provide improved slope error trends between elements. Results show smaller ring elements have improved surface geometry than larger elements.

	Ring element						
	#1	**#2**	**#3**	**#4**	**#5**	**#6**	**#7**
φ_{RMS} (mrad)	4.77	5.67	5.39	4.02	3.32	4.22	2.90
φ_{RMS} (E/O, mrad)	2.21	1.12	1.53	1.23	1.24	1.17	0.79

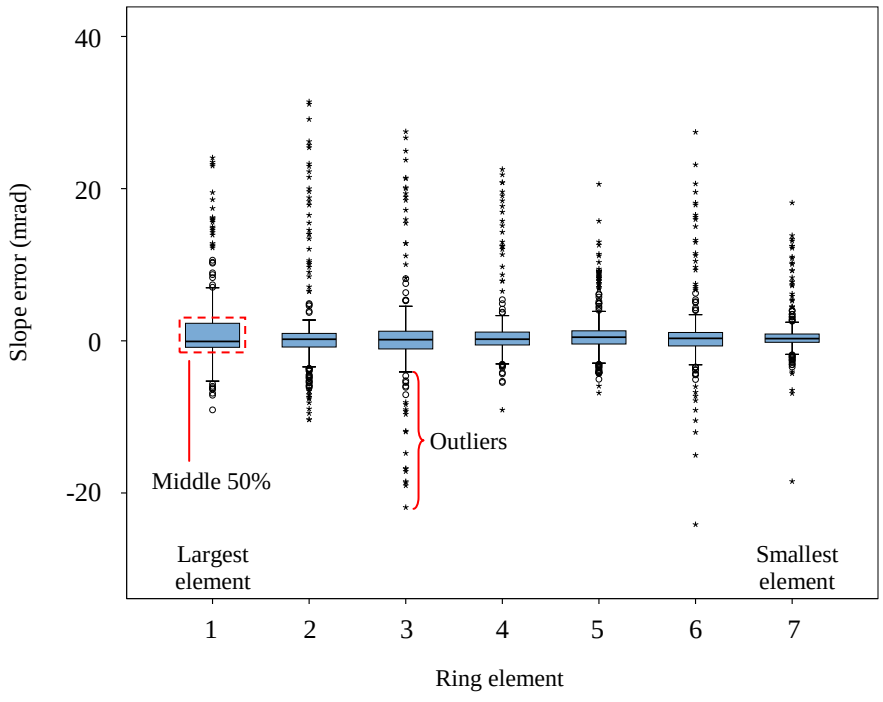

Figure 6.4 Comparative box-and-whisker plots for the seven reflective elements. Each plot represents the distribution of the observations showing outlier positions. The middle 50% of the observations represented by the blue box shows element #7 having the least distributed data indicating an improved construction process.

Several factors can cause surface errors in the constructed elements, as well as variation in error between individual elements constructed using the same method. For one, the manual wet lay-up, vacuum bagging process permits variation in the nature and extent of distortion, and can explain the range of slope error results. Resin and fibre volume fractions characterise the quality of each laminate and although a low resin laminate was desirable, the quality of the resulting part depends on the skills and consistency of the laminators. Due to the unique nature of wet lay-up processes it was difficult to produce high fibre volume fractions for the seven separate vacuum bagging processes, which potentially caused the range of errors between elements. Improved slope error results in the smaller ring elements suggests that due to the decreasing curvature, smaller elements require less shaping and pressure forming of the flat reflective aluminium to form a paraboloid. In addition the characteristic double curvature of the paraboloidal surface creates a complex manufacturing geometry in which material fibres are less likely to adhere accurately to the mould shape. The slope error results suggest that ring array designs should ideally comprise reflective elements with reduced curvatures if wet lay-up, vacuum bagging methods are employed. A thorough analysis of structural distortion during curing of the composites, which is outside the scope of this research, could lead to better lay-up design and material selection. These and other improvements would reduce surface slope errors and increase overall optical efficiency of the concentrating system. In addition to slope errors, point focus systems experience performance losses when pointing errors due to tracking misalignment occur.

6.3 Pointing error analysis

6.3.1 Misalignment error

Point focus solar concentrators experience optical loss whenever incident light deviates from the aperture normal resulting in pointing errors. Pointing errors include tracking misalignment and displacement of the receiver (Hughes, 1980). Sun-tracking strategies for solar collectors minimise tracking misalignment by maintaining optimum positioning of the collector to incident solar radiation (Cope and Tully, 1981; Wijeysundera, 1977). Tracking strategies include passive or active sun-tracking systems (Chong and Wong, 2009). Passive trackers use the thermal expansion of fluids to cause imbalances in the system that result in the correct orientation of the collector to solar rays (Mousazadeh et al., 2009). More accurate active systems use photo-sensors to sense the direction of the sun's rays and output current to the drive motors for the correct alignment of the collector. To increase collector efficiency point focus concentrators commonly use active, dual-axis tracking mechanisms such as altitude-azimuth and polar tracking systems (Mavromatakis and Franghiadakis, 2008). Dual-axis solar trackers have two degrees of

freedom to perpendicularly align the collector to direct normal irradiation. An active, dual-axis altitude-azimuth solar tracking system is used in this research to minimise efficiency losses due to imperfect focusing. The tracker is manufactured by Small Power Systems (SPS) and has an average tracking accuracy of 0.05° reported by Feuermann et al. (2002).

As part of selecting a feasible ring array configuration, as described in Chapter 4, two concentrator diameters were chosen to compare performance results as a function of differing focal length. A computational analysis was conducted to characterise the sensitivity of each RAC to misalignment errors with the SPS tracker using ray tracing software (OptisWorks Studio). The software uses Monte Carlo based methods to simulate illumination by approximating integrals using repeated random sampling (Shirley and Wang, 1992). The algorithm distributes the evaluation points uniformly over the integration region and uses importance sampling to obtain improved results for the ray tracing model. Figure 6.5 gives an overall view of the ray trace environment showing direct, parallel rays generated from a sun source and being reflected by the RAC to achieve point convergence of light at the target. The sun source is modelled as a blackbody emitting radiation in the wavelength range 320 nm to 1200 nm.

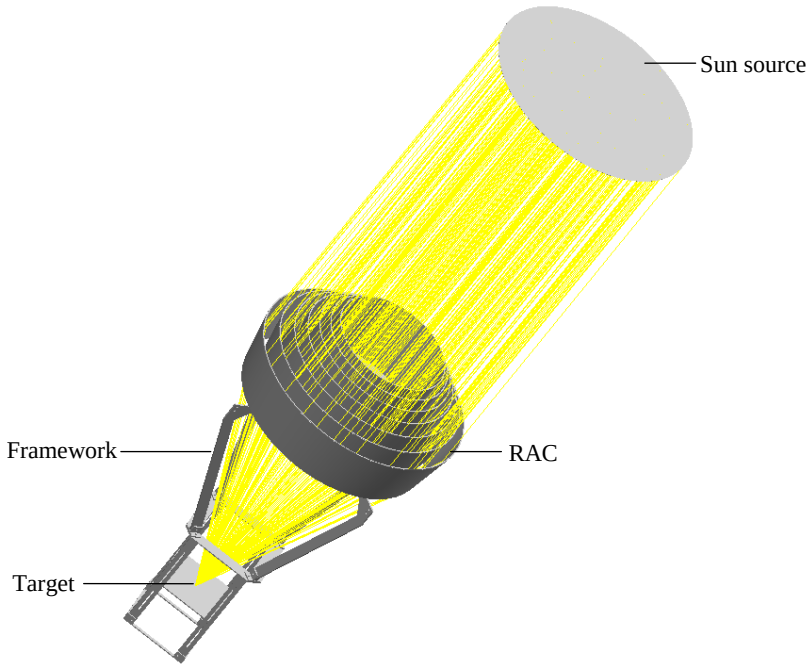

Figure 6.5 Ray tracing environment in OptisWorks Studio. A simulation of FOCUS includes modelling the concentrator, framework and creating a sun source to generate rays. The sun source is modelled as a blackbody at a temperature of 5800 K to approximate the spectral irradiance of solar radiation.

6.3.2 Ray tracing model

A ray tracing model is developed in OptisWorks Studio to simulate the performance of a RAC configuration. The procedure involves importing a three-dimensional RAC model into the ray tracing environment after which several optical parameters are selected. Optical parameters include the surface finish of components, being either reflective or absorptive. A sun source is created with the correct wavelength and diverging solar half-angle. Two ray tracing simulations, ideal and real, are conducted to compare performance for the misalignment error investigation. The difference between the ideal and realistic simulations is the modeling of the solar half-angle in the realistic case, whereas parallel rays are modelled in the ideal simulation.

A ray tracing analysis is conducted to predict the average power absorbed at the inlet to the optical waveguide (P_{OWin}) of two different ring array systems in the presence of angular misalignment, ε, relative to the sun's rays. The misalignment is representative in magnitude of the range of errors encountered with current two-axis trackers including the SPS solar tracker. The concentrator designs are sized such that each has seven reflective elements, even though the outer diameters are different. This enables a direct comparison of performance as a function of focal length and angular misalignment relative to the longitudinal axis of each array. The ring arrays investigated here have outer diameters of 0.6 m and 1.0 m and corresponding focal lengths of 0.68 m and 1.18 m respectively. In both cases light is focused from optically perfect paraboloidal elements on to the inlet end of the fibre optic bundle (Figure 6.6).

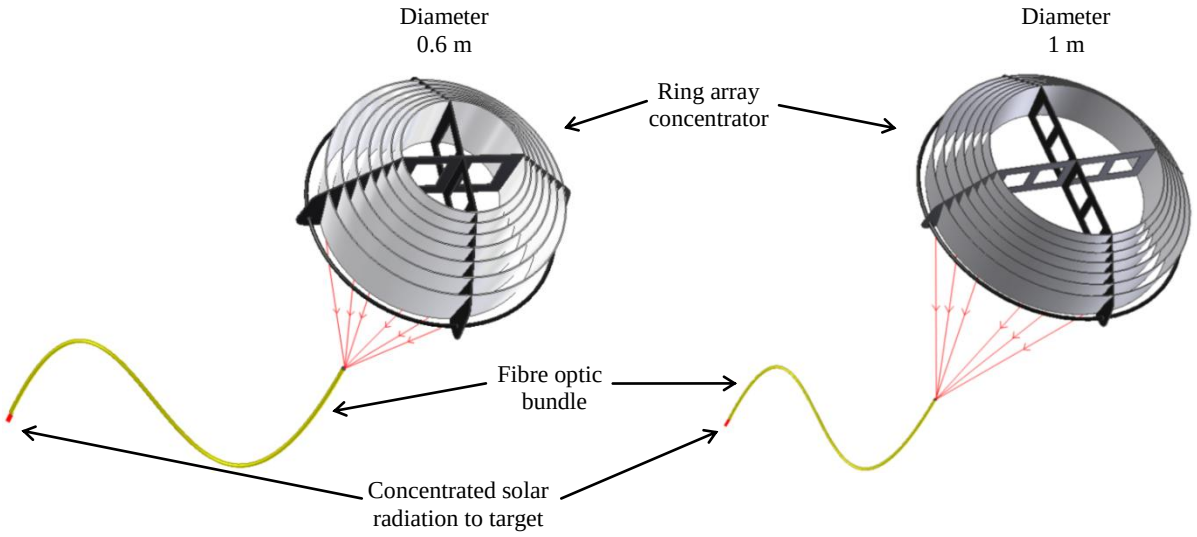

Figure 6.6 Two point focus concentrator systems used to compare misalignment sensitivity. Each concentrator consists of a nested set of reflective rings of 600 mm (left) and 1000 mm (right) diameter. There are seven reflective rings in both cases, but focal length differs.

To model the sensitivity of the two concentrators to tracking error, the light source used in the ray tracing software is misaligned through angles of 0.05˚, 0.10˚ and 0.15˚ relative to the longitudinal axis of each collector and rays are generated to assess the effect of the deviation (Figure 6.7). Results are then compared to the ideal case of no misalignment error (0˚).

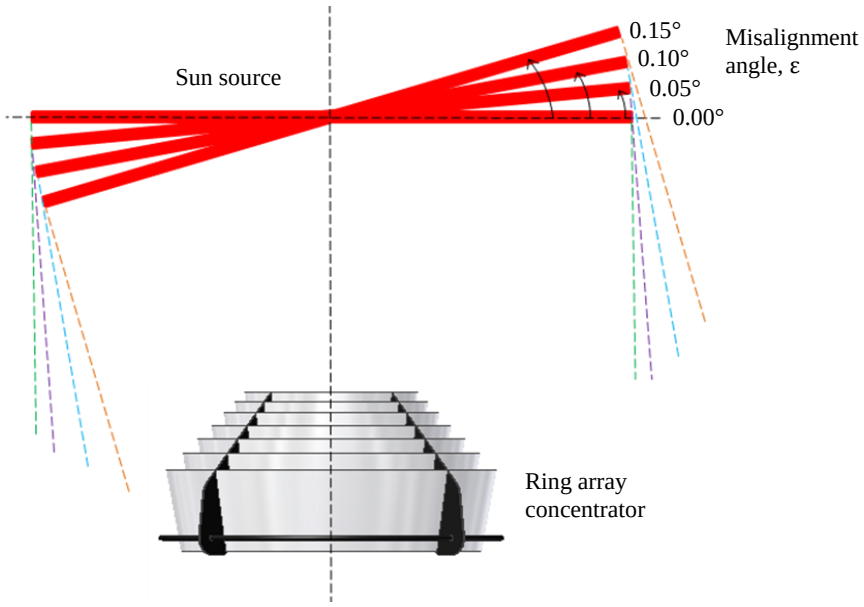

Figure 6.7 Exaggerated misalignment angles (ε) of 0.05˚, 0.10˚ and 0.15˚ at the sun source for the ring array concentrator configuration. Pointing error in an optical system is defined as the angular difference between the aperture center and the flux distribution center.

6.3.3 Ray tracing results

To compare ray tracing results, ideal and realistic conditions for the two RAC systems were modelled to reflect rays on to the 6 mm diameter inlet of the optical waveguide at a typical direct normal irradiance level of 850 W/m^2. Ideal parameters are defined by incident parallel light rays while the realistic simulation accounts for the non-parallel nature of the sun's rays (half-angle of 0.265˚). Simulating ideal and realistic properties is a generally accepted method to compare optical devices in the presence of diverging angles.

The ideal flux maps for the two systems are illustrated in Figure 6.8 showing average power values striking the fibre optic cable inlet. The unrealistic parallel rays were simulated to obtain improved representations of the RAC sensitivity to misalignment error. The parallel ray assumption gives rise to an expected violation of the second law of thermodynamics in predicting a concentration of 46 000 suns. As

an example, the top right flux map shows a peak level of $5.75*10^8$ W/m^2, which corresponds to a concentration of 676 471 suns, that is in violation of the maximum geometric concentration ratio. Both ring array systems show that as the misalignment angle (ε) increases the flux distribution on the optical waveguide inlet shifts off center, with the effect most pronounced for ε = 0.15˚, or three times the maximum error of the SPS tracker. The 1.0 m diameter system reaches the highest unrealistic flux levels due to the aperture area of the concentrator being larger than the 0.6 m diameter system. However as the misalignment angle increases the 1.0 m RAC system shows a wider spread and shifting of rays when compared to the smaller system. A possible reason for the higher spread in rays is the characteristic longer focal length related to larger diameter RAC systems. The realistic simulations for the 0.6 m diameter system show similar trends to that of the ideal case, with flux distributions shifting off center with an increase in misalignment angle (Figure 6.9). In comparison the 1.0 m array appears to show a uniform flux distribution, with no visible shifting from the center of the cable, except for the 0.15° misalignment error. This is due to larger initial spread of the concentrated beam and some spillage outside of the target, even for zero misalignment. The design procedure employed for both collectors assumes parallel incoming rays, hence the spillage of focused light when non-parallel rays are directed at the device.

In addition, for both systems the focused power on the fibre optic cable inlet decreases with increasing ε, as expected (Table 6.3). For the ideal simulation, the larger array's power values decrease more rapidly due to greater sensitivity to the range of misalignment angles. Decreases in percentage power values for the 0.6 m and 1.0 m diameter systems are 2.2% and 98.2% respectively. In comparison the realistic case shows a more rapid decrease in power for the 0.6 m diameter system. Percentages of the decrease in power values are 23.2% and 3.0% for the realistic and ideal simulations respectively. However the power values for each increment of ε are higher for the smaller system, indicating it is more sensitive to misalignment errors when the solar angle is modelled because the initial focus is better. This is due to the smaller concentrator having a focal length 500 mm shorter than the larger unit, thus less pointing errors occur and better performance values are obtained. Powers at inlet to the fibre optic cable are plotted in Figure 6.10 to illustrate the trend in performance loss as a function of ε for the two systems. The realistic simulation for the 0.6 m diameter system clearly produces superior performance. The larger array is relatively insensitive to tracking misalignment in the given ε-range, mainly because of a longer focal length such that the initial focusing and efficiency are poor compared to the smaller system. Key results from the analysis show that the realistic 0.6 m diameter model will perform at 99% its theoretical ray trace power value when integrating the accuracy of the SPS tracker into simulations. The misalignment error investigation comparing the two ring array systems supports the selection of the 0.6 m diameter ring array configuration for construction.

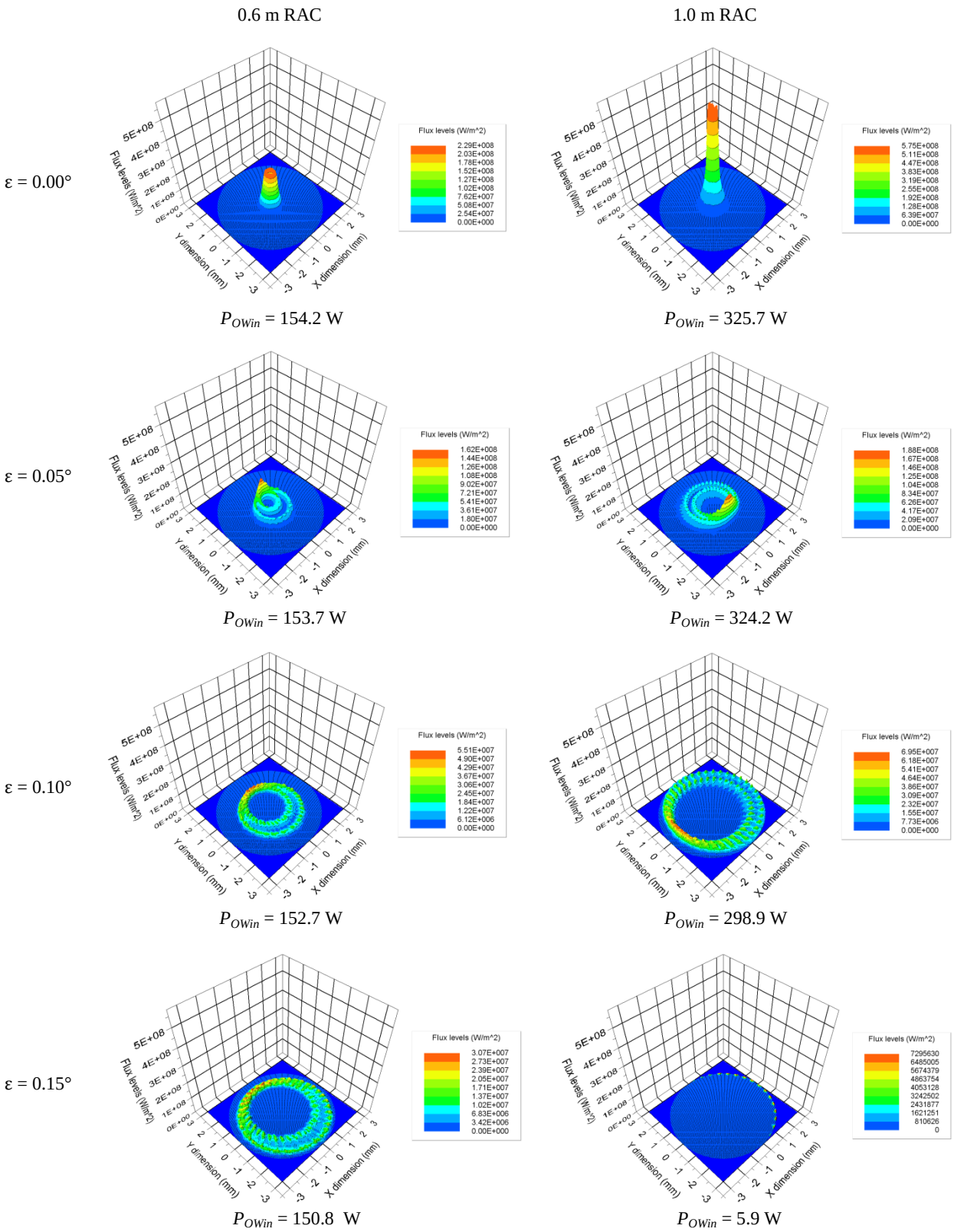

Figure 6.8 Ideal three-dimensional flux maps showing the irradiance levels and positioning of the reflected parallel rays of light at the inlet to the waveguide. Average power values are given beneath respective flux maps. The 0.6 m and 1.0 m diameter optical systems with corresponding misalignment angles are on the left and right respectively.

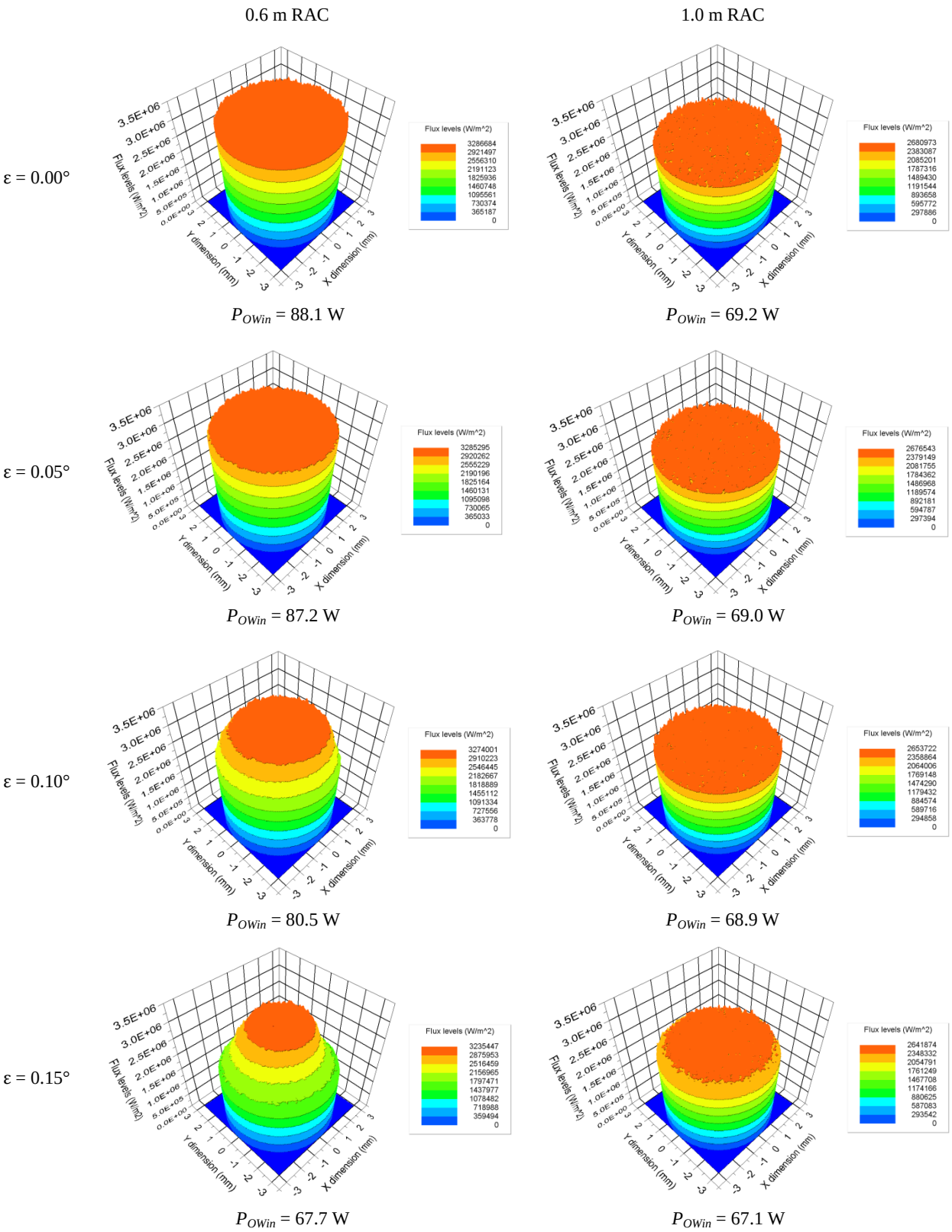

Figure 6.9 Three-dimensional irradiance maps showing a realistic simulation of rays striking the 6 mm diameter optical waveguide inlet. Average power values are given beneath respective flux maps. The 0.6 m and 1.0 m diameter optical systems with corresponding misalignment angles are on the left and right respectively.

Table 6.3 Average power values at optical waveguide inlet, P_{OWin}, for the range of misalignment errors obtained by ray tracing methods for two ring array concentrator systems.

		Average power at fibre optic cable inlet, P_{OWin} (W)			
		Ideal		Real	
		0.6 m	1.0 m	0.6 m	1.0 m
Misalignment angle, ε	0.00°	154.2	325.7	88.1	69.2
	0.05°	153.7	324.2	87.2	69.0
	0.10°	152.7	298.9	80.5	68.9
	0.15°	150.8	5.9	67.7	67.1

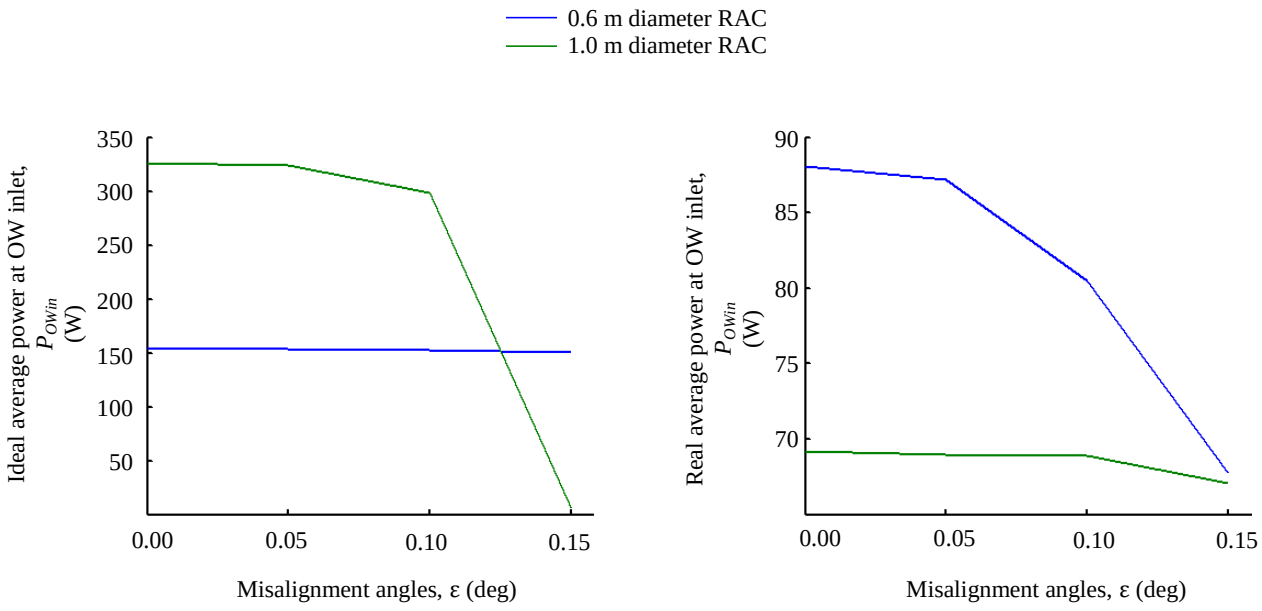

Figure 6.10 Ideal and realistic power plots at optical waveguide inlet showing misalignment sensitivity for the two systems (0.6 m and 1 m diameter systems).

6.4 Summary

Factors contributing to the reduction in performance of FOCUS including the solar half-angle, optical errors and pointing errors have been individually modelled and characterised. Further analysis incorporating realistic material properties of the elements with surface slope errors for the reflective elements and misalignment errors due to imprecise tracking is conducted through a set of ray tracing simulations for the 300 mm radius ring array concentrator. The theoretical model allows predictions of the power density at the inlet and outlet of the fibre optic cable.

7. NUMERICAL RESULTS

7.1 Introduction

A numerical analysis was conducted to predict performance results of the Fibre Optic Concentrating Utilisation System through a set of ray tracing simulations. The results from the ray trace provide power values at different stages in the system for characterising the optical efficiency.

Optical efficiency, as defined in solar concentrating applications, is the ratio of solar energy striking the receiver to the incident energy falling on the reflective collector surface (Kribus et al., 1999). Overall optical efficiency of FOCUS (Equation 7.1) is characterised as the product of the efficiencies applicable to the concentrator (η_{RAC}), the focusing process (η_{foc}), injection into the optical waveguide (η_{inj}) and transmission to the target (η_{τ}) (Figure 7.1). Power values used to obtain the first three efficiency stages include the powers at concentrator inlet (P_{in}), concentrator exit (P_{out}), inlet to optical waveguide (P_{OWin}) and the actual power injected into the silica fibres (P_{act}). Predictions of each power value were conducted using ray tracing simulations.

$$\eta_{overall} = \eta_{RAC} \cdot \eta_{foc} \cdot \eta_{inj} \cdot \eta_{\tau} \tag{7.1}$$

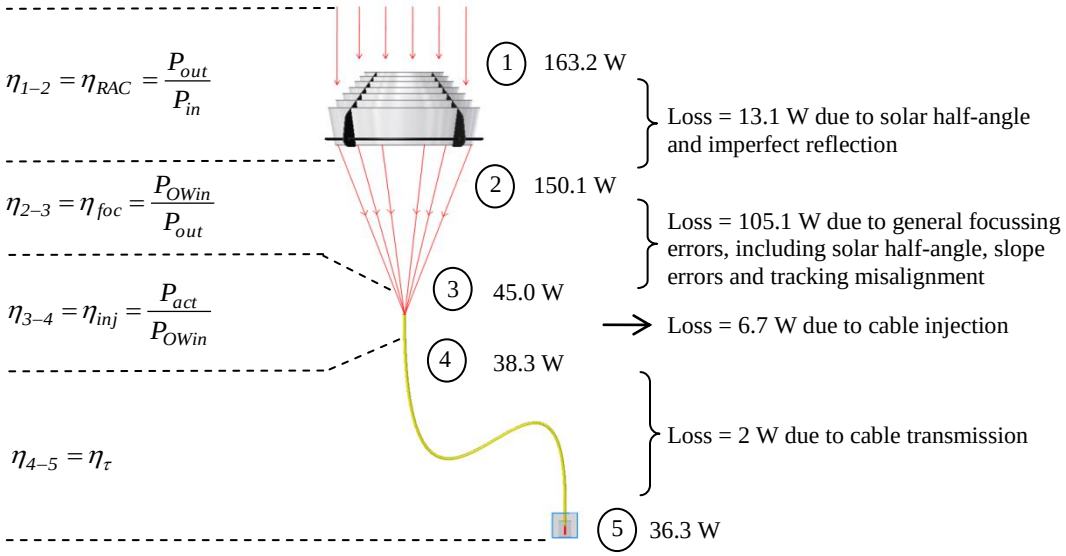

Figure 7.1 Predicted optical efficiency stages for FOCUS. The four efficiency stages include the concentrator, focusing process, injection into the optical waveguide and the transmission of the concentrated sunlight to the target. The power values given are based on a nominal input flux of 850 W/m^2 acting on an aperture of 0.192 m^2.

7.2 Ray tracing model

A ray tracing model was developed to characterise the optical efficiency of the 300 mm radius RAC by estimating the amount of energy striking a receiver of 60 mm diameter. The receiver represents a copper plate used to capture the energy reflected from the 600 mm diameter RAC for an experimental energy balance analysis (discussed in Chapter 8). The aim of the ray tracing model is to estimate the optical efficiencies of the RAC concentrating energy on to: 1) a 60 mm diameter copper plate and 2) a 6 mm diameter receiver representing the inlet to the fibre optic cable.

Ray tracing simulations were conducted for the model to compare progressive efficiencies for eight cases incorporating ideal and realistic parameters. Table 7.1 shows the input parameters for each case. Starting from Case 1, simulations were carried out incorporating ideal parameters progressing to a worst case scenario of errors in Case 8. Ideal parameters include parallel rays of sunlight incident on the ideal paraboloidal concentrator, perfect specular reflection from the reflective elements and no tracking misalignment. Realistic parameters incorporate the solar half-angle of 0.265°, 95% specular reflection for Miro 4 aluminium, an average tracking error of 0.05° and a best and worst case scenario of the surface slope errors for the manufactured elements. The eight cases were simulated for a typical direct normal irradiance of 850 W/m^2 to obtain comparative power density results.

Table 7.1 Ray tracing input parameters. Eight numerical simulations of FOCUS were conducted incorporating ideal and realistic parameters for comparison.

	Ideal →							**Real**
Input parameters	**Case 1**	**Case 2**	**Case 3**	**Case 4**	**Case 5**	**Case 6**	**Case 7**	**Case 8**
Ideal parallel rays (0.00°)	1	0	0	0	0	0	0	0
Ideal specular reflection (100%)	1	1	0	0	0	0	0	0
Ideal RAC geometry	1	1	1	1	0	0	0	0
Ideal tracking error (0.00°)	1	1	1	0	1	0	1	0
Solar half-angle (0.265°)	0	1	1	1	1	1	1	1
Realistic specular reflection (95%)	0	0	1	1	1	1	1	1
Average tracking error (0.05°)	0	0	0	1	0	1	0	1
Manufactured geometry (Best case)	0	0	0	0	1	1	0	0
Manufactured geometry (Worst case)	0	0	0	0	0	0	1	1

7.3 Ray tracing results

To estimate overall optical efficiency, power values for the first three efficiency stages were computed. Key power results at the receiver are illustrated in two sets of three dimensional flux maps. Figures 7.2 and 7.3 show the average power levels striking the 60 mm diameter copper plate, P_{Cu} and 6 mm diameter inlet to the optical waveguide, P_{OWin} respectively. In both Figures, Cases 1 – 8 progressively illustrate expected power losses at the receiver.

Figure 7.2 shows a power of 163.2 W striking the copper receiver for Case 1 which indicates a no loss model due to the unrealistic parameters simulated. Cases 2 – 8 illustrate losses in power due to the use of realistic parameters given in Table 7.1. A comparison between Cases 2 and 4 show that integrating the solar angle, realistic surface properties for elements and the tracking error decreases power levels by 6%. More realistic models are simulated in Cases 5 – 8 where the majority of losses are expected due to integration of slope errors. Power losses between Cases 2 and 5 amount to 10% when the best case scenario of slope errors and no misalignment errors are simulated. Case 8 represents the worst case scenario for all modelled components in the system and shows a power decrease of 14% when compared to Case 2.

The importance of the ray tracing simulations is estimating the power striking the fibre optic cable inlet, P_{OWin}. Figure 7.3 represents magnified views of Figure 7.2 showing only the average power striking the 6 mm diameter cable inlet. Similarly with the 60 mm diameter copper plate, the no loss model of Case 1 shows a power of 163.2 W striking the cable inlet. Power levels between Cases 2 and 4 decrease by 6% showing a similar trend to that of the 60 mm diameter receiver. A comparison between Cases 4 and 6, and Cases 4 and 8 shows representations of slope error effects on the manufactured composite material RAC. For the best and worst case scenarios of the slope errors a decrease in power of 45% and 48% is observed respectively. In addition Case 8 performs at 49% its maximum attainable performance (Case 2) when realistic material properties, misalignment error and surface slope inaccuracies are implemented.

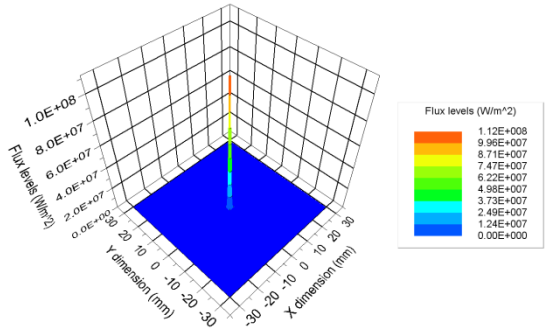

Case 1 – P_{Cu} = 163.2 W

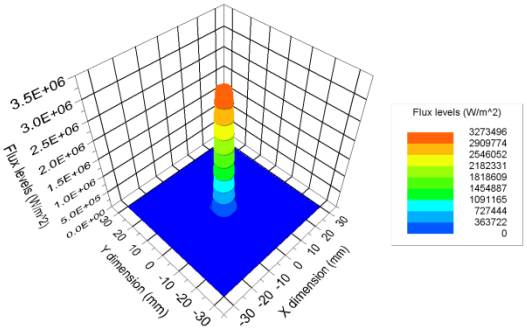

Case 2 – P_{Cu} = 159.2 W

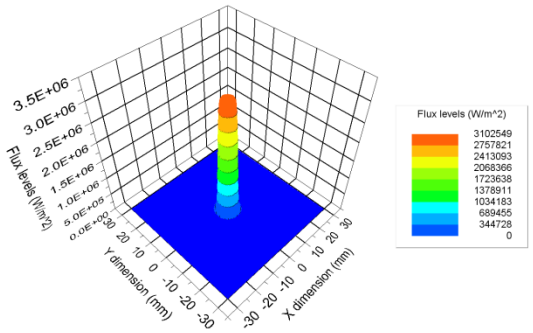

Case 3 – P_{Cu} = 150.5 W

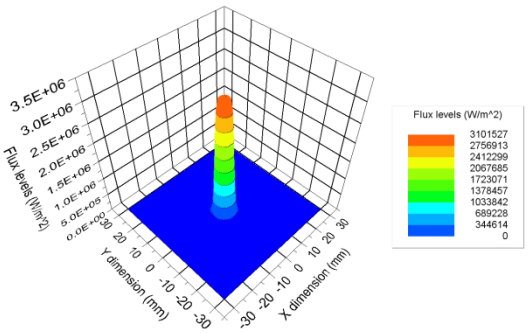

Case 4 – P_{Cu} = 149.3 W

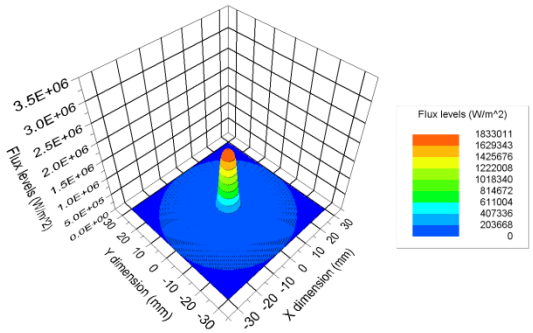

Case 5 – P_{Cu} = 142.8 W

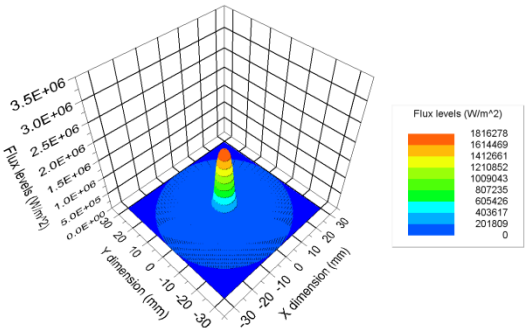

Case 6 – P_{Cu} = 142.7 W

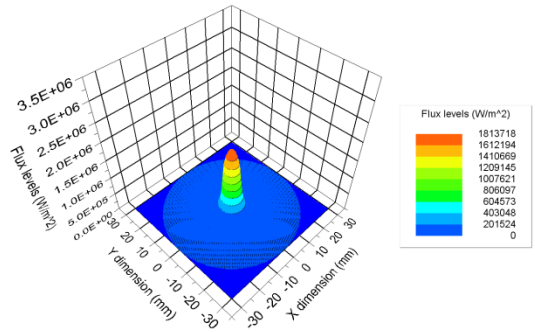

Case 7 – P_{Cu} = 137.8 W

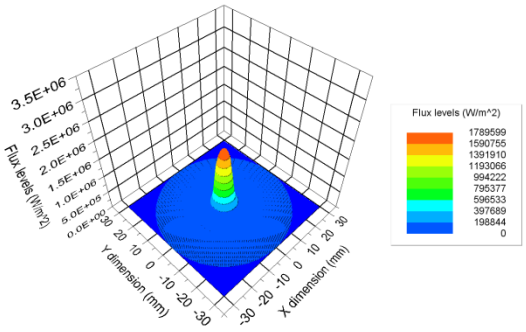

Case 8 – P_{Cu} = 137.7 W

Figure 7.2 Three-dimensional irradiance maps illustrating flux levels striking the 60 mm diameter copper plate for simulation Cases 1 – 8. Flux levels decrease progressively due to realistic parameters modelled for each simulation.

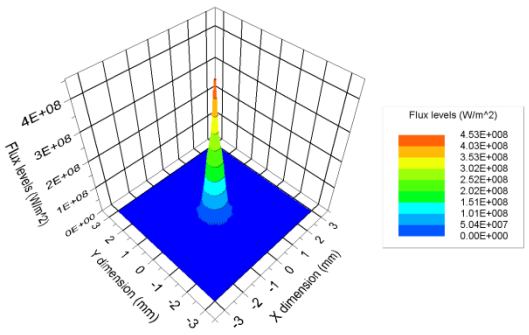

Case 1 - P_{OWin} = 163.2 W

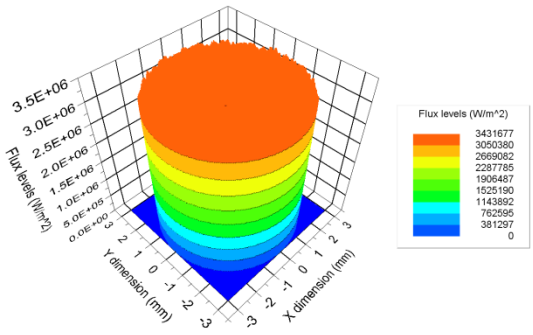

Case 2 - P_{OWin} = 91.9 W

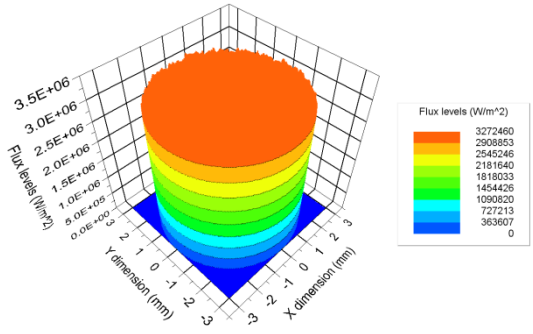

Case 3 - P_{OWin} = 86.8 W

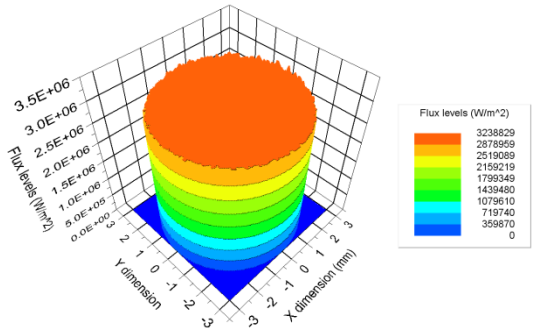

Case 4 - P_{OWin} = 86.2 W

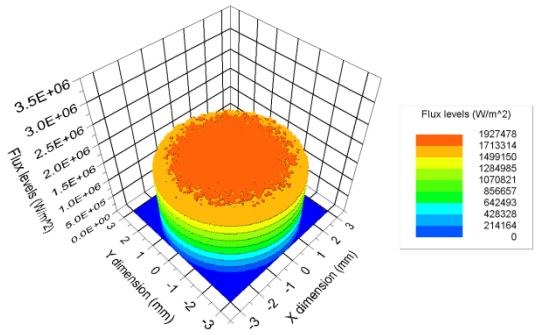

Case 5 - P_{OWin} = 48.0 W

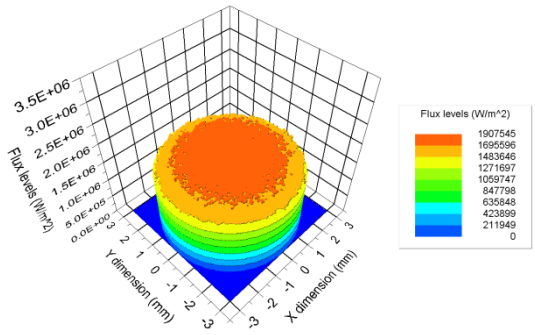

Case 6 - P_{OWin} = 47.5 W

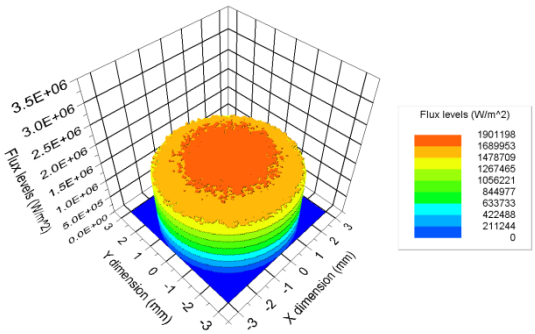

Case 7 - P_{OWin} = 46.5 W

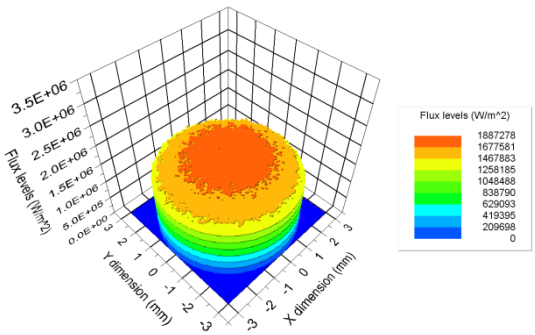

Case 8 - P_{OWin} = 44.8 W

Figure 7.3 Three-dimensional flux maps representing power density levels at waveguide inlet for simulation Cases 1 – 8. Average power levels at waveguide inlet, P_{OWin} decrease progressively due to realistic parameters implemented for each case simulation.

In addition to the three-dimensional flux maps representative cross-sectional flux profiles for the 60mm diameter receiver and 6 mm diameter cable inlet are shown in Figures 7.4 and 7.5 respectively. The two-dimensional profiles illustrate progressive power losses starting from Case 2 through to 8 due to realistic parameters modelled. The primary aim of the numerical analysis is to obtain expected flux profiles striking the 60 mm diameter copper receiver and 6 mm diameter fibre optic cable inlet using a worst case scenario simulation. Figure 7.6 illustrates the worst case flux profiles and will be used when validating the experimental results against the numerical model.

The performance of a concentrator can also be shown using a flux concentration ratio. Equation 7.2 defines the average flux concentration of the concentrator, C_{flux} where F_{A_r} is the average flux striking the receiver and F_{A_a} is the average flux on the collector aperture area. Using the ray trace results of Case 8, average concentrations of 58 suns and 1864 suns are estimated for the 60 mm diameter copper plate and 6 mm diameter cable inlet respectively.

$$C_{flux} = \frac{F_{A_r}}{F_{A_a}} \tag{7.2}$$

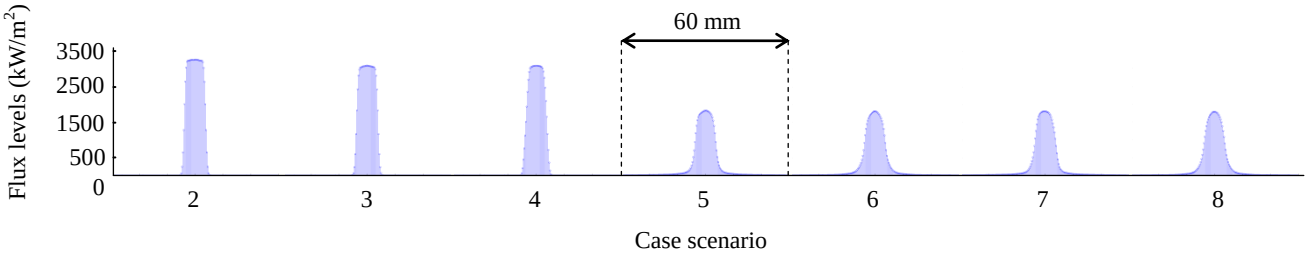

Figure 7.4 Two-dimensional flux maps showing representative cross-sectional profiles of the 60 mm diameter receiver for Cases 2 - 8. Progressive losses in performance occur due to realistic ray trace modelling.

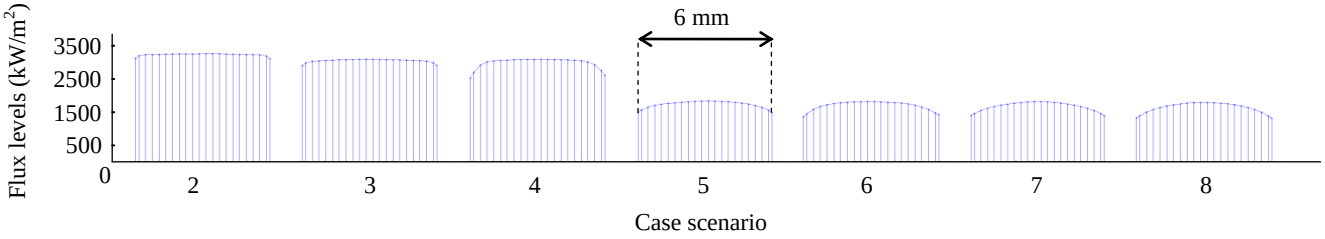

Figure 7.5 Two-dimensional flux maps showing magnified cross-sectional flux profiles of the 6 mm diameter optical waveguide inlet for Cases 2 - 8. Progressive losses in performance occur due to realistic ray trace modelling.

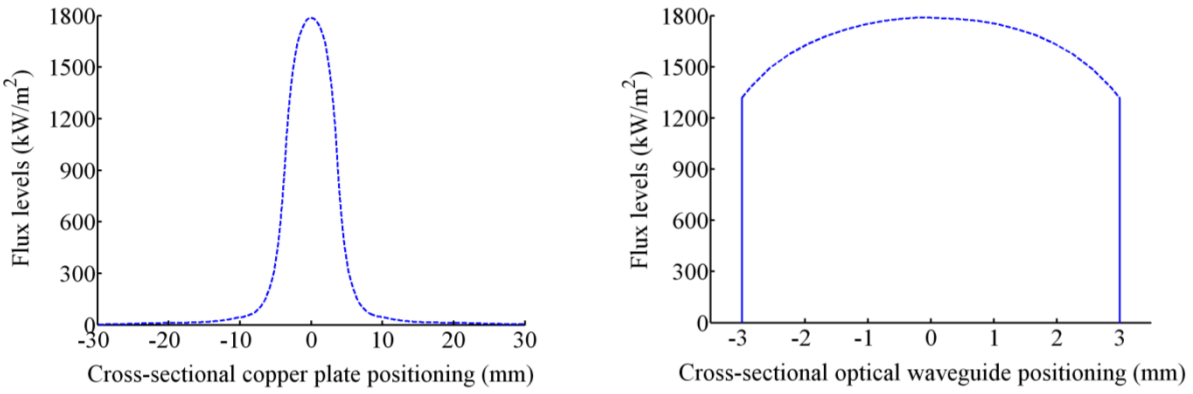

Figure 7.6 Representative cross-sectional flux maps showing the worst case ray trace scenario of Case 8 for the 60 mm diameter copper receiver (left) and the fibre optic cable inlet (right). The two theoretical ray trace profiles will be compared to the experimental results.

The numerical analysis incorporating optical errors in the system is comprehensive but not exhaustive, and additional inefficiencies are certain to manifest due, for example, to overall structural distortion of the integrated collector as it tracks the sun, reflective losses at the inlet to the fibre optic cable, soiling of the mirror surfaces and degradation of the aluminium over time due to atmospheric exposure.

Improvements to the concentrating system should focus on optimising efficiencies between each Case simulation. Boosting the specular reflectance of the mirror material is necessary to increase efficiency between Cases 2 and 3, and may be possible using silver deposition methods. Power levels between Cases 3 and 4 can be increased by improving the sensitivity of the sun sensor to allow for a tracking accuracy of 0.04°. Improving surface slope accuracies of the reflective elements will increase efficiencies between Cases 4 through 8 significantly. The results from each ray trace scenario allow for calculating the theoretical optical efficiency of: 1) the RAC concentrating energy on to a 60 mm diameter copper plate, and 2) FOCUS.

7.4 Optical efficiency

The estimated efficiency stages, average power, P_{Cu}, flux levels, F_{Cu} and flux concentration, $C_{flux,Cu}$ for characterising the performance of the ring array concentrator are given in Table 7.2. The results from each case scenario show performance of the RAC focussing sunlight onto a 60 mm diameter receiver. An overall efficiency of 84% for Case 8 indicates the copper receiver does not capture all the reflected rays from the RAC. To potentially increase the efficiency a larger copper plate should be modelled, however this research uses a smaller plate to minimise the expected heat losses associated to larger surfaces.

Table 7.2 Predicted component efficiencies and performance results for characterising the ring array concentrator with a 60 mm diameter receiver using ray tracing methods. Simulations were conducted at a typical irradiance of 850 W/m^2.

		Case simulation							
		1	**2**	**3**	**4**	**5**	**6**	**7**	**8**
Stages	η_{RAC}	1.00	0.98	0.93	0.93	0.93	0.93	0.92	0.92
	η_{foc}	1.00	1.00	0.99	0.98	0.95	0.94	0.91	0.91
Total	$\eta_{overall}$	1.00	0.98	0.92	0.91	0.88	0.87	0.84	0.84
Power striking copper plate, P_{Cu} (W)		163.2	159.2	150.5	149.3	142.8	142.7	137.8	137.7
Flux striking copper plate, F_{Cu} (W/cm^2)		5.8	5.6	5.3	5.3	5.1	5.0	4.9	4.9
Flux concentration, copper plate, $C_{flux,\,Cu}$ (suns)		68.2	65.9	62.4	62.4	60.0	58.8	57.6	57.6

The above efficiency values do not account for integration of the RAC with the fibre optic cable, therefore further processing of the ray trace results is needed to estimate the energy injected into and transmitted through the cable. Using Case 8 as an example, an average power of 44.8 W strikes the inlet to the optical waveguide (Figure 7.3). This value corresponds to an average flux at optical waveguide inlet, F_{OWin} of 158.4 W/cm^2 and does not represent absorbed power because the waveguide inlet is composed of a bundle of 900 fibres (Figure 7.7 left). The approximate active area of waveguide inlet, AA_{OWin} and outlet, AA_{OWout} is calculated by summing the surface areas of the hexagonally distorted fibre ends, with representative dimensions obtained from a micrograph (Figure 7.7 right). Using a hexagonal width, W, of 176 µm, active area is calculated using Equation 7.3. The actual power (P_{act}) that strikes the fibres is then obtained from Equation 7.4, which scales the ray trace value (P_{OWin}) by the ratio of active to total area, TA_{OWin}.

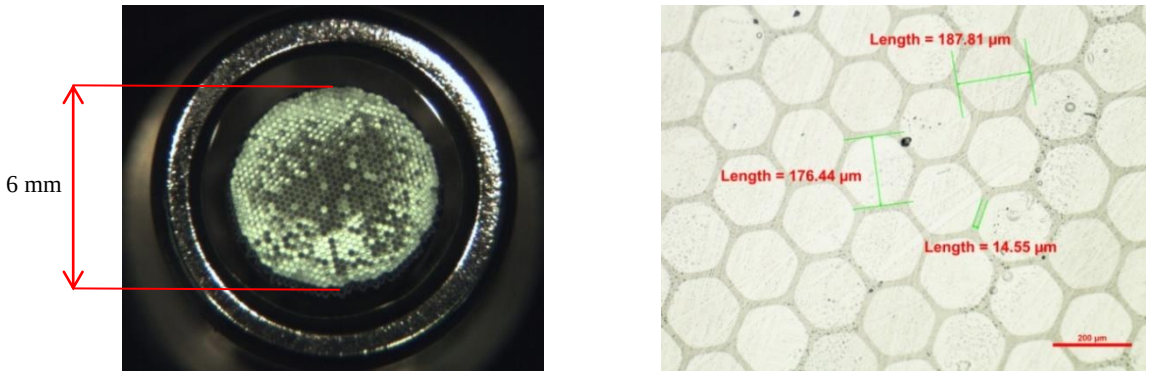

Figure 7.7. Photomicrographs of the optical waveguide fused inlet end (left) and a 100 times magnified view showing the hexagonal geometry of the silica fibres (right).

$$AA_{OWin} = AA_{OWout} = \frac{\sqrt{3}}{2} W^2 * N_f \quad (7.3)$$

$$P_{act} = \frac{P_{OWin}}{TA_{OWin}} AA_{OWin} \quad (7.4)$$

The waveguide used here has a fused outlet, similar to the inlet shown in Figure 7.7. The outlet cable flux (F_{OWout}) is calculated using the estimated power exiting the cable, P_{OWout} and the active area (Equation 7.5). Final performance results for the Fibre Optic Concentrating Utilisation System are given in Table 7.3. The values assume fibre optic transmission efficiency (η_τ) of 95%. For the realistic simulation of Case 8 a flux of 150.5 W/cm^2 is estimated which exceeds the nominal design value of 85 W/cm^2 by 77%. For the realistic best and worst case scenarios of Cases 5 and 8, FOCUS has overall optical efficiencies of 24% and 22% respectively. To validate the theoretical ray tracing simulations of Case 8, a flat plate calorimeter was constructed to be used in an experimental heat transfer analysis for high-flux solar measurements.

$$F_{OWout} = \frac{P_{OWout}}{AA_{OWout}} \quad (7.5)$$

Table 7.3 Predicted component efficiencies and average performance results for FOCUS using ray tracing methods. Simulations were conducted at a typical irradiance of 850 W/m^2.

		Case simulation							
		1	**2**	**3**	**4**	**5**	**6**	**7**	**8**
Stages	η_{RAC}	1.00	0.98	0.93	0.93	0.93	0.93	0.92	0.92
	η_{foc}	1.00	0.58	0.58	0.57	0.32	0.31	0.31	0.30
	η_{inj}	0.85	0.85	0.85	0.85	0.85	0.85	0.85	0.85
	η_τ	0.95	0.95	0.95	0.95	0.95	0.95	0.95	0.95
Total	$\eta_{overall}$	0.81	0.46	0.44	0.43	0.24	0.23	0.23	0.22
Power at cable inlet, P_{OWin} (W)		163.2	91.9	86.8	86.2	48.0	47.5	46.5	44.8
Fibre optic inlet flux, F_{OWin} (W/cm^2)		577.2	325.0	307.0	304.9	169.8	168.0	164.5	158.4
Flux concentration, cable inlet, $C_{flux,\ OWin}$ (suns)		6790.6	3823.9	3611.7	3586.7	1997.2	1976.4	1934.8	1864.1
Power at cable outlet, P_{OWout} (W)		132.4	74.5	70.4	69.9	38.9	38.5	37.7	36.3
Fibre optic outlet flux, F_{OWout} (W/cm^2)		548.3	308.8	291.6	289.6	161.3	159.6	156.2	150.5
Flux concentration, cable outlet, $C_{flux,\ OWout}$ (suns)		6451.1	3632.7	3431.1	3407.4	1897.4	1877.6	1838.1	1770.9

8. ENERGY BALANCE VALIDATION METHOD

8.1 Introduction

The measurement of energy flux is required to characterise the performance of a point-focus solar concentrating system. Several devices have been developed for high-flux solar measurements, including calorimetric and radiometric techniques (Ballestrín et al., 2006 and Ballestrín, 2002). Calorimeters use energy balance methods to obtain estimated flux concentrations incident on the receiving surface. The methodology includes determining the heat absorbed by a heat transfer fluid flowing through the calorimeter body, by measuring the change in temperatures at inlet and outlet (Estrada et al., 2007). Considerations for this technique include minimising uncertain measurements pertaining to mass flow rate of the fluid and rise in temperature at calorimeter exit. Estimated modeling of heat losses due to convection and radiation is needed when the receiver plate does not approximate ambient temperature. Other more expensive instruments used for measuring heat flux are CPV cells (Fernández-Reche et al., 2008) and radiometers, such as the Gardon gage (Ballestrín et al., 2003). Operating principles of the Gardon gage include measuring the radial temperature difference of a circular foil disk using a differential thermocouple (Ballestrín and Monterreal, 2004). The disk is machined from constantan and attached to a cylindrical copper heat sink. Material properties of the assembly produce a 10mV maximum output that is directly proportional to the absorbed heat flux. The advantage of using the Gardon gage for high-flux solar measurements is its short time response of less than one second which makes it an attractive device for experimental procedures (Ballestrín et al., 2006). In comparison the inexpensive approach of using calorimeters requires processing of the experimental results before obtaining flux measurements. A combination of calorimetric and radiometric methods can also be employed to measure concentrated solar radiation (Pérez-Rábago et al., 2006). The device operates as a normal radiometer and a calorimetric component is added to calibrate the apparatus.

For this research a low-cost approach was adopted to determine the high-flux solar measurements of FOCUS. A flat plate calorimeter was constructed to validate ray tracing results with cost savings estimated at one tenth the price of existing commercial radiometers. Energy balance methods include using the simplified steady-flow thermal energy equation to estimate the heat absorbed by the circulating fluid, water, with convection and radiation losses described. Experimental results are compared to theoretical ray trace simulations during the performance testing programme. The experimental aim is to

quantify the power densities at inlet and exit of the fibre optic cable by energy balance methods. The calorimeter design is based on work done by Jaramillo et al. (2008).

8.2 Calorimeter construction

The calorimeter with its sub-components is shown in Figure 8.1. The cylindrical outer casing is machined from stainless steel that houses a nylon insulator, radial flow distributor and a copper receiver. The insulation material is Ertalon 66SA Polyamide which has a low thermal conductivity of 0.25 W/(m.K) to minimise heat transfer between the calorimeter body and water flow. The radial flow distributor threads into the cylindrical water passage and allows water to diffuse evenly on to the copper disc. The 60 mm diameter copper plate of 6 mm thickness fastens on to the insulation and concentrically covers the distributor with a gap that allows water flow. Construction efforts included roughening the inside surfaces of the calorimeter with the intention of inducing turbulent flow. The copper surface exposed to the concentrated energy is painted with NS7, a black matt paint which creates a rough surface to increase energy absorption. NS7 paint was assumed to have similar properties to the well characterised coating of Zynolyte paint due to their use in similar applications. The properties of Zynolyte paint which makes it attractive for solar energy applications are its absorptivity and emissivity values of 0.95 each (Ballestrín et al., 2004).

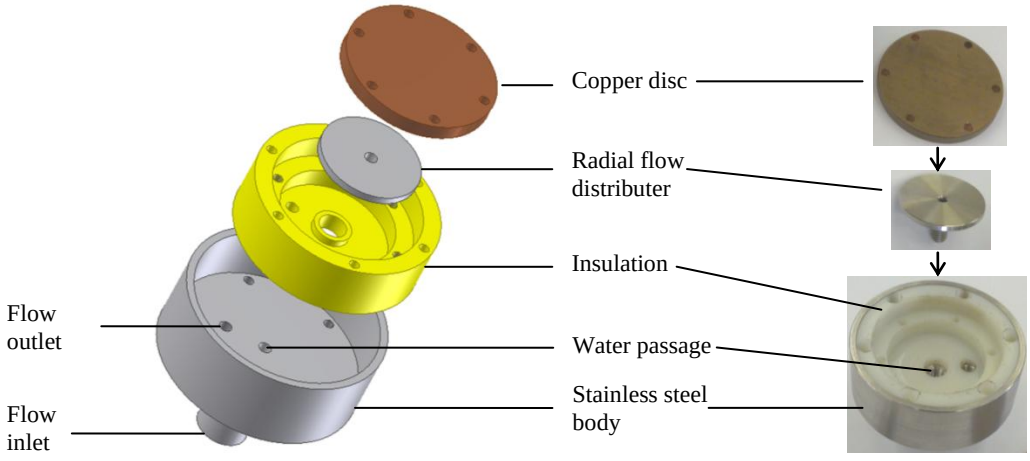

Figure 8.1 Exploded view of the flat plate calorimeter constructed for performance measurements of FOCUS. The device consists of a cylindrical stainless steel outer casing that houses a nylon insulator, a radial flow distributor and the copper receiving plate (left). Pre-assembly of the calorimeter is shown on the right.

The operational procedure involves concentrated rays striking the copper disc while cold water flows through the device to absorb energy. Cold water enters via the inlet and flows up the water passage arriving at the copper receiver where heat transfer takes place. The water contacts the inner surface of the copper thereby removing heat before flowing radially between the plate and distributor to exit the device. An energy balance is carried out on the copper disc to determine the concentrated flux arriving at the plate surface.

8.3 Energy balance

The conservation of energy derived from the first law of thermodynamics is required to carry out energy balance calculations (Incropera et al., 2007). The methodology includes defining a control volume, identifying relevant heat transfer processes and establishing the rate equations. The general form of conservation of energy states that on a rate basis, the stored energy, $\dot{E}_{st}$, equals the energy inflow, $\dot{E}_{in}$ plus the thermal energy generated, $\dot{E}_{g}$, minus the energy outflow, $\dot{E}_{out}$ (Equation 8.1). Under assumed steady state conditions there is no change in energy storage, and due to zero thermal energy generated, Equation 1 is simplified to zero change in energy inflow and outflow (Equation 8.2).

$$\dot{E}_{in} + \dot{E}_{g} - \dot{E}_{out} = \dot{E}_{st} \tag{8.1}$$

$$\dot{E}_{in} - \dot{E}_{out} = 0 \tag{8.2}$$

Figure 8.2, left illustrates the control volume around the copper receiver as the boundary where energy inflow and outflow occurs. The aim of the energy balance is to estimate the solar power incident on the plate, q_{in}, by summing the energy absorbed by the water flow, q_{abs} and the external heat losses, $q_{l,out}$ (Equation 8.3). By using the absorptivity of the plate surface, α_s the fraction of incident irradiation that is absorbed may be estimated. Internal losses are neglected due to the low thermal conductivity of the nylon insulation within the calorimeter body.

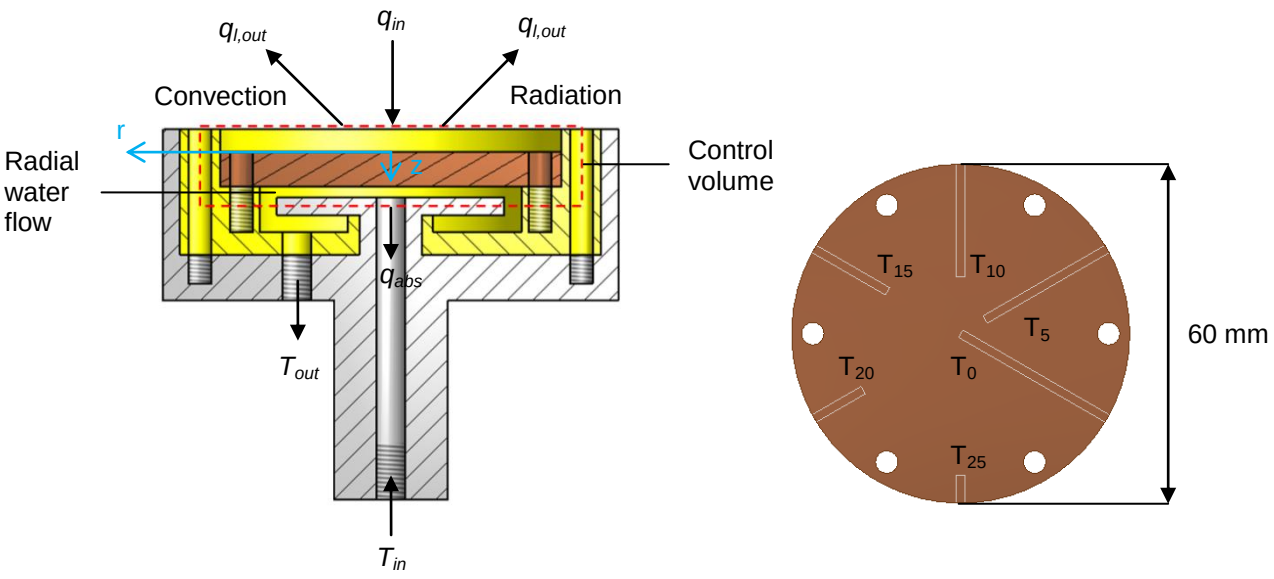

Figure 8.2 (left) Calorimeter cross-section illustrating the conservation of energy for a steady-flow, open system. (right) Top view of the six thermocouple positions inside the copper plate, starting with T_0 at r = 0 mm, increasing anti-clockwise in increments of 5 mm, ending with T_{25} at r = 25 mm.

$$\alpha_s q_{in} = q_{abs} + q_{l,out} \tag{8.3}$$

Energy absorbed by the water flow is estimated by the simplified steady-flow thermal energy equation (Equation 8.4), where $\dot{m}$ is the mass flow rate, $C_{p,w}$ is the specific heat of water and T_{out} and T_{in} are the water outlet and inlet temperatures respectively. External heat losses to the surroundings arise from convection, q_{conv} and radiation, q_{rad} at the copper plate surface (Equation 8.5), where A_{Cu} is the area of the copper plate, h is the convective heat transfer co-efficient at the surface, ε_s is the emissivity of the plate, σ is the Stefan-Boltzmann constant and T_s and T_{amb} are the mean value of surface temperature and ambient temperature, respectively. To approximate a mean temperature value at a depth of z = 3 mm, six thermocouples, equidistant apart are radially positioned (Figure 8.2, right). The thermocouples will measure radial temperature distribution midway in the plate. To obtain a mean temperature at the plate surface, T_s a conduction analysis in the z-direction is modelled to approximate the additional temperature from z = 3 mm to the plate surface (z = 0 mm). Using ray tracing results the temperature change, ΔT between the top (z = 0 mm) and bottom (z = 6 mm) surfaces of the plate can be estimated with Equation 8.6, where $\alpha_s \dot{q}''_{theo,in}$ is the heat flux in the z-direction, k_t is the thermal conductivity of copper and t is the plate thickness. Scaling down the temperature difference by a factor of two, estimates the temperature in the z-direction from z = 3 mm to the plate surface (z = 0 mm), where concentrated solar rays strike.

$$q_{abs} = \dot{m} C_{p,w} (T_{out} - T_{in}) \tag{8.4}$$

$$q_{l,out} = q_{conv} + q_{rad} \tag{8.5}$$

$$= A_{Cu} [h(T_s - T_{amb}) + \varepsilon_s \sigma ({T_s}^4 - {T_{amb}}^4)]$$

$$\alpha_s \dot{q}''_{theo,in} = k_t \frac{\Delta T}{t} \tag{8.6}$$

The energy balance methodology is implemented in MATLAB to obtain a heat transfer analysis code (HTAC) for point focus solar concentrators using a flat plate calorimeter (Appendix C). The completed calorimeter is shown in Figure 8.3.

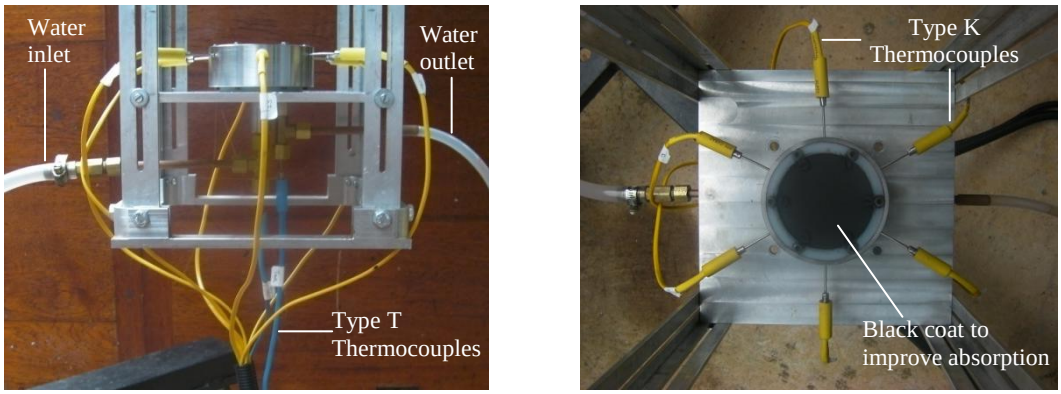

Figure 8.3 (left) Calorimeter side view showing water inlet and outlet passages. (right) Top view of the six thermocouple positions inside the painted copper plate to estimate convective and radiative heat losses.

9. EXPERIMENTAL RESULTS

9.1 Introduction

The experimental testing programme aims to characterise the performance of the Fibre Optic Concentrating Utilisation System using a flat plate calorimeter. Experimental testing was conducted for three phases with primary aims to determine: 1) the power entering and 2) exiting the fibre optic cable and 3) the melting capabilities of lunar regolith using FOCUS. Results are compared to the 85 W/cm^2 flux criterion reported by Nakamura and Smith (2009) to validate the optical system's ability to melt lunar regolith for high-flux applications.

9.2 Experimental setup

Key components of the experiment include FOCUS, the calorimeter, water circulation system and instrumentation (Figure 9.1). The experimental procedures to determine the high-flux solar measurements of FOCUS include positioning the calorimeter firstly at the focal point of the concentrator, and secondly at fibre optic cable exit (Figure 9.2). Calorimeter positioning at concentrator focus allows determining performance results entering the optical waveguide such as, power, (P_{OWin}) flux (F_{OWin}) and flux concentration ratio ($C_{flux,OWin}$). Similarly performance results at fibre optic outlet of P_{OWout}, F_{OWout} and $C_{flux,OWout}$ are characterised.

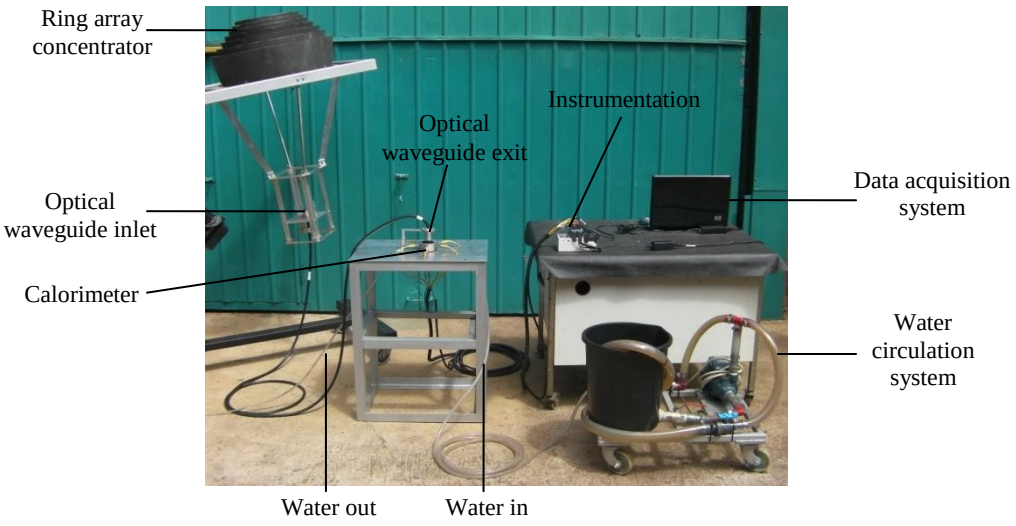

Figure 9.1 Experimental layout for the second test phase to characterise the flux at fibre optic cable exit. Fundamental components include FOCUS, the flat plate calorimeter, water pumping system and thermocouples.

Figure 9.2 (left) Calorimeter positioned at concentrator focal point to characterise the performance of the composite material RAC and (right) fibre optic cable directed onto the calorimeter to determine exit flux concentration.

9.3 Experimental procedure

Testing was conducted at the University of KwaZulu-Natal under clear sky conditions. The test area was sheltered to ensure favourable wind conditions while allowing clear vertical views for sun-concentrator orientation. Direct normal irradiance levels were measured with a nearby Eppley normal incidence pyrheliometer located at the Howard College radiometric ground station (29.9°S, 30.98°E, 151.1 m elevation). A typical experiment includes cleaning the seven reflective elements and positioning them such that the focal spot approximates concentric alignment onto the receiver, being either the copper plate or the fibre optic cable inlet. The receiver is firstly positioned using the calculated focal point and is vertically fine-tuned for a visibly minimised focal spot diameter. Positioning the ring elements and receiver was performed with the dual-axis solar tracker in operation. Running time per experiment is three minutes, which assumes negligible differences in direct normal irradiation and steady state water flow. The fluid circulation system consists of a pump fitted with a throttle valve to achieve the desired mass flow rate (Figure 9.3). Mass flow rate is measured by conducting a timed volume collection and is set to keep the copper receiving plate at a temperature close to ambient to minimise external heat losses due to convection and radiation. Instrumentation includes two type T thermocouples for the inlet and outlet water measurements and six type K thermocouples for the temperature distribution measurements midway in the copper plate. Data acquisition software was developed in LabVIEW to log measurement results for further processing in HTAC. The controlled experimental procedure allows characterising the performance results of three test phases for FOCUS.

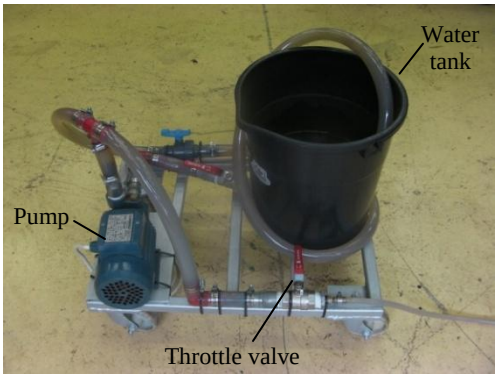

Figure 9.3 Water circulation system showing throttle valve to achieve the desired mass flow rate.

9.4 FOCUS performance results

The experimental methodology includes firstly characterising the performance at concentrator focus, by positioning the calorimeter at the focal spot. The second test phase includes determining exit optical waveguide power and flux levels to estimate the cable transmission efficiency. A third experimental procedure involves positioning a lunar regolith simulant, JSC-1 at cable exit to establish the melting capabilities of FOCUS. Video footage demonstrating the experimental procedure to characterise the performance of FOCUS is supplied in a compact disc at the back of this dissertation.

9.4.1 Concentrator focus

The first phase of the experimental testing includes positioning the calorimeter at concentrator focus (Figure 9.2, left). Characterising the flux distribution at concentrator focus requires covering the copper plate with a series of reflective shields to limit exposure of concentrated rays onto the copper receiver. Ten discretised stages, q, were chosen to estimate the flux distribution, starting with no shield, representing full exposure of the copper plate, and ending with a reflective shield incorporating a small diameter opening. The exposed parts of the copper plate are labelled $s_1 - s_q$, with s_1 representing full plate exposure and s_q a 3 mm diameter opening (Figure 9.4). The 6 mm diameter reflective shield, s_7 represents the optical waveguide inlet. Several experiments were conducted for each shield to obtain the average power incident on the exposed copper surface. Subtracting successive exposed powers represents power values striking the area difference, or band between two reflective shields (Figure 9.5). The methodology allows for obtaining the flux distribution of the RAC onto a 60 mm diameter receiver using Equation 9.1, where $F_{band,s_q - s_{q+1}}$ is the band flux and P_{s_q}, $P_{s_{q+1}}$ are the average powers striking the exposed areas of the copper plate (A_{s_q} and $A_{s_{q+1}}$). A sample calculation to obtain the average power and flux using the 6

mm diameter reflective shield is given in Appendix D. Performance results for the ten stages are given in Table 9.1. The flux distribution of the results showing concentrator focal point performance is illustrated in Figure 9.6. Results show a peak flux level of 1528 kW/m^2 at an irradiance of 850 W/m^2 corresponding to a concentration of 1798 suns. Measured temperature values at concentrator focus showed peak values approaching 1500°C at irradiance levels in the region of 1000 W/m^2. Comparison of the experimental results with the theoretical ray tracing simulation of Case 8 for both the full copper plate and optical waveguide inlet is shown in Figure 9.7. In addition to flux concentration, average power striking the exposed surface of the calorimeter is also an indication of performance, as shown in Figure 9.8. Performance results indicate a similar trend to theoretical results with the discretised experimental steps approaching ray tracing simulation results. Expected differences in the two curves of Figure 9.8 result from the increase in heat losses due to surface area increasing towards the circumference of the copper plate. The heat losses due to increasing surface area were not modelled. Average efficiency results for the experimental power striking the plate show an 89% approximation to ray tracing simulations. Test results approximate the ray trace model, however neglect to show peak flux levels possibly due to insufficient reflective shield discretisations. Preliminary experiments were conducted using smaller reflective shields allowing a 2 mm and 1 mm diameter exposure of the copper surface, however results showed inconclusive performance levels. A possible reason is due to additional heat seepage onto the copper plate surface which amplifies results when smaller diameter reflective shields are used. The additional heat could result from convection from the reflective shield and radiation from the heated air surrounding the calorimeter. To obtain peak flux levels and comparative results, further performance testing using a radiometric device such as a Gardon flux sensor would be required.

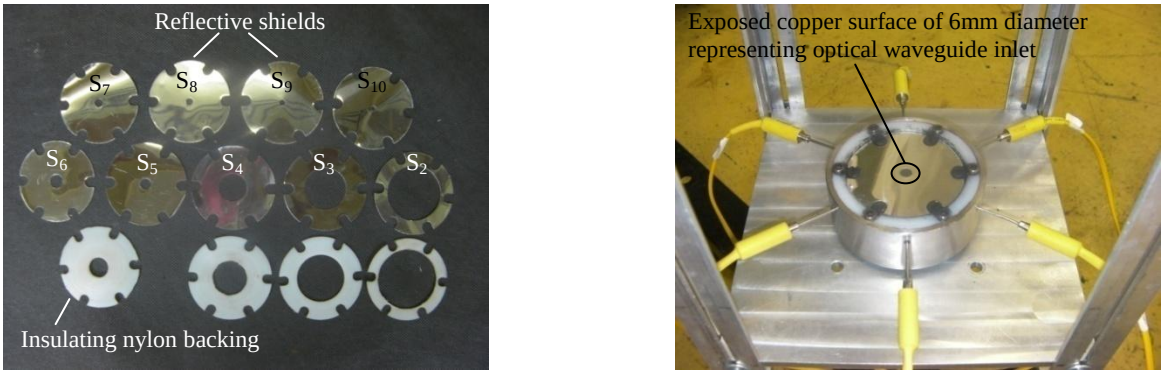

Figure 9.4 (left) The nine reflective shields with nylon backing used to characterise the average power striking the exposed copper surface. From the top right in an anti-clockwise direction, the shields (s_2 - s_{10}) allow copper exposure of diameter 3 mm, 4 mm, 5 mm, 6mm, 8 mm, 10 mm, 20 mm, 30 mm and 40 mm. (right) The 6 mm diameter reflective shield positioned at concentrator focus with a nylon backing to minimise conduction between the shield and copper surface.

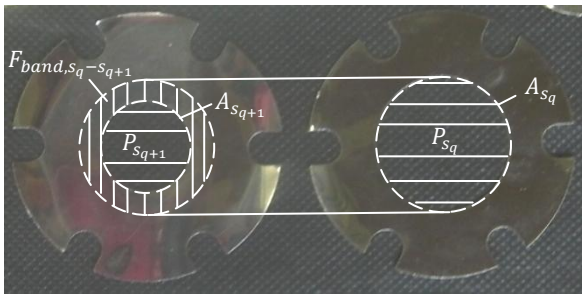

Figure 9.5 Two reflective shields illustrating the methodology used to obtain a band flux, $F_{band,s_q-s_{q+1}}$ on the copper surface. Shields on the left and right represent smaller, s_{q+1} and larger, s_q exposed surfaces respectively. Average powers striking the exposed surface are illustrated with $P_{s_{q+1}}$ and P_{s_q} on the areas $A_{s_{q+1}}$ and A_{s_q} respectively.

$$F_{band,s_q-s_{q+1}} = \frac{P_{s_q}-P_{s_{q+1}}}{A_{s_q}-A_{s_{q+1}}} \tag{9.1}$$

Table 9.1 Performance results at concentrator focus using the ten stages. Power and flux distribution results are normalised to 850 W/m^2 and represent an average of five experimental tests conducted for each reflective shield. Theoretical results represent ray tracing simulations at an irradiance of 850 W/m^2 with Case 8 scenario parameters modelled.

		Theoretical	**Experimental**				**Theoretical**	**Experimental**
Average power striking exposed copper plate surface (W)	P_{s_1}	137.7	118.5		**Average flux striking each band (kW/m^2)**	F_{band,s_1-s_2}	6.7	2.6
	P_{s_2}	127.2	114.4			F_{band,s_2-s_3}	16.2	10.2
	P_{s_3}	118.3	108.8			F_{band,s_3-s_4}	31.6	17.6
	P_{s_4}	105.9	101.9			F_{band,s_4-s_5}	97.6	117.6
	P_{s_5}	82.9	74.2			F_{band,s_5-s_6}	541.1	523.4
	P_{s_6}	67.6	59.4			F_{band,s_6-s_7}	1036.8	909.5
	P_{s_7}	44.8	39.4			F_{band,s_7-s_8}	1412.1	1296.4
	P_{s_8}	32.6	28.3			F_{band,s_8-s_9}	1570.3	1315.7
	P_{s_9}	21.5	19.0			$F_{band,s_9-s_{10}}$	1655.2	1491.5
	$P_{s_{10}}$	12.4	10.8			$F_{band,s_{10}}$	1754.2	1527.9

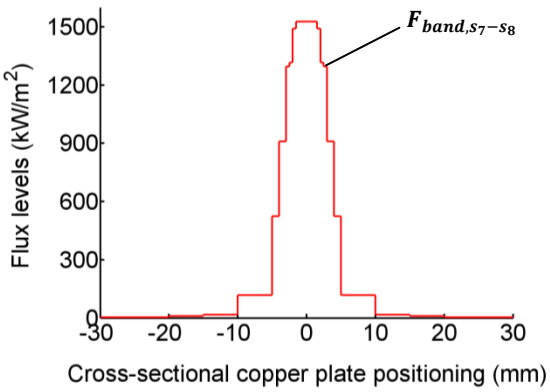

Figure 9.6 Experimental results showing the flux distribution at concentrator focus at a typical irradiance level of 850 W/m^2. Peak flux levels recorded are illustrated with the 3 mm diameter reflective shield.

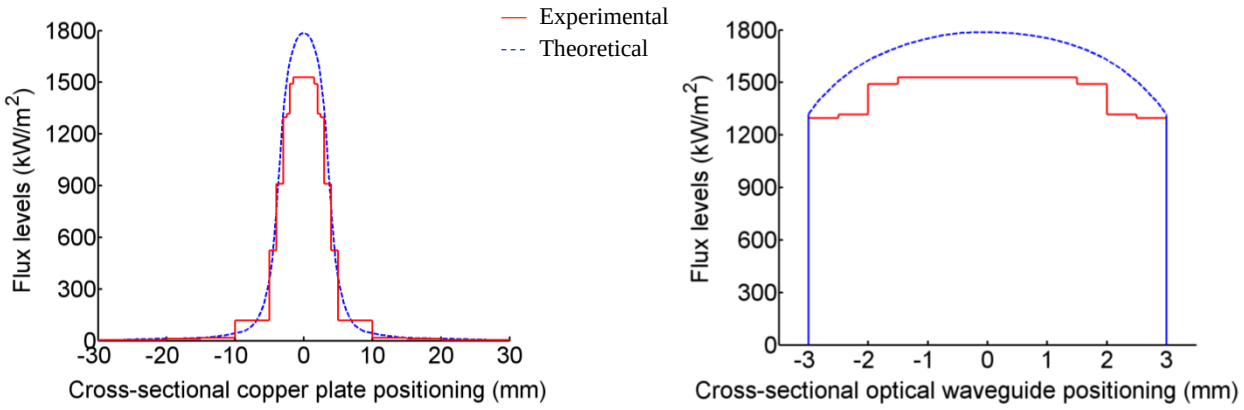

Figure 9.7 Performance results at concentrator focus showing flux levels striking the 60 mm diameter copper plate (left) and a magnified view of the 6 mm diameter inlet to the optical waveguide (right). Theoretical and experimental results illustrate performance levels at 850 W/m^2.

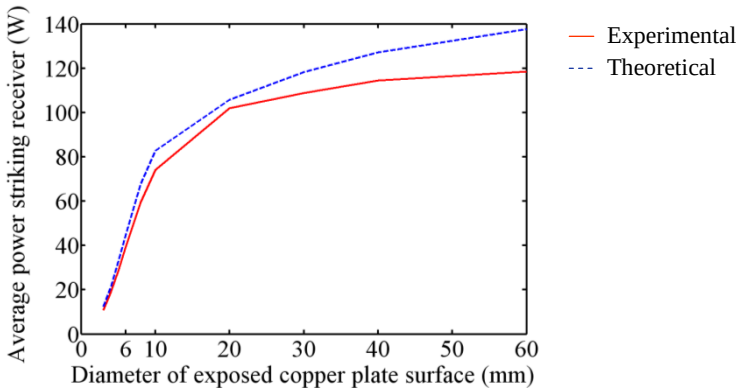

Figure 9.8 Average power striking calorimeter as a function of exposed copper surface diameter. Theoretical and experimental results illustrate performance levels at 850 W/m^2.

Key results from the first phase experiments include performance at optical waveguide inlet. Representative average power and flux levels incident on the cable of 39.4 W and 139.3 W/cm^2 respectively were observed over five experiments, as shown in Appendix D. An injected power into the 900 silica fibres of 33.5 W is estimated and is used in the calculating the transmission efficiency of the cable. Characterising outlet cable performance using similar energy balance methods permits the calculation of overall optical efficiency.

9.4.2 Optical waveguide exit

The procedure to obtain optical waveguide exit performance results involves aiming the waveguide at the calorimeter, as shown in Figure 9.2, right. Tests were conducted using the same methodology as at concentrator focus, however neglecting the copper plate reflective shields. A reflective shield was positioned at optical waveguide inlet to protect the metal ferrule from direct radiation concentrations that may cause damage (Figure 9.9, left). The shield allows concentrated energy entering only the 6 mm diameter quartz glass inlet of the cable. At cable outlet a preventative measure of offsetting the cable 5 mm away from the calorimeter centre, was taken to avoid reflection of sunlight back onto the bundle of fibres (Figure 9.9, right). Nonimaging optical theory allows predictions of the focal spot spread due to the additional 5 mm offset using Equation 9.2, where *VD* is the vertical displacement of the cable from the receiver and r_{VD} is the additional focal spot spread outside the diameter of the optical waveguide. Figure 9.10 illustrates the geometry involved showing the maximum half-angle cone of light exiting the cable as a function of numerical aperture and vertical distance. The flux striking the receiver is determined by the ratio of power to the size of the focal spot, which is defined by r_{VD} and r_{OWout} (Equation 9.3).

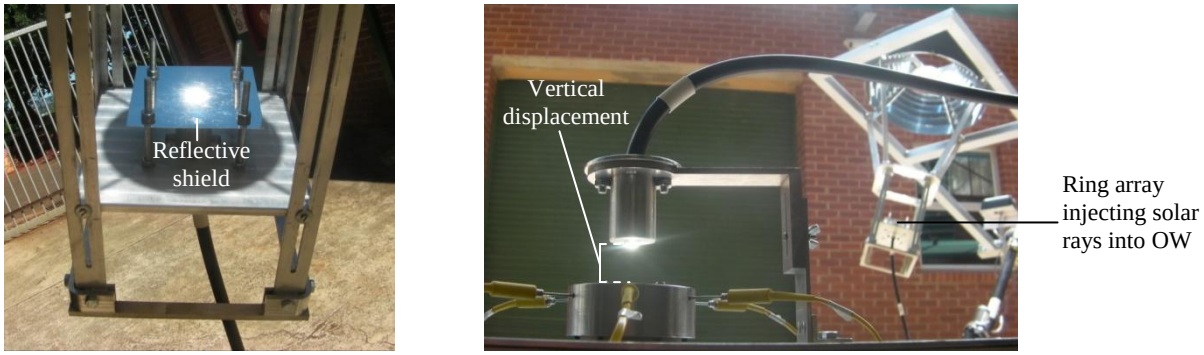

Figure 9.9 (left) Reflective shield at fibre optic cable inlet allowing concentrated solar energy into the 6 mm diameter quartz glass inlet. (right) Vertical displacement of the cable outlet prevents back reflection onto the 900 fibres resulting in cable damage.

$$tan(asin(NA)) = \frac{r_{VD}}{VD} \tag{9.2}$$

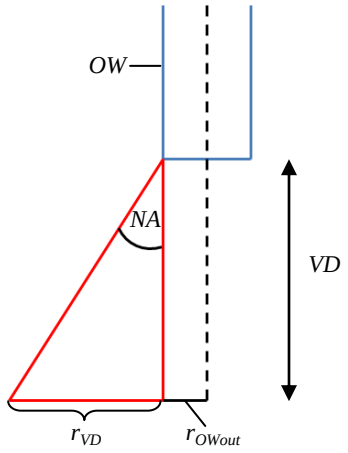

Figure 9.10 Diagram illustrating exit cable concentrations as a function of vertical displacement (*VD*) from the receiver. Numerical aperture, diameter of the exit quartz glass and distance from the receiver characterise the flux striking the target. Experiments were conducted using a 5 mm *VD* from calorimeter centre to prevent cable damage.

$$F_{Cu} = \frac{P_{Cu}}{\pi(r_{VD} + r_{OWout})^2} \tag{9.3}$$

Average performance results of five tests showed a power of 20.5 W striking the copper plate at a vertical displacement of 5 mm, corresponding to a flux of 84.9 W/cm^2 exiting the 900 fused fibres. The results represent normalised values at an irradiance of 850 W/m^2. Using equations 9.2, 9.3 and a power of 20.5 W, a theoretical representation of flux striking the copper plate versus displacement of the cable was modelled, as shown in Figure 9.11. The figure illustrates a rapid decrease in flux as the vertical displacement increases due to the cone shaped solar rays exiting the cable. Experimental results of the flux striking the receiver were obtained by estimating the diameter of the focal spot on the copper plate at respective vertical displacements. Flux results show a maximum power density of 30.2 W/cm^2 striking the plate at a 3 mm offset with flux levels unattainable below the 3 mm displacement in an attempt to prevent cable damage due to back reflection of light. The experimental trend however closely approximates theoretical calculations and flux levels approaching 85 W/cm^2 are assumed at cable exit.

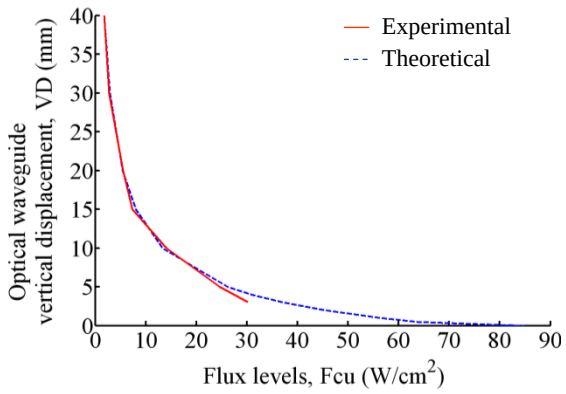

Figure 9.11 Relationship between vertical displacement of the optical waveguide to the flux concentration striking the copper surface. The trend represents an average power of 20.5 W striking the calorimeter at an irradiance of 850 W/m^2.

Transmission efficiency of the fibre optic cable is estimated at 61% using the average power results from the 6 mm diameter reflective shield, conducted at concentrator focus. A predicted efficiency of 95% was used for the theoretical calculations stipulated by the supplier of the cable. A possible reason for the 34% decrease in efficiency includes losses due to reflection at inlet. The reflective losses at cable inlet manifest due to the sudden change of refractive indices from air (n = 1.0) to fused quartz glass (n = 1.5). A solution to minimise inlet reflective losses is the design and implementation of a secondary concentrator at cable inlet to boost energy injection into the silica fibres, however this was beyond the scope of this work.

The results at cable exit represent performance at an irradiance of 850 W/m^2, however higher irradiance levels of 950 W/m^2 are attainable in KwaZulu-Natal. The increase in irradiance levels boosts flux concentrations from 84.9 W/cm^2 to 94.8 W/cm^2 which exceeds the minimum criterion to melt lunar regolith by 12%. Overall FOCUS optical efficiency calculations using the first two experimental phase results are discussed below.

9.4.3 Optical efficiency

Final performance results from the first two experimental phases are illustrated in Figure 9.12, which is an experimental representation of Figure 7.1. Calorimetric power results of 39.4 W and 20.5 W are shown at optical waveguide inlet and outlet respectively. Total system losses amount to 142.7 W, and primarily occur due to the solar half-angle and slope errors. The results allow calculating the optical efficiency of FOCUS using the incident power on the aperture area and the exit optical waveguide power obtained from the calorimetric experiments (Table 9.2). A predicted efficiency of 22% was obtained using ray tracing methods and a worst case error scenario for the system while experimental results demonstrate an

efficiency of 13%. Contributing factors for the decrease in system performance include fibre optic cable inlet reflective losses as previously discussed above.

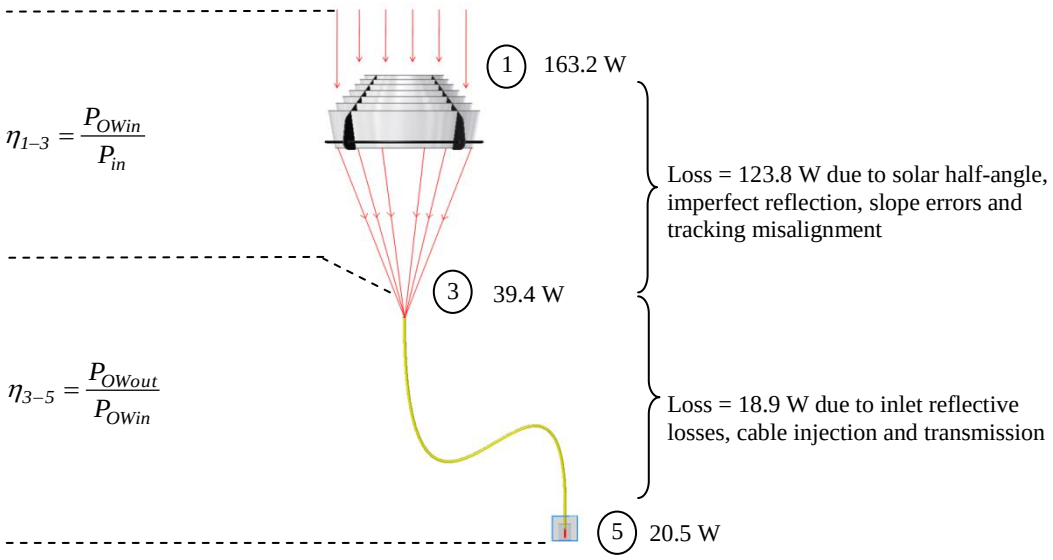

Figure 9.12 Realised optical efficiency stages for FOCUS. The power values given are based on a nominal input flux of 850 W/m^2 acting on an aperture of 0.192 m^2. Calorimetric experiments showed representative optical waveguide inlet and outlet powers of 39.4 W and 20.5 W respectively.

Table 9.2 Performance results of FOCUS. Experimental results were normalised to an irradiance value of 850 W/m^2 and represent an average of five tests conducted.

	Theoretical	**Experimental**
Power at cable inlet, P_{OWin} (W)	44.8	39.4
Fibre optic inlet flux, F_{OWin} (W/cm^2)	158.4	139.3
Flux concentration, cable inlet, $C_{flux,\ OWin}$ (suns)	1864.1	1638.8
Power at cable outlet, P_{OWout} (W)	36.3	20.5
Fibre optic outlet flux, F_{OWout} (W/cm^2)	150.5	84.9
Flux concentration, cable outlet, $C_{flux,\ OWout}$ (suns)	1770.9	998.8
Overall optical efficiency, $\eta_{overall}$	0.22	0.13

9.4.4 Regolith melting capabilities

The final test procedure includes conducting several melting experiments with FOCUS concentrating sunlight on to a lunar regolith simulant, JSC-1. The aim of the experiment is to demonstrate the high surface temperatures and flux levels required to melt lunar regolith for applications stipulated in Table 2.1 (Nakamura and Senior, 2004).

The experimental procedure includes positioning the optical waveguide over the JSC-1 surface and measuring the temperature of the melt zone formed after six minutes (Figure 9.13). A downward facing reflective shield was positioned beneath the cable to prevent reflected solar rays off the regolith surface from striking the cable. The temperature of the regolith simulant was measured using a type K thermocouple approximately positioned at the center of the melt zone.

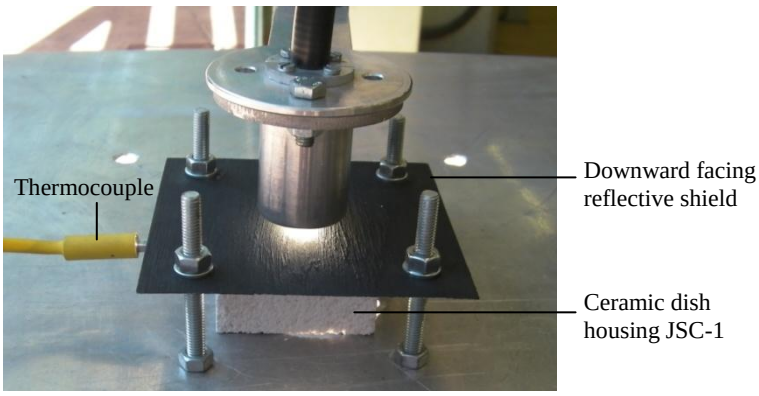

Figure 9.13 Regolith melting experiment, including a downward facing reflective shield and a thermocouple for the central melt temperature measurement. The lunar regolith simulant, JSC-1 was placed in a ceramic dish at a 5 mm vertical displacement from the cable.

Figure 9.14 shows a post experimental observation of the melted regolith from a typical experiment. The vitrified circular melt zone formed after six minutes is 6 mm in diameter having a depth of 2.5 mm. Table 9.3 summarises the peak melt temperature readings obtained for five separate experiments. The stabilisation of temperature within the melt zone is illustrated in Figure 9.15 with peak temperature values graphed against estimated flux levels. Flux levels exiting the cable were estimated using average irradiance levels over the six minute test period and the optical efficiency value from the first two experimental phases. Salient results show a peak temperature exceeding 1200 K at cable exit flux levels of 104 W/cm^2 which exceeds the minimum flux criterion for successfull regolith melting by 22%. Temperature results achieved can be applied to several high temperature lunar ISRU processes, including oxygen production and surface stabilisation, as shown in Table 2.1. To demonstrate lunar surface stabilisation a test sample was positioned beneath the cable and shifted at 60 second intervals to a achieve an ‘S’ shaped sintered regolith geometry (Figure 9.16). The sintered geometry shows the ability of high-flux solar concentrators to develop stable lunar surfaces for safe robotic and human activity. Creating larger sintered surfaces for practical human use on the lunar surface is possible by implementing multiple collectors and autonomous mechanisms to drive the fibre optic cable in the necessary intervals. In addition the integration of several fibre optic cables to achieve a larger exit area of concentrated energy

permits more efficient sintering of regolith per unit area. Similar technologies have been designed and tested using a quartz glass rod for the assembly of several fibre optic cables (Nakamura and Smith, 2011).

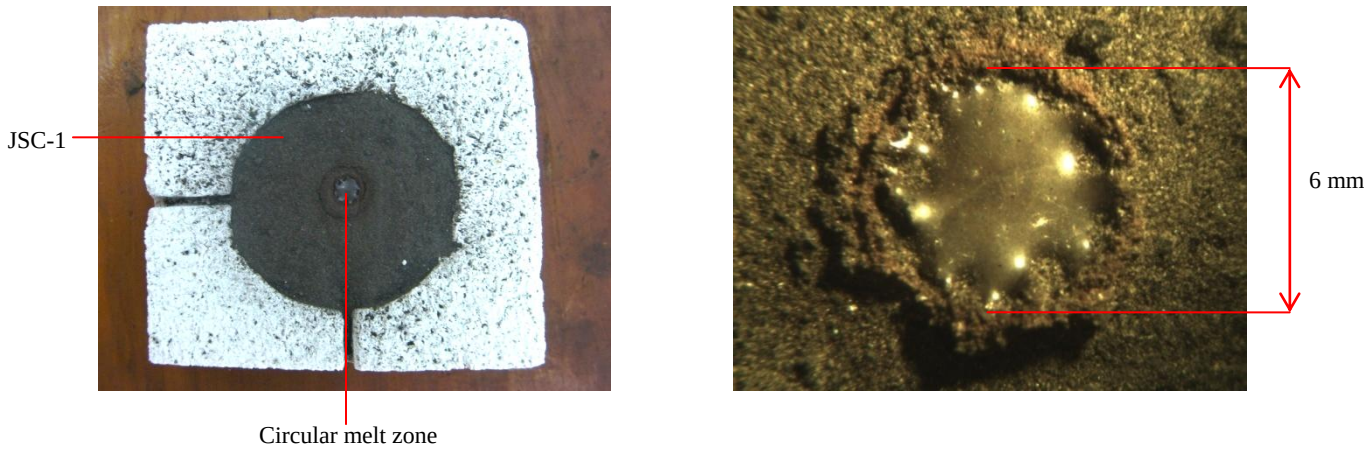

Figure 9.14 (left) Post experimental observations of JSC-1 in the ceramic dish showing a circular melt zone with (right) a magnified view of the vitrified melt having an estimated diameter of 6 mm and depth 2.5 mm.

Table 9.3 Lunar regolith simulant peak melt temperature and cable exit flux concentration results.

	Experiment				
	#1	**#2**	**#3**	**#4**	**#5**
Irradiance level (W/m^2)	1005.44	997.05	995.69	991.25	987.94
Peak temperature (°C)	935.51	901.62	882.04	876.91	850.41
Flux level (W/cm^2)	103.95	103.08	102.94	102.48	102.14

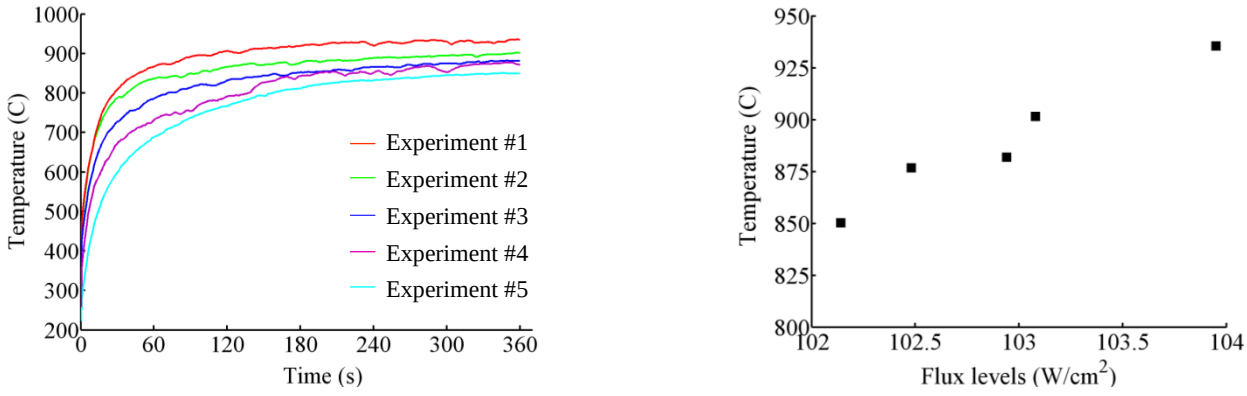

Figure 9.15 (left) Time evolution of the melt temperature for each of the five experiments. Temperature stabilisation in the melt zone is evident over the six minute test period. (right) Peak melt temperatures vs. flux levels at cable exit. Flux results represent a maximum value exiting the 900 silica fibres at varied irradiance levels.

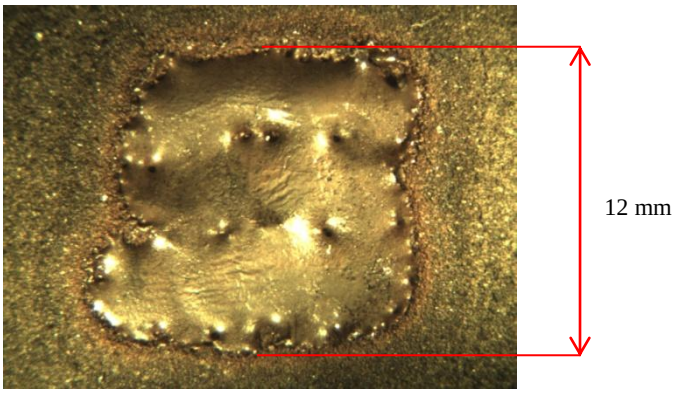

Figure 9.16 A vitrified sample of JSC-1 illustrating an ‘S’ shaped geometry obtained by shifting the regolith beneath the cable in intervals of 60 seconds. The sample approximates a square geometry with 12 mm sides and shows the ability of lunar surface stabilisation using concentrated solar energy.

10. CONCLUSION

Optical systems have previously demonstrated the achievement of high-flux solar concentrations for various energy intensive applications. This study investigated the collection of solar energy using an alternate concentrator design and its transmission through optical fibres for space related ISRU research. Research aims included the design, construction and testing of a prototype optical system, known as the Fibre Optic Concentrating Utilisation System (FOCUS). The objective of achieving a flux criterion of 85 W/cm^2 was exceeded to successfully melt a lunar regolith simulant using solar energy. Operating procedure for the system includes a composite material ring array concentrator injecting solar rays into a fibre optic cable where the high-flux concentrations are transported to a remote target. The outline for this study entailed four salient aspects, including a review of the relevant literature for optical systems, the design and construction of FOCUS, a theoretical model of system performance, and finally validation of the theory using experimental procedures.

The first part of this dissertation surveyed previous optical systems comprising of solar collectors and their evolution with fibre optic cables for applications such as solar power, solar surgery and space research. Key knowledge gained from the survey included the operating principles of point focus geometries in the form of common paraboloidal dish concentrators. A novel nonimaging concentrator was recognised as an alternative to the dish and comprises a set of paraboloidal reflective elements to concentrate sunlight to a common point. Advantages over the dish include rearward focusing and the potential to outperform the dish geometry at shorter focal lengths. The characteristic of single stage reflection to an upward facing receiver which facilitates receiver maintenance was motivation for using the ring array concentrator for concentrating energy into the fibre optic cable.

The design and construction of the optical system incorporates the use of nonimaging optical theory for system design. The methodology included using properties of the fibre optic cable in conjunction with paraboloidal geometries to obtain a seven element ring array concentrator reflecting rays into the acceptable light aperture. Construction objectives for the seven elements were to produce a low-cost, rigid and light ring array configuration. For this reason, composite material fabrication techniques were chosen for their mouldable characteristics to potentially minimise geometry imperfections. An optical error analysis on the manufactured elements showed slope errors between 5.67 mrad and 2.90 mrad which are comparable to other concentrators manufactured using similar methods, such as the parabolic tough constructed by Arasu and Sornakumar (2007) which has a surface slope error of 6.60 mrad.

The third part of this investigation involved a numerical analysis to estimate the performance of the system in the presence of errors at typical irradiance levels of 850 W/m^2. The analysis addressed the manufacturing process of the concentrator by characterising the optical and pointing errors resulting from the composite material process. The imperfect final array was modeled using ray trace methods and then compared to a set of progressively distorted array elements, each varying in a predetermined way from the ideal geometry. The optical efficiency of FOCUS was estimated at 22% with a flux at cable outlet of 150.5 W/cm^2.

The final section of this study was to validate the theoretical model with experimental methods. Literature on several methods to characterise the performance of point focus concentrators was gathered with an aim to provide a low-cost approach. An energy balance methodology using a flat plate calorimeter in conjunction with a heat transfer analysis was chosen. The experimental procedure was divided into three phases with primary aims to determine: 1) the power entering and 2) exiting the fibre optic cable and 3) the melting capabilities of lunar regolith. Concluding remarks for the first experimental phase was the close approximation of the test procedure to ray tracing simulations, with peak flux levels approaching 1800 suns at temperatures exceeding 1450°C. Average optical waveguide inlet power and flux values of 39.4 W and 139.3 W/cm^2 were obtained respectively, corresponding to a concentration of 1639 suns. Injected power into the 900 silica fibres was estimated at 33.5 W due to the geometry of the hexagonal fibres. Peak flux levels within the 3 mm diameter reflective shield could not be characterised due to inconclusive experimental testing. Further work to characterise peak flux levels should be investigated using methods such as radiometry. Phase two in the experimental procedure consisted of determining exit fibre optic performance. Results showed a representative exit power and flux level of 20.5 W and 84.9 W/cm^2 respectively, corresponding to a cable transmission efficiency of 61%, which contradicts the expected performance of 95%. Possible reasons for the reduction in efficiency are cable inlet reflective losses. Overall optical efficiency of FOCUS amounted to 13% resulting in a 9% decrease from the theoretical model, indicating further simulation refinements are required with regard to reflective losses at inlet. Finally FOCUS was used to demonstrate its usefulness as a test bed for lunar ISRU research by successfully melting a lunar regolith simulant, JSC-1 at a peak temperature exceeding 900°C. The estimated flux level at cable exit for the test amounted to 104.0 W/cm^2, which exceeds the minimum design flux criterion of 85 W/cm^2 by 22%. The performance results obtained can be applied to several ISRU applications. As an example, FOCUS was used to sinter a square geometry to demonstrate its applicability to lunar surface stabilisation, which enhances spacecraft and human mobility on the Moon. The successfull melting of JSC-1 using FOCUS gives a firm platform for future development in concentrating optics using single-stage reflection ring array technology.

Future work related to optimising the efficiency and performance of FOCUS includes improved manufacturing procedures for a ring array concentrator and integration of a secondary concentrator to boost injection into optical fibres. Composite material construction techniques can potentially be improved by reducing the curvature for element design. A thorough analysis of structural distortion during curing of the composites could lead to better lay-up design and material selection. These and other improvements would reduce surface slope errors and increase overall optical efficiency of the concentrating system. To supplement light injection into the cable a secondary concentrator such as a refractive or nonimaging hollow reflective type should be investigated. Successful implementation of a secondary device would re-focus the concentrated solar rays provided by the RAC and reduce the input light aperture onto the cable, resulting in additional light injection.

The primary aim to design, construct and test a ring array solar concentrator was successfully met, with flux levels exceeding the required minimum. To establish the ring array concentrator as a competitor to other point-focus technologies, such as the much used parabolic dish and Fresnel lens, a further comparison investigation is required. The proposed study should involve the design, construction and testing of a point-focus technology with similar characteristics, such as aperture area and focal length, as the ring array concentrator designed in this research. With the exception of a Fresnel lens, a parabolic dish should be constructed in a method similar to the composite material technique used in this study. Key differences and similarities should be revealed under manufacturing feasibility, performance, cost and spatial constraints.

The investigation of injecting solar rays into optical fibres for high-flux applications has been successfully demonstrated using FOCUS. Salient performance metrics include flux levels of 1000 suns at cable exit with temperatures exceeding 1200 K. Performance characteristics can be applied to several terrestrial and space-based applications, such as solar power generation, solar surgery, lunar ISRU research and HCPV.

REFERENCES

Abengoa Solar, http://www.abengoasolar.com/corp/web/en/our_projects/solucar [Accessed: 14/06/2011].

Alanod, http://www.alanod.com/opencms/opencms/Technik/datenblaetter.html [Accessed: 14/06/2011].

Arasu, V.A. and Sornakumar, T. "Design, manufacture and testing of fiberglass reinforced parabola trough for parabolic trough solar collectors" Solar Energy Vol. 81, pp. 1273-1279, 2007.

Ballestrín, J. "A non-water-cooled heat flux measurement system under concentrated solar radiation conditions" Solar Energy Vol. 73, pp. 159-168, 2002.

Ballestrín, J., Ulmer, S., Morales, A., Barnes, A., Langley, L.W. and Rodriguez, M. "Systematic error in the measurement of very high solar irradiance" Solar Energy Materials and Solar Cells Vol. 80, pp. 375-381, 2003.

Ballestrín, J., Estrada C.A., Rodríguez-Alonso, M., Pérez-Rábago, C., Langley, L.W. and Barnes, A. "High-heat-flux sensor calibration using calorimetry" Metrologia Vol. 41, pp. 314-318, 2004.

Ballestrín, J.and Monterreal, R. "Hybrid heat flux measurement system for solar central receiver evaluation" Energy Vol. 29, pp. 915-924, 2004.

Ballestrín, J., Estrada, C.A., Rodríguez-Alonso, M., Pérez-Rábago, C., Langley, L.W. and Barnes, A. "Heat flux sensors: Calorimeters or radiometers?" Solar Energy Vol. 80, pp. 1314-1320, 2006.

Brooks, M.J. and Roberts, L.W. "Establishment of a broadband radiometric ground station on the South African east coast" Proceedings of SPIE Optics and Photonics Vol. 7410, San Diego, CA, August 1-6, 2009.

CeramOptec, http://www.ceramoptec.com/filephotos/pdf/PowerLightGuides.pdf [Accessed: 14/06/2011].

Chong, K.K. and Wong, C.W. "General formula for on-axis sun-tracking system and its application in improving tracking accuracy of solar collector" Solar Energy Vol. 83, pp. 298-305, 2009.

Cope, A.W.G. and Tully, N. “Simple tracking strategies for solar concentrations” Solar Energy Vol. 27, pp. 361-365, 1981.

Duffie, J.A and Beckman, W.A. *Solar engineering of thermal processes*, John Wiley & Sons, Inc., United States, 2006.

Estrada, C.A., Jaramillo, O.A., Acosta, R. and Arancibia-Bulnes, C.A. “Heat transfer analysis in a calorimeter for concentrated solar radiation measurements” Solar Energy Vol. 81, pp. 1306-1313, 2007.

Fernandez-Reche J., Sanchez M., Alonso M., Canadas I., Chenlo F., Rodriguez J. and Ballestrin J. “Concentrating PV: An alternative to calorimeters for measuring high solar flux densities” Journal of Solar Energy Engineering Vol. 130, pp. 044502-1 – 044502-3, 2008.

Feuermann, D., Gordon, J.M. and Huleihil, M. “Solar fiber-optic mini dish concentrators: First experimental results and field experience” Solar Energy Vol. 71, pp. 459-472, 2002.

Feuermann, D. and Gordon, J.M. “High-concentration photovoltaic designs based on miniature parabolic dishes” Solar Energy Vol. 70, pp. 423-430, 2001.

Feuermann, D. and Gordon, J.M. “Solar fiber-optic mini-dishes: A new approach to the efficient collection of sunlight” Solar Energy Vol. 65, pp. 159-170, 1999.

Feuermann, D. and Gordon, J.M. “Solar surgery: remote fiber optic irradiation with highly concentrated sunlight in lieu of lasers” Opt. Eng. Vol. 37, pp. 2760-2767, 1998.

Gordon, J.M., Feuermann, D., Huleihil, M., Mizrahi, S. and Shaco-Levy, R. “Solar surgery” Journal of Applied Physics Vol. 93, pp. 4843-4851, 2003.

Gordon, J.M., Feuermann, D. and Huleihil, M. “Laser surgical effects with concentrated solar radiation” Applied Physics Letters Vol. 81, pp. 2653-2655, 2002.

Hughes, R.O. “Effects of tracking errors on the performance of point focusing solar collectors” Solar Energy Vol. 24, pp. 83-92, 1980.

Incropera, F.P., Dewitt, D.P., Bergman, T.L. and Lavine, A.S. *Fundamentals of heat and mass transfer 6th ed.*, John Wiley & Sons, Inc., United States, 2007.

Jaramillo, O.A., Pérez-Rábago, C.A., Arancibia-Bulnes, C.A. and Estrada, C.A. "A flat-plate calorimeter for concentrated solar flux evaluation" Renewable Energy Vol. 33, pg. 2322-2328, 2008.

Johnston, G. "Focal region measurements of the 20m^2 tilted dish at the Australian National University" Solar Energy Vol. 63, pp. 117-124, 1998.

Jones, S.A. "VSHOT measurements of distal II dish concentrators" SAND98-2778C, Sandia National Laboratories, 1998.

Kalogirou S.A. "Solar thermal collectors and applications" Progress in Energy and Combustion Science Vol. 30, pp. 231-295, 2004.

Kumler, J.J. and Caldwell, J.B. "Measuring surface slope error on precision aspheres' Proceedings of SPIE Optics and Photonics, 2007.

Kunene, K.R., Brooks, M.J., Roberts, L.W. and Zawilska, E. "Introducing GRADRAD: The Greater Durban Radiometric Network" Proceedings of World Renewable Energy Congress XI, Abu Dhabi, UAE, September 25-30, 2010.

Kribus, A., Zik, O. and Karni, J. "Optical fibers and solar power generation" Solar Energy Vol. 68, pp. 405-416, 2000.

Mavromatakis, F. and Franghiadakis, Y. "A highly efficient novel azimuthal heliotrope" Solar Energy Vol. 82 pp. 336-342, 2008.

Menq, C. and Chen, F.L. "Curve and surface approximation from CMM measurement data" Computers ind. Engng Vol. 30, pp. 211-225, 1996.

Mills, D.R. and Morrison, G.L. "Compact linear Fresnel reflector solar thermal powerplants" Solar Energy Vol. 68, pp. 263-283, 2000.

Mousazadeh, H., Keyhani, A., Javadi, A., Mobli, H, Abrinia K. and Sharifi, A. "A review of principle and sun-tracking methods for maximizing solar systems output" Renewable and Sustainable Energy Reviews Vol. 13, pp. 1800-1818, 2009.

Nakamura, T. and Smith, B.K. "Solar power system for lunar ISRU applications" Proceedings of 48th AIAA Aerospace Sciences Meeting Including the New Horizons Forum and Aerospace Exposition, Orlando, FL, 4-7 January, 2011.

Nakamura, T. and Smith, B.K. "Solar thermal system for lunar ISRU applications: Development and field operation at Mauna Kea, HI" Proceedings of 48th AIAA Aerospace Sciences Meeting Including the New Horizons Forum and Aerospace Exposition, Orlando, FL, 4-7 January, 2011.

Nakamura, T. and Smith, K.B. "Solar Thermal Power System for Oxygen Production from Lunar regolith" Proceedings of AIAA Space Conference and Exposition, Pasadena, CA, 14-17 September, 2009.

Nakamura, T. "Optical waveguide system for solar power applications in space" Proceedings of SPIE Optics and Photonics, San Diego, CA, 1-6 August, 2009.

Nakamura, T. and Senior, C.L. "Solar Thermal Power System for lunar materials processing" Journal of Aerospace Engineering Vol. 21, pp. 91-101, 2008.

Nakamura, T., Van Pelt, A.D, Gustafson, R.J and Clark, L. "Solar thermal power system for oxygen production from lunar regolith" Proceedings of Space Technology and Applications International Forum, Albuquerque, NM, 10-14 February, 2008.

Nakamura, T. and Senior, C. "Solar Energy System for In-Situ Resource Utilization" Proceedings of AIAA Space Conference and Exhibit, San Diego, CA, 28-30 September, 2004.

New scientist, http://www.newscientist.com/article/dn4009-optic-fibre-delivers-solar-surgery [Accessed: 14/06/2011].

NIST/SEMATECH e-Handbook of Statistical Methods, http://www.itl.nist.gov/div898/handbook [Accessed: 10/04/2010].

Odeh, S.D., Morrison, G.L. and Behnia, M. “Modelling of parabolic trough direct steam generation solar collectors” Solar Energy Vol. 62, pp. 395-406, 1998.

Pérez-Rábago, C.A., Marcos, M.J., Romero, M. and Estrada, C.A. “Heat transfer in a conical cavity calorimeter for measuring thermal power of a point focus concentrator” Solar Energy Vol. 80, pp. 1434-1442, 2006.

Pottler, K., Lupfert, E., Johnston, G., Shortis, M.R. “Photogrammetry: A powerful tool for geometric analysis of solar concentrators and their components” ASME Vol. 127 pp. 94-101, 2005.

Power technology, http://www.power-technology.com/projects/maricopasolarplantar [Accessed: 14/06/2011].

Pregger T., Graf D., Krewitt W., Sattler C., Roeb M. and Moller S. “Prospects of solar thermal hydrogen production processes” International journal of hydrogen energy Vol. 34 pp. 4256-4267, 2009.

Seboldt, W. “Space-and Earth-based solar power for the growing energy needs of future generations” Acta Astronautica Vol. 55, pp. 389-399, 2004.

Sen, Z. “Solar energy in progress and future research trends” Progress in Energy and Combustion Science Vol. 30, pp. 367-416, 2004.

Shirley, P. and Wang, C. “Distribution ray tracing: Theory and practice” Proceedings of the Third Eurographics Workshop on Rendering, Bristol, United Kingdom, pp. 33-43, 1992.

Shortis, M.R. and Johnston, G.H.G. “Photogrammetry: A powerful tool for geometric analysis of solar concentrators and their components” ASME Journal of Solar Energy Engineering Vol. 118, pp. 146-150, 1996.

Small Power Systems, http://www.smallpowersystems.com [Accessed: 14/06/2011].

Stine, W.B. and Harrigan, R.W. *Solar energy fundamentals and design: with computer applications*, John Wiley & Sons, Inc., United States, 1985.

Teti, R. “Machining of composite materials” CIRP Annals, Manufacturing Technology Vol. 51, pp. 611-634, 2002.

Ulmer, S. Heller, P. and Reinalter, W. “Slope measurements of parabolic dish concentrators using color-coded targets” Journal of Solar Energy Engineering Vol. 130, pp. 011015-1-5, 2008.

Vasylyev S.V., Vasylyev V.P. and Sergeev, V.A “Concept and design of ‘Flat-plate’ CPV module based on ring-array concentrator” Proceedings of 35th IEEE Photovoltaic Specialists Conference (PVSC), Honolulu, HI, June 20-25, 2010.

Vasylyev S. “Nonimaging reflective lens concentrator” Proceedings of the International Conference on Solar Concentrators for the Generation of Electricity or Hydrogen, Scottsdale, AZ, May 1-5, 2005.

Vasylyev S. and Vasylyev V. “Nonimaging reflective lenses: A new type of high-heat solar collector” Proceedings of the Solar World Congress, Orlando, Fl, 2005.

Vasylyev, S.V. and Vasylyev V.P “Non-imaging system for radiant energy flux transformation” Patent No. US 6620995, 2003.

Vasylyev V., Vasylyev S. “Expected optical performances of novel type multi-element high-heat solar concentrators” Proceedings of the American Solar Energy Society, Reno, NV, 2002.

Vasylyev, V.P. “Concentrator of radiant energy ‘Peresvet’ and the manufacturing method” USSR Patent No. SU 1023270, in Russian, 1981.

Welford, W.T. and Winston, R. *The optics of nonimaging concentrators*, Academic Press, United States, 1978.

Wendelin, T.J., Jorgensen, G.J. and Wood, R.L. “SHOT: a method for characterising the surface figure and optical performance of point focus solar concentrators” Proceedings of Second ASME-JSES-JSME International Solar Energy Conference, Reno, NV, pp. 555-560, 1991.

Wijeysundera, N.E. “Effect of angular misorientation on the performance of conical, spherical and parabolic solar concentrators” Solar Energy Vol. 19, pp. 583-588, 1977.

APPENDIX A

MATLAB SOFTWARE: OPTICAL SYSTEM DESIGN

MATLAB Code: Concentrating Optics Design Code (CODeC)

The design methodology for a ring array concentrator integrated with a fibre optic cable can be driven by any one of four primary variables, namely:

1) Aperture area (A_a)
2) Power incident on the concentrator (P)
3) Geometric concentration ratio (C)
4) Number of rings (k).

A flow chart illustrating the design process to obtain a RAC integrated with a fibre optic cable is illustrated in Appendix A.1. Each design method outputs the concentrator geometry required for the primary and secondary variables defined. For the primary variables of aperture area (A_a), power incident on the concentrator (P) and geometric concentration ratio, (C) CODeC initiates the design process using the respective equations after which following a common code to complete the design (Appendix A.2). For a design based on stipulating the number of rings, (k) CODeC starts by calculating the parameters of the first ring element progressing through to ring k (Appendix A.3).

Appendix A.1

MATLAB Code: Flow chart for RAC integrated with a fibre optic cable

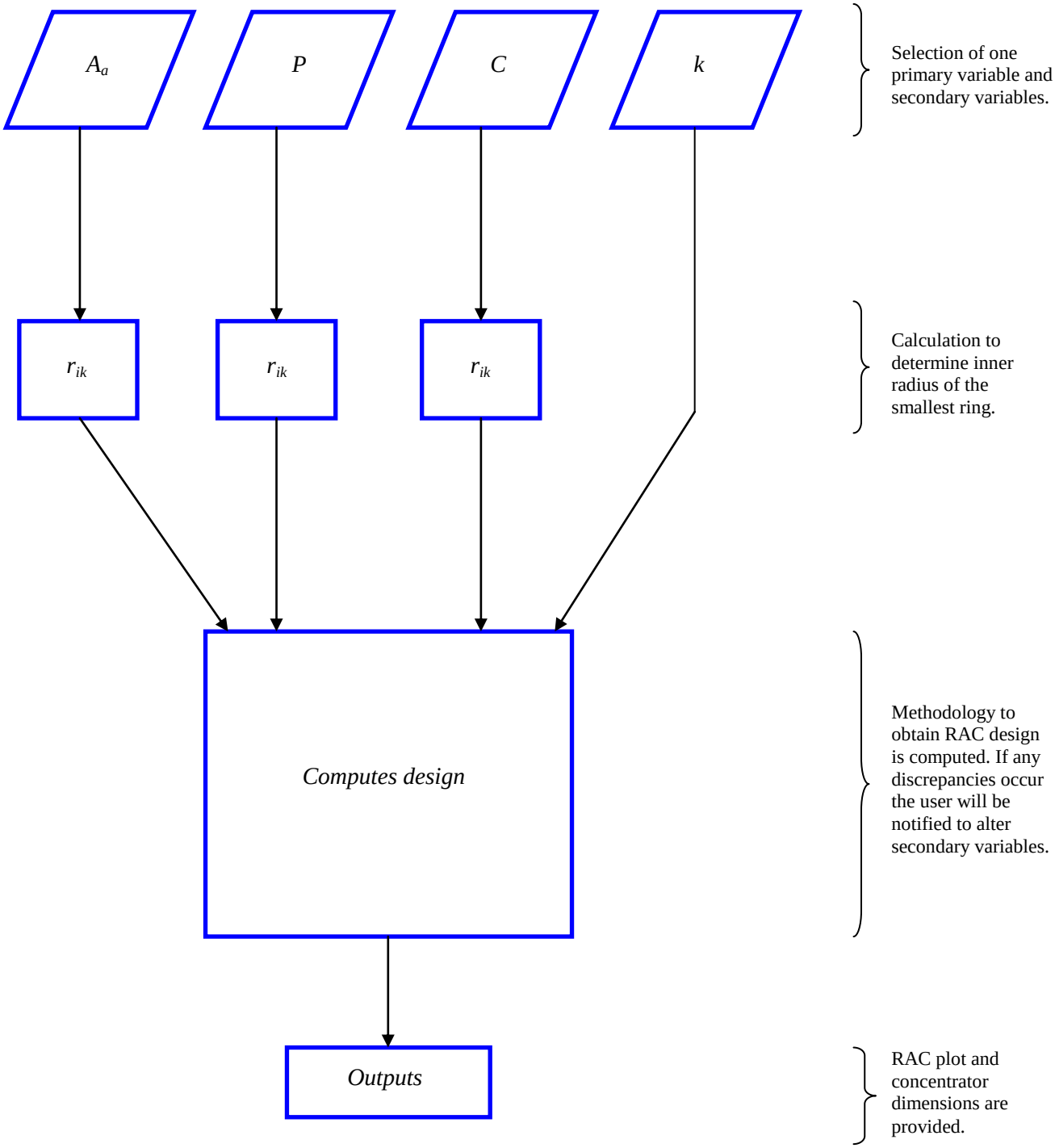

Appendix A.2

MATLAB Code: Concentrating Optics Design Code (CODeC) for A_a, P and C

1. Algorithm for aperture area (A_a)

```
%% User Defined Inputs - Aperture Area

Aperture Area = 192056;          % Aperture Area (mm^2)
outerringradius = 300;           % Required Concentrator Radius
OWoutletradius = 4.1;            % Required fibre optic inlet radius
NA = 0.37;                       % Numerical Aperture of fibre optic cable
ringheight = 150;                % Height of Concentrator Elements (Rings)
t = 3;                           % Thickness of rings
GF = 1;                          % Gradient factor
accuracy = 100;

%% Calculation to determine the required inner ring radius from the given
Aperture Area.

IRradius = (sqrt((Area-pi*outerringradius^2)/(-pi))); % Inner Ring Radius
if imag(IRradius) > 0
    disp('Error : The Area cannot be obtained from the given outer ring
radius and optical waveguide radius. Acion : Increase outer ring radius
and/or Decrease optical waveguide radius.');
end
```

2. Algorithm for power (P)

```
%% User Defined Inputs - Power incident on Concentrator

Power = 250;                     % Required Power
outerringradius = 300;           % Required Concentrator Radius
OWoutletradius = 4.1;            % Required fibre optic inlet radius
NA = 0.37;                       % Numerical Aperture of fibre optic cable
ringheight = 150;                % Height of Concentrator Elements (Rings)
t = 3;                           % Thickness of rings
GF = 1;                          % Gradient factor
accuracy = 100;

%% Calculation to determine the required inner ring radius for the given
Power.

IRradius = (sqrt(((Power/850) - (pi*(outerringradius/1000)^2))/-pi))*1000;
% Inner Ring Radius
if imag(IRradius) > 0
    disp('Error : The Power cannot be obtained from the given outer ring
radius and optical waveguide radius. Acion : Increase outer ring radius
and/or Decrease optical waveguide radius.');
end
```

3. Algorithm for geometric concentration ratio (*C*)

```
%% User Defined Inputs - Geometric concentration ratio

C = 9000;                           % Required Concentration Ratio
outerringradius = 500;              % Required Concentrator Radius
OWoutletradius = 3;                 % Required fibre optic inlet radius
NA = 0.37;                          % Numerical Aperture of fibre optic cable
ringheight = 150;                   % Height of Concentrator Elements (Rings)
t = 3;                              % Thickness of rings
GF = 1;                             % Gradient factor
accuracy = 100;

%% Calculation to determine the required inner ring radius for the given
conc. ratio.

IRradius = sqrt((-CR*pi*(OWoutletradius)^2 + pi*outerringradius^2)/pi);
% Inner Ring Radius
if imag(IRradius) > 0
    disp('Error : The concentration ratio cannot be obtained from the given
outer ring radius and optical waveguide radius. Acion : Increase outer ring
radius and/or Decrease optical waveguide radius.');
end
```

Common algorithm to complete CODeC for *Aa*, *P* and *C*

```
%% Check that Outer Radius is greater than inner radius

if IRradius >= outerringradius;
    disp('Error : The Area cannot be obtained from the given outer ring
radius and optical waveguide radius. Acion : Increase outer ring radius
and/or Decrease optical waveguide radius.')
end

%% Relevant Angles in RAC Design

values = xlsread('Table of theta values (NA 0.51).xlsx');

% Matlab reads excel spreadsheet to obtain correct theta value for the radius
that is required.
for v = 1:20;
    if outerringradius == values(v,1);
       theta = values(v,2);
    end
end

alpharequired = asind(NA);
% Max 1/2 angle that a ray of light can enter RAC
beta = ((180 - 90 -theta) + 90)/2;
% Bisect the angle of the incident ray and reflected ray.  This ensures
% angle of incidence = angle of reflection
```

```
gamma = 90 - beta;

% Properties of Ring 1

m1 = tand(90-gamma);
% To find the gradient at a point on a curved surface a tangent line must be
drawn at the point on the surface. The tan of the angle between the
tangent and the normal to the incident ray is the gradient.

a1 = m1/(2*(outerringradius-t));
% y1' = 2*a1*x, using gradient to find a1

u1 = sqrt((a1*(outerringradius-t)^2 - ringheight)/a1);
% Lower x co-ord of ring 1

f1 = 1/(4*a1);
% Focus of Ring 1

% Finding points along Ring 1
x(1,:) = linspace(outerringradius-t,u1, accuracy);
% x co-ord points on Ring 1
y(1,:) = a1*(x(1,:).*x(1,:));
% Equation of Ring 1

%% Check that calculated 1/2 angle (alphatrial) at focus (reflected ray from
Ring 1) corresponds to alpha required from NA of o/w

alphatrial = 90 - atand((y(1,10)-f1)/x(1,10));
% Calculated max. 1/2 angle from theta value.  This value must tend towards
the alpha required value, but must never exceed it.  If it exceeds or is too
far away from the alpha required value then theta needs to be altered :

if      alphatrial > alpharequired;
        disp('Error : Max. 1/2 angle calculated is greater than required 1/2
angle, Action : Decrease theta');
elseif  (alpharequired - 0.5 < alphatrial) && (alphatrial < alpharequired);
        disp( 'Good : Max. 1/2 angle calculated within 1/2 a degree of
required 1/2 angle');
elseif  (alphatrial < alpharequired -0.5);
        disp( 'Unsatisfactory : Max. 1/2 angle calculated is greater than 1/2
a degree difference of required 1/2 angle, Action : Increase theta');
end

%% Properties of Rib Supports 1 and 2
% Finding properties of Rib Support 1
% Rib Support 1 is a line from the bottom co-ord of Ring 1 to inner ring
radius of innermost Ring (calculated from conc. ratio).
mL1 = -GF;
% Gradient of Rib Support 1
cL1 = y(1,10) - mL1*x(1,10);
% y axis Intercept of Rib Support 1

% Finding properties of Rib Support 2
% Rib Support 2 is a line from the top co-ord of Ring 1 that is parallel to
Rib Support 1
```

```
mL2 = mL1;
% L1 is \\ to L2, Gradient of Rib Support 2
cL2 = y(1,1) - mL2*x(1,1);
% y axis Intercept of Rib Support 2

if mL1 >= 0;
    disp('Error : Area cannot be obtained, Action : Increase outer ring
radius')
end

k=1;
contin = true;
while(contin)

%% Ring k
% Properties of Ring k
% If k is equal to 1 code works out the second ring, then increases by 1 so k
equals to 2 and code works out third ring, code carries on to work out rings
until IRradius is achieved. Hence Conc. ratio is achieved

    if k == 1
        yL2 = mL2*(x(k,10) - t) + cL2;
% Ring k y-intersection with L2-Rib Support 2 (this forms the top co-ord of
Ring k), [x(k,10)-t] - this incorporates thickness in the design.
        syms a c
        [a c] = solve(yL2 - (a*(x(k,10) - t)^2+c), f1 - c - (1/(4*a)));
% Simultaneous equations to obtain values for a & c of Ring k
        a = eval(a(1));
        c = eval(c(1));
        hold
        % intersect with L1 with P2 (x value)
        syms n
        xL1 = solve(a*n^2 +c -(mL1*n +cL1));
% Simultaneous eq. to get Ring k x-intersection with L1-Rib Support 1 (this
forms the bottom co-ord of Ring k).
        x(k+1,10) = eval(xL1(1));
% finding points along P2
        x(k+1,:) = linspace(x(k,10)-t,x(k+1,10), accuracy);
% x axis values for Ring k
        y(k+1,:) = a*(x(k+1,:).*x(k+1,:))+c;
% Equation of Ring k
    else
        if x(k,10) >= IRradius
            yL2 = mL2*(x(k,10) - t) + cL2;  % y intersection with L2
            syms a c
            [a c] = solve(yL2 - (a*(x(k,10) - t)^2+c), f1 - c - (1/(4*a)));
            a = eval(a(1));
            c = eval(c(1));
            % intersect with L1 with P2 (x value)
            syms n
            xL1 = solve(a*n^2 +c -(mL1*n +cL1));
            x(k+1,10) = eval(xL1(1));
            % finding points along P2
            x(k+1,:) = linspace(x(k,10)-t,x(k+1,10), accuracy);
            y(k+1,:) = a*(x(k+1,:).*x(k+1,:))+c;
        else
```

```
            contin = false;
        end
    end
    k = k+1;
end

%% Solution Space

k = k-1;
% This shows the actual Ring No that will be drawn including the first ring
generated.

%Support Ribs Solution Space
xL1p = linspace(x(1,10),x(k,10),10);
% x values on Rib 1
yL1p = mL1*xL1p+cL1;
% Straight line from bottom of ring 1 to bottom of last ring
xL2p = linspace(outerringradius-t,x(k,1),10);
% x values on Rib 2
yL2p = mL2*xL2p+cL2;
% Straight line from top of ring 1 to top of last ring

% 1/2 angle Solution Space
m_osol_line = tand(90-alphatrial);
% Gradient of max 1/2 angle reflected rays will enter optical fiber optic.
c_osol_line = f1;
% Reflected rays will focus to focus of Ring 1
x_osol_line = linspace(0,x(1,10));
% x values of max Reflected rays
y_osol_line = m_osol_line*x_osol_line + c_osol_line;
% Straight line from bottom of ring 1 to focus

m_isol_line = (y(k,10) - f1)/x(k,10);
% Gradient of min 1/2 angle reflected rays will enter fiber optic.
c_isol_line = f1;
% Reflected rays will focus to focus of Ring 1
x_isol_line = linspace(0,x(k,10));
% x values of min Reflected rays
y_isol_line = m_isol_line*x_isol_line + c_isol_line;
% Straight line from bottom of last ring to focus
```

Appendix A.3

MATLAB Code: Concentrating Optics Design Code (CODeC) for *k*

---

4. Algorithm for number of rings (*k*)

```
format long                     % for higher precision
clear all
clc

%% User Defined Inputs - Number of rings

RingNo = 7;                     % Required number of rings
outerringradius = 500;          % Required Concentrator Radius
OWoutletradius = 4.1;           % Required fibre optic outlet radius
NA = 0.37;                      % Numerical Aperture of fibre optic cable
ringheight = 150;               % Height of Concentrator Elements (Rings)
t = 3;                          % Thickness of rings
GF = 1;                         % Gradient Factor
accuracy = 100;                 % Coordinate points to be used

%% Relevant Angles in RAC Design

values = xlsread('Table of theta values (NA 0.37).xlsx');
% Matlab reads excel spreadsheet to obtain correct theta value for the radius
that is required.
for v = 1:20;
    if outerringradius == values(v,1);
       theta = values(v,2);
    end
end

alpharequired = asind(NA);
% Max 1/2 angle that a ray of light can enter RAC

beta = ((180 - 90 -theta) + 90)/2;
% Bisect the angle of the incident ray and reflected ray.  This will ensure

% the angle of incidence = angle of reflection
gamma = 90 - beta;

% Properties of Ring 1

m1 = tand(90-gamma);

a1 = m1/(2*(outerringradius-t));
% y1' = 2*a1*x, using gradient to find a1

u1 = sqrt((a1*(outerringradius-t)^2 - ringheight)/a1);
% Lower x co-ord of ring 1
```

```
f1 = 1/(4*a1);
% Focus of Ring 1

% Finding points along Ring 1
x(1,:) = linspace(outerringradius-t,u1, accuracy);
% x co-ord points on Ring 1
y(1,:) = a1*(x(1,:).*x(1,:));
% Equation of Ring 1

%% Check that calculated 1/2 angle (alphatrial) at focus (reflected ray from
Ring 1) is close to alpha required from NA of o/w

alphatrial = 90 - atand((y(1,accuracy)-f1)/x(1,accuracy));
% Calculated max. 1/2 angle from theta value.  This value must tend towards
the alpha required value, but must never exceed it.  If it exceeds or is too
far away from the alpha required value then theta needs to be altered :

if      alphatrial > alpharequired;
        disp('Error : Max. 1/2 angle calculated is greater than required 1/2
angle, Action : Decrease theta');
elseif  (alpharequired - 0.5 < alphatrial) && (alphatrial < alpharequired);
        disp( 'Good : Max. 1/2 angle calculated within 1/2 a degree of
required 1/2 angle');
elseif  (alphatrial < alpharequired -0.5);
        disp( 'Unsatisfactory : Max. 1/2 angle calculated is greater than 1/2
a degree difference of required 1/2 angle, Action : Increase theta');
end

%% Properties of Rib Supports 1 and 2

% Finding properties of Rib Support 1
% Rib Support 1 is a line from the bottom co-ord of Ring 1 to

% inner ring radius of innermost Ring
mL1 = -GF;
% Gradient of Rib Support 1 is perpendicular to surface of Ring 1 (for ease
of manufacture)
cL1 = y(1,accuracy)-mL1*x(1,accuracy);
% y axis Intercept of Rib Support 1

% Finding properties of Rib Support 2
% Rib Support 2 is a line from the top co-ord of Ring 1 that

% is parallel to Rib Support 1 (for ease of manufacture)
mL2 = mL1;
% L1 is \\ to L2, Gradient of Rib Support 2
cL2 = y(1,1) - mL2*x(1,1);
% y axis Intercept of Rib Support 2

if mL1 >= 0;
    disp('Error : RAC cannot be obtained, Action : Increase Gradient Factor')
end
%% Ring k
```

```
% Properties of Ring k
% Calculates all the rings needed, until the Ring No. is reached (specified
in the user defined inputs)

for k = 1:RingNo-1
        yL2 = mL2*(x(k,accuracy) - t) + cL2;
% Ring k y-intersection with L2-Rib Support 2 (this forms the top co-ord of
Ring k), [x(k,10)-t] - this incorporates thickness in the design.
        syms a c
        [a c] = solve(yL2 - (a*(x(k,accuracy) - t)^2+c), f1 - c - (1/(4*a)));
% Simultaneous equations to obtain values for a & c of Ring k
        a = eval(a(1));
        c = eval(c(1));
% intersect with L1 with P2 (x value)
        syms n
        xL1 = solve(a*n^2 +c -(mL1*n +cL1));
% Simultaneous eq. to get Ring k x-intersection with L1-Rib Support 1 (this
forms the bottom co-ord of Ring k).
        x(k+1,accuracy) = eval(xL1(1));
% finding points along P2
        x(k+1,:) = linspace(x(k,accuracy)-t,x(k+1,accuracy), accuracy);
% x axis values for Ring k
        y(k+1,:) = a*(x(k+1,:).*x(k+1,:))+c;
% Equation of Ring k
end

%% Solution Space

%Support Ribs Solution Space
xL1p = linspace(x(1,accuracy),x(RingNo,accuracy),10);
% x values on Rib 1
yL1p = mL1*xL1p+cL1;
% Straight line from bottom of ring 1 to bottom of last ring
xL2p = linspace(outerringradius-t,x(RingNo,1),10);
% x values on Rib 2
yL2p = mL2*xL2p+cL2;
% Straight line from top of ring 1 to top of last ring

% 1/2 angle Solution Space
m_osol_line = tand(90-alphatrial);
% Gradient of max 1/2 angle reflected rays will enter optical fiber optic.
c_osol_line = f1;
% Reflected rays will focus to focus of Ring 1
x_osol_line = linspace(0,x(1,accuracy));
% x values of max Reflected rays
y_osol_line = m_osol_line*x_osol_line + c_osol_line;
% Straight line from bottom of ring 1 to focus

m_isol_line = (y(RingNo,accuracy) - f1)/x(RingNo,accuracy);
% Gradient of min 1/2 angle reflected rays will enter fiber optic.
c_isol_line = f1;
% Reflected rays will focus to focus of Ring 1
x_isol_line = linspace(0,x(RingNo,accuracy));
% x values of min Reflected rays
y_isol_line = m_isol_line*x_isol_line + c_isol_line;
% Straight line from bottom of last ring to focus
```

APPENDIX B

STATISTICAL ANALYSIS

Appendix B.1

ANOVA Test: Sample set data and results for element #7

The one way ANOVA test for element #7 is conducted to determine if the four profile scans (+X, -X, +Y, -Y) have no significant statistical differences. To conduct the test the following assumptions were made: 1) the four scans are or approximate a normal distribution, 2) the variances of the scans are equal and 3) the 98 data points per scan are independent. The CMM scans for the horizontal deviation analysis were processed to obtain slope error results for each point of the four profile scans (Table B.1). The four scans, m each have 98 data points, n with individual profile slope errors, φ_{RMS} shown to represent best and worst case scenarios of the profile trends. Using m, n and a 1% level of significance ($\alpha_{l.o.s} = 0.01$) for the ANOVA test the $F_{statistic}$ was calculated in a statistical software package called Statistical Package for the Social Science (SPSS). Table B.2 shows the results of the ANOVA test for element #7 indicating an $F_{statistic}$ of 2.649. The criterion in Equation 6.4 suggests the four profile trends can be pooled to obtain a sample of 392 observations for further statistical analysis.

Table B.1 Slope error values after processing CMM results in a 3D modeling package. The four profile scans (+X, -X, +Y, -Y) comprise 98 points each. Data results are in milliradians.

	Four profile scans (m = 4)			
	X +	**X -**	**Y +**	**Y -**
1	13.84115	13.35679	18.14315	13.13153
2	12.43827	12.19802	12.42385	10.23048
3	10.83763	11.02537	7.773528	7.775294
4	9.242036	10.06409	5.368462	5.856366
5	7.382167	9.215704	3.997835	4.445054
6	4.36604	8.317336	3.146582	3.472868
7	2.098653	7.242243	2.581025	2.762014
8	1.746445	6.171576	2.163169	2.218966
9	1.675437	5.249824	1.831691	1.794224
10	1.616701	4.510771	1.555674	1.458068
11	1.562922	3.934374	1.31818	1.193014
12	1.51187	3.486257	1.108394	0.988749
13	1.46269	3.137133	0.919594	0.839787
14	1.415023	2.863306	0.747478	0.735764
15	1.368734	2.638524	0.588387	0.652215
16	1.323745	2.446374	0.439837	0.585561
17	1.280099	2.278061	0.300416	0.536301
18	1.237953	2.127676	0.168795	0.504605

19	1.19733	1.991079	0.043929	0.490386
20	1.158445	1.865643	0.07466	0.493181
21	1.121499	1.749424	0.187376	0.512031
22	1.08669	1.64097	0.29434	0.545868
23	1.054338	1.539285	0.395278	0.59328
24	1.024767	1.443605	0.489322	0.652235
25	0.998362	1.353403	0.574851	0.712066
26	0.975583	1.268345	0.648553	0.764071
27	0.957007	1.188211	0.703254	0.807382
28	0.94234	1.112939	0.720411	0.84183
29	0.928573	1.042596	0.631366	0.867186
30	0.914933	0.977379	0.352732	0.883363
31	0.90137	0.91766	2.013916	0.890685
32	0.887796	0.864016	1.236422	0.889536
33	0.874165	0.817233	0.976506	0.880445
34	0.860349	0.77847	0.814557	0.863896
35	0.847803	0.749353	0.688368	0.840405
36	0.831915	0.732162	0.580116	0.810604
37	0.817211	0.730376	0.482705	0.775009
38	0.801928	0.748921	0.392418	0.734208
39	0.786017	0.785045	0.307268	0.690169
40	0.769422	0.82922	0.226121	0.645372
41	0.751963	0.878984	0.148286	0.600218
42	0.7336	0.931106	0.073383	0.554856
43	0.71429	0.98068	0.001247	0.509414
44	0.693806	1.020562	0.068115	0.464039
45	0.671985	1.04203	0.134512	0.418899
46	0.648877	1.036195	0.197545	0.37405
47	0.624396	0.995904	0.256607	0.329623
48	0.598382	0.917855	0.310617	0.28573
49	0.570732	0.803619	0.357958	0.242454
50	0.541332	0.659814	0.396492	0.199978
51	0.510165	0.517574	0.424411	0.158366
52	0.477137	0.403826	0.440505	0.117775
53	0.442835	0.314884	0.443829	0.078371
54	0.409875	0.246217	0.434488	0.04027
55	0.378833	0.194069	0.41369	0.003653
56	0.349739	0.155345	0.384066	0.031276
57	0.322631	0.127487	0.349201	0.064333
58	0.297474	0.108406	0.313138	0.09527
59	0.274188	0.096246	0.280349	0.123781
60	0.252851	0.089578	0.254437	0.149599
61	0.233524	0.087265	0.237771	0.17233
62	0.216114	0.088246	0.231633	0.191591

63	0.200675	0.091688	0.236333	0.206908
64	0.187185	0.096931	0.251449	0.217973
65	0.175631	0.103355	0.276256	0.225572
66	0.166047	0.110533	0.309625	0.229827
67	0.158356	0.118119	0.35163	0.2305
68	0.152637	0.125646	0.401382	0.227617
69	0.148977	0.13294	0.457175	0.221326
70	0.14726	0.13776	0.517826	0.211487
71	0.147442	0.132673	0.58257	0.197831
72	0.149571	0.117425	0.650821	0.180472
73	0.153677	0.09345	0.722098	0.159638
74	0.159729	0.061805	0.796107	0.13529
75	0.16772	0.023306	0.87263	0.107442
76	0.17686	0.021412	0.951531	0.07624
77	0.181876	0.07188	1.03272	0.041874
78	0.180686	0.127741	1.116165	0.004357
79	0.173378	0.18877	1.201893	0.035885
80	0.159939	0.254859	1.289952	0.078693
81	0.140254	0.326007	1.380424	0.123958
82	0.114376	0.402306	1.473528	0.170967
83	0.08233	0.483965	1.56953	0.219588
84	0.04412	0.571349	1.668755	0.266369
85	0.000294	0.664981	1.771654	0.306358
86	0.050955	0.765603	1.878796	0.339275
87	0.107815	0.87427	1.990953	0.365055
88	0.170892	0.992467	2.10933	0.383589
89	0.240203	1.122228	2.235329	0.394704
90	0.315742	1.266506	2.371118	0.398403
91	0.39753	1.429823	2.520528	0.394484
92	0.485573	1.619183	2.688924	0.382641
93	0.579887	1.846181	2.885234	0.362811
94	0.680474	2.13209	3.127879	0.334559
95	0.787364	2.520489	3.456303	0.297589
96	0.900556	3.122098	4.069323	0.251599
97	1.020065	4.295768	6.486818	0.196083
98	1.145955	6.904589	18.47561	0.130568
$\varphi_{\mathbf{RMS}}$	2.64	3.28	3.39	2.13
Scenario	-	-	WORST	BEST

Table B.2 ANOVA results for element #7. The test was conducted at the 1% level of significance.

Source of variation	**Sum of squares**	**Degrees of freedom**	**Mean square**	$\mathbf{F_{statistic}}$	$\mathbf{F_{critical}}$
Between profiles	51.08459	m-1 = 3	$MS_B = 17.028$	2.649	3.832
Within profiles	2494.078	m(n-1) = 388	$MS_W = 6.428$		
Total	2545.163	nm -1 = 391			

Appendix B.2

Sample results to statistically obtain the outliers for element #7

A statistical analysis to determine the outliers for element #7 was performed in SPSS to obtain improved representative results for slope error trends. The four profile scans are pooled together and listed in ascending order for further processing. Figure B.1 shows the histogram plot of the slope errors illustrating the pooled scans approximate a normally distributed function which complements the ANOVA test. To determine the outliers the methodology includes calculating the median (Q2), upper quartile (Q3), lower quartile (Q1) and the inter-quartile range (IQR) shown in the box-and-whisker plot of Figure B.2. The software package uses Equations B.1 – B.4 for the calculations, where φ_{real} is the slope error at the appropriate point, N is the number of observations and Q3 and Q1 are solved by interpolation. Outliers are defined to be either mild or extreme depending on the extent of deviation from the middle 50% of the data. Equations B.5 – B.8 are used to statistically determine the boundaries for the outlier positioning and are indicated in Figure B.2. Mild and extreme outliers are shown as circles and stars respectively. To obtain an improved slope error representation for element #7 the outliers were excluded in Equation 6.5. Results showed a slope error (φ_{RMS}) of 0.79 mrad indicating outliers accounted for 73% of the errors in comparison to results including all data points of 2.90 mrad. To increase surface accuracies in the paraboloidal element outliers need to be minimised by improving manufacturing techniques.

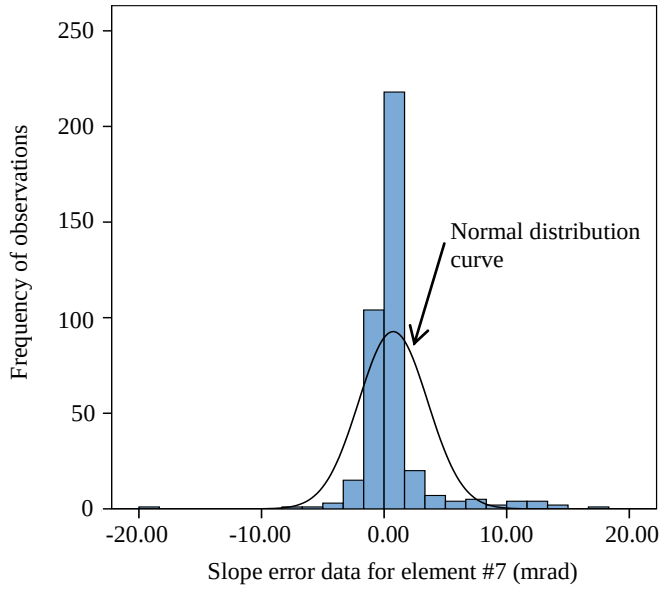

Figure B.1 Histogram plot for the 392 slope error observations for element #7. The highest frequency occurs near the ideal 0 mrad slope error with frequencies on either side decreasing. The histogram approximates a normally distributed curve with its symmetric bell-shaped appearance.

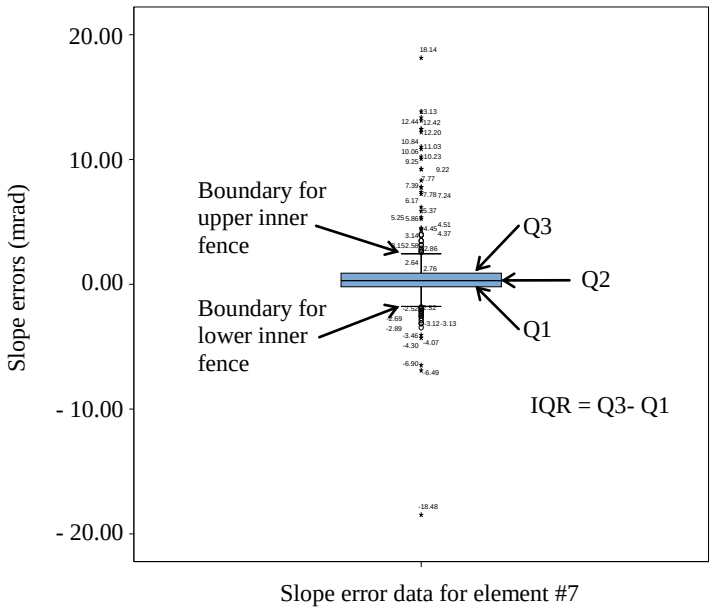

Figure B.2 Box-and-whisker plot for element #7 showing the statistical spread in the data. The blue box indicates the middle 50% of the 392 observations and is calculated from Q1, Q2 and Q3. Outliers are evident outside the upper and lower inner fence boundaries.

$$Q2 = \frac{\left(\varphi_{real_{\left(\frac{N}{2}\right)}} + \varphi_{real_{\left(\frac{N}{2}\right)+1}}\right)}{2} \quad \text{B.1}$$

$$Q3 = \varphi_{real_{\left(\frac{3}{4}(N+1)\right)}} \quad \text{B.2}$$

$$Q1 = \varphi_{real_{\left(\frac{1}{4}(N+1)\right)}} \quad \text{B.3}$$

$$IQR = Q3 - Q1 \quad \text{B.4}$$

Mild outliers

$$\begin{cases} \text{Lower inner fence} = Q1 - 1.5 * IQR & \text{B.5} \\ \text{Upper inner fence} = Q3 + 1.5 * IQR & \text{B.6} \end{cases}$$

Extreme outliers

$$\begin{cases} \text{Lower outer fence} = Q1 - 3 * IQR & \text{B.7} \\ \text{Upper outer fence} = Q3 + 3 * IQR & \text{B.8} \end{cases}$$

APPENDIX C

MATLAB SOFTWARE: CALORIMETRIC ENERGY BALANCE

MATLAB Code: Heat Transfer Analysis Code (HTAC)

```
%% Input parameters for Energy Balance Calculations

time = 42.71;                    % Water collection -flow rate calculation (s)
litres = 0.04858;                % Water collection -flow rate calc (l)
Tin = 32.23 + 273.15;            % Temperature -inlet, outlet calorimeter (K)
Tout = 33.77 + 273.15;
T0 = 37.08 + 273.15;             % Radial thermocouple measurements (K)
T5 = 36.96 + 273.15;
T10 = 37.38 + 273.15;
T15 = 37.40 + 273.15;
T20 = 37.42 + 273.15;
T25 = 37.28 + 273.15;
Tamb = 32.38 + 273.15;
hf = 206.00;                     % Theoretical ray tracing heat flux (W/cm^2)
Dt = 0.0015;                     % Diameter - tube for water flow (m)
De = 0.001;                      % Diameter - exposed copper plate surface (m)
abs = 0.95;                      % absorptivity
emi = 0.95;                      % emissivity
Cp = 4180;                       % Specific heat of water (J/kg.K)
h = 80;                          % heat transfer coefficient (W/K.m^2)
sig = 5.670*10^-8;               % Stefan Boltzmann constant (W/m^2.K^4)
k = 401;                         % Thermal conductivity copper (W/m.K)
t = 0.006;                       % Thickness of copper plate (m)
rho = 1000;                      % Density of water (kg/m^3)
mu = 0.001;                      % Viscosity of water kg/(m.s)

%% Energy Balance Methodology

Q = (litres*10^-3)/time;                    % Volumetric flow rate (m^3/s)
At = (pi*(Dt)^2)/4;                         % Area of tube for flow (m^2)
v = Q/At;                                   % Velocity of water (m/s)
mdot = rho*Q;                               % mass flow rate (kg/s)
qabs = mdot*Cp*(Tout-Tin);                  % Power absorbed by water (W)
DeltaTwater = Tout-Tin;                     % Change in water temperature (K)
T3 = (T0+T5+T10+T15+T20+T25)/6;             % Mean temp at z = 3 (K)
DeltaT = ((hf*abs/0.0001)*t)/k;             % Change in temperature between
                                              plate surface (K)
Ts = (DeltaT/2) + T3;                       % Estimated mean surface temp (K)
Ae = (pi*De^2)/4;                           % Area of exposed copper plate
                                              surface (W/m^2)
qconv = Ae*h*(Ts - Tamb);                   % Convective power losses(W)
qrad = Ae*emi*sig*((Ts^4) - (Tamb^4));      % Radiative power losses(W)
qlout = qconv + qrad;                       % Total losses(W)
qin = (qabs + qlout)/abs;                   % Total power absorbed(W)
Flux = (4*qin)/(pi*((De*100)^2));           % Flux on exposed copper plate
                                              surface (W/cm^2)
```

APPENDIX D

EXPERIMENTAL RESULTS

Sample set performance calculations for 6 mm diameter reflective shield

The experimental procedure to characterise the performance at concentrator focus includes conducting a series of tests with each reflective shield. Several experiments were conducted for each shield after which five tests which approximating the theory best were chosen to represent results. Measurement aims were to log temperature readings after three minutes of testing to allow the system to reach steady state conditions. Ambient temperature readings were recorded at the start of each test using a type K thermocouple. A sample set calculation for the 6 mm diameter shield, s_7 is shown to illustrate the methodology involved for measurement processing. Data acquisition software developed in LabVIEW (Figure D.1) was used to log temperature readings for further processing in the heat transfer analysis code (HTAC). Figure D.2 shows the LabVIEW environment representing the real-time measurement output from a typical experiment. The five experimental measurements with corresponding results chosen to represent performance results for the 6 mm diameter shield are given in Table D.1. Experimental results were normalised to 850 W/m^2 to obtain comparative test results between experiments. An average of the five tests represents a power of 39.4 W striking the exposed 6 mm diameter copper plate surface, corresponding to an estimate flux of 139.3 W/cm^2 entering the fibre optic cable. Comparison with the worst case scenario numerical analysis power result shows an 88% approximation to ray tracing simulations. Using a cable injection efficiency of 85% the power entering the 900 silica fibres is estimated at 33.5 W.

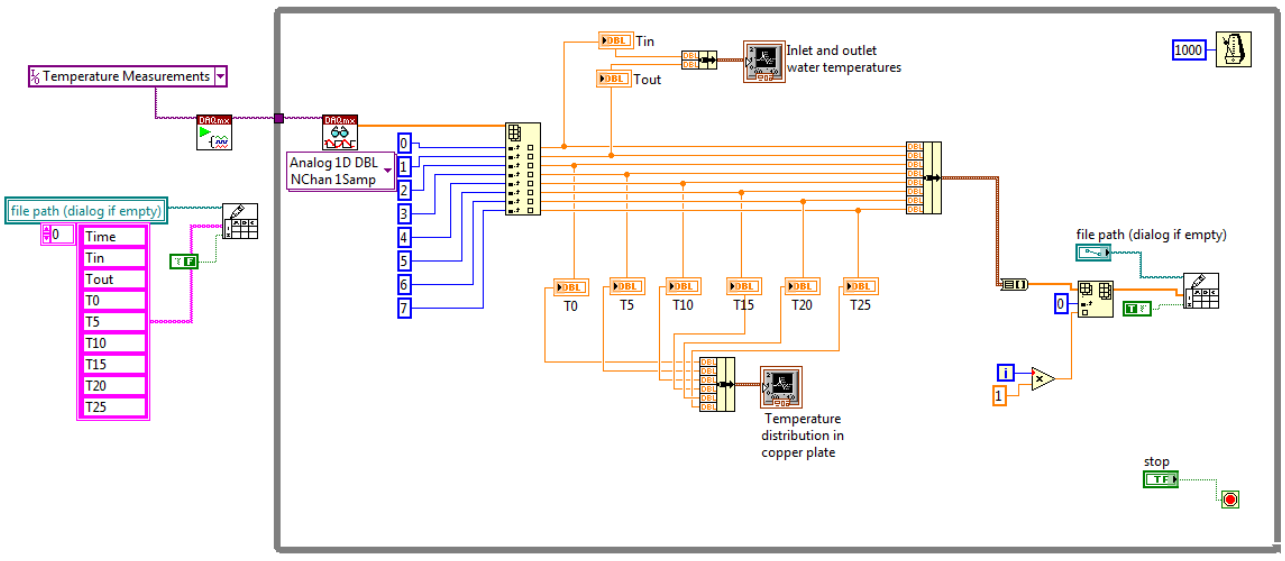

Figure D.1 LabVIEW block diagram illustrating the methodology for obtaining temperature measurements from the eight thermocouples in the calorimeter.

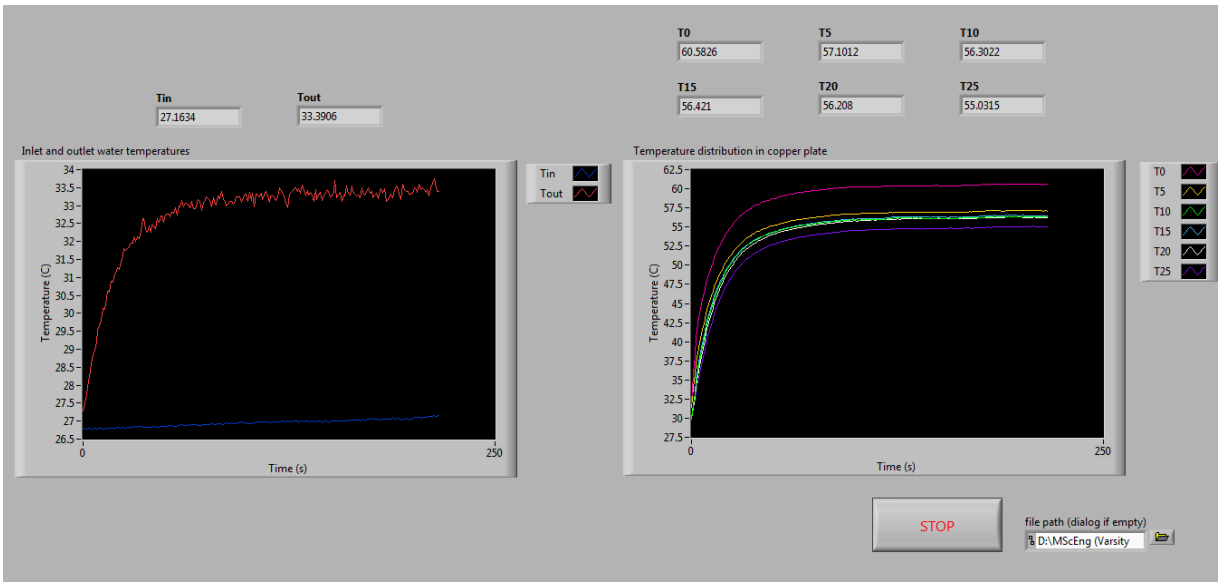

Figure D.2 LabVIEW environment showing the time evolution of temperature for all thermocouples.

Table D.1 Five experimental measurements and results for the 6 mm diameter reflective shield, s_7 using HTAC software.

	Experiment						
	#1	**#2**	**#3**	**#4**	**#5**		
Irradiance levels (W/m^2)	**954.65**	**949.27**	**937.98**	**923.39**	**890.67**		
Ray trace q_{in} (W)	50.52	50.22	48.79	48.78	46.76		
Experimental q_{in} (W)	44.29	42.19	43.22	42.10	43.63		
q_{abs} (W)	41.98	39.95	41.00	39.88	41.36		
$q_{l,out}$ (W)	0.09	0.12	0.09	0.12	0.09		
$\dot{m}$ (kg/s)	0.00181	0.00135	0.00154	0.00129	0.00186		
ΔT (T_{out} - T_{in}) (°C)	5.54	7.07	6.37	7.22	5.32		
T_s (°C)	64.55	81.43	69.19	78.26	65.12		
T_{in} (°C)	31.60	33.47	27.04	27.46	32.31		
T_{out} (°C)	37.14	40.54	33.41	34.68	37.63		
T_0 (°C)	54.27	72.15	60.53	68.89	55.37		
T_5 (°C)	52.07	68.14	57.11	66.63	53.56		
T_{10} (°C)	51.34	68.03	56.29	65.68	52.64		
T_{15} (°C)	51.15	68.95	56.43	65.70	52.68		
T_{20} (°C)	51.40	67.51	56.19	64.50	52.86		
T_{25} (°C)	51.30	68.07	54.97	64.52	52.94		
T_{amb} (°C)	30.50	31.30	32.90	30.30	29.90		
Experimental q_{in} normalised to 850 W/m^2 (W)	39.43	37.78	39.17	38.75	41.64	**39.35**	**Average**
Corresponding flux at optical waveguide inlet (kW/m^2)	1394.72	1336.12	1385.30	1370.64	1472.63	**1391.88**	**Average**

Key sample set graphs from experiment #3 are shown to illustrate a typical experiment for the 6 mm diameter reflective shield. The temperature distributions midway in the copper plate and calorimeter inlet and outlet water temperatures are shown in Figure D.3. Of importance is the stabilisation of temperature measurements which allows for the assumption of steady state conditions. A temperature difference between water inlet and outlet of 6.4°C is observed after three minutes, using a mass flow rate of 0.00154 kg/sec resulting in 41 W of power absorbed by the water. To obtain an estimate power striking the copper plate surface heat losses were calculated, using the copper plate temperature readings, and added to the power absorbed by the water. The temperature distribution midway in the copper plate is shown in Figure D.4, where the highest temperature of 60.5°C is noted at the center of the plate with a general decreasing temperature gradient towards the circumference. The temperature measurements of T_{10}, T_{15} and T_{20} show unexpected similar readings with possible reasons due to thermocouple inaccuracies or imprecise machining of the copper plate. Using the midway temperature measurements of the copper plate and HTAC an estimate surface temperature of 69.2°C was obtained, which is not close to the ambient temperature of 32.9°C. One of the objectives of the calorimetric experiments was to keep the copper surface close to the ambient temperature to reduce heat losses. Nonetheless heat losses due to convection and radiation amounted to 0.2% of the power absorbed, resulting in an estimate power striking the copper plate surface of 43.2 W at an irradiance of 938.0 W/m^2. This corresponds to an efficiency of 24% which is in good agreement with the Case 8 numerical efficiency result at optical waveguide inlet of 27%.

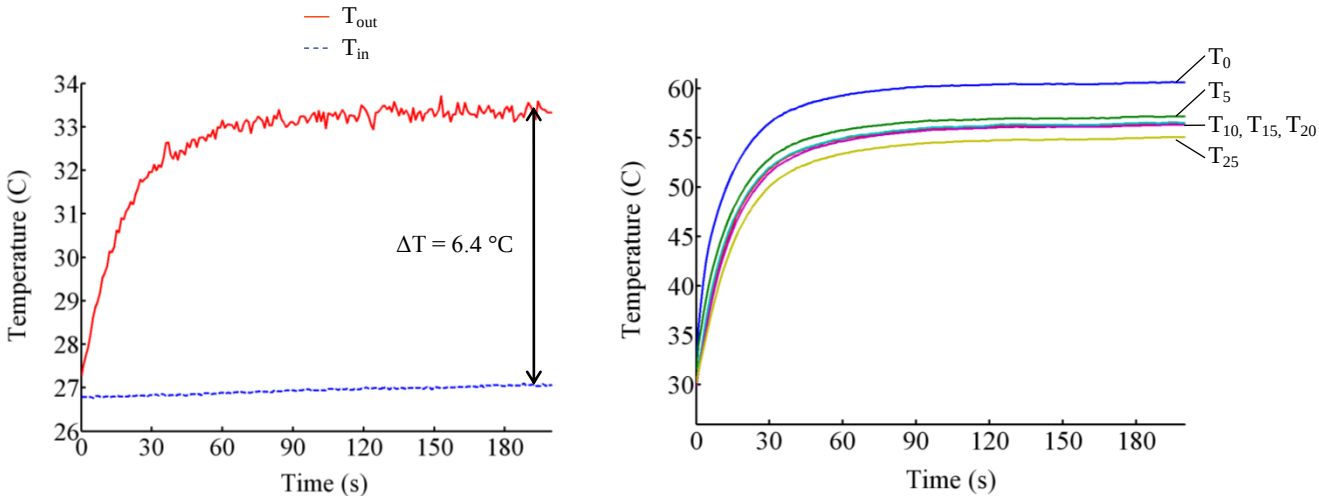

Figure D.3 Results from experiment #3, showing a water temperature difference of 6.4°C (left) and temperature measurements midway in the copper plate (right). The experimental procedure was conducted for three minutes allowing the temperatures to reach steady state conditions.

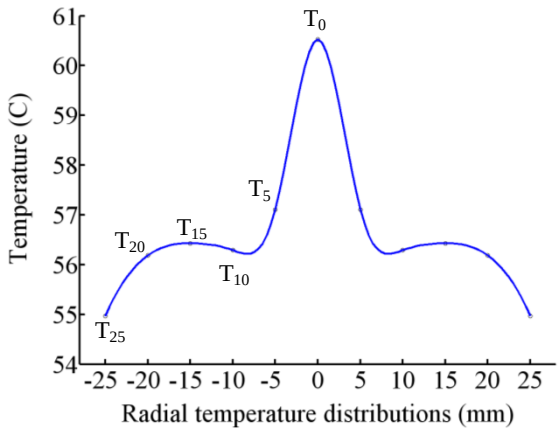

Figure D.4 Temperature distribution midway in copper plate (z = 3 mm) after three minutes of testing. Assuming a concentric focal spot on the calorimeter surface allows obtaining a mirrored representation of temperatures on the full diameter copper plate.